

INCORPORATING HYDROGEN AND TUNGSTEN IN STRUCTURALLY ORIENTED VO₂ THIN FILMS, AND THE RESULTANT EFFECTS ON PHYSICAL PROPERTIES

Ph.D. Thesis

By
KOMAL MULCHANDANI



**DISCIPLINE OF PHYSICS
INDIAN INSTITUTE OF TECHNOLOGY INDORE
JANUARY 2021**

INCORPORATING HYDROGEN AND TUNGSTEN IN STRUCTURALLY ORIENTED VO₂ THIN FILMS, AND THE RESULTANT EFFECTS ON PHYSICAL PROPERTIES

A THESIS

*Submitted in partial fulfillment of the
requirements for the award of the degree*

of

DOCTOR OF PHILOSOPHY

by

KOMAL MULCHANDANI



DISCIPLINE OF PHYSICS

INDIAN INSTITUTE OF TECHNOLOGY INDORE

JANUARY 2021



INDIAN INSTITUTE OF TECHNOLOGY INDORE

CANDIDATE'S DECLARATION

I hereby certify that the work which is being presented in the thesis entitled **INCORPORATING HYDROGEN AND TUNGSTEN IN STRUCTURALLY ORIENTED VO₂ THIN FILMS, AND THE RESULTANT EFFECTS ON PHYSICAL PROPERTIES** in the partial fulfillment of the requirements for the award of the degree of **DOCTOR OF PHILOSOPHY** and submitted in the **DEPARTMENT/SCHOOL OF PHYSICS, Indian Institute of Technology Indore**, is an authentic record of my own work carried out during the time period from July, 2017 to January, 2021 under the supervision of Dr. Krushna R. Mavani, Professor, Department of Physics.

The matter presented in this thesis has not been submitted by me for the award of any other degree of this or any other institute.

Komal
08.12.21

**signature of the student with date
(KOMAL MULCHANDANI)**

This is to certify that the above statement made by the candidate is correct to the best of my knowledge.

Krushna R. Mavani

03.01.2022

Signature of Thesis Supervisor with date
(PROF. KRUSHNA R. MAVANI)

KOMAL MULCHANDANI has successfully given his/her Ph.D. Oral Examination held on **November 24, 2021**.

Krushna R. Mavani

03.01.2022

Signature of Thesis Supervisor with date
(PROF. KRUSHNA R. MAVANI)

ACKNOWLEDGEMENTS

“Waheguru ji ka Khalsa, Waheguru ji ki Fateh”

First and foremost, I am deeply grateful and express my deep sense of gratitude and profound respect to my PhD supervisor Prof. Krushna R Mavani for giving me the opportunity to work with her. Her constant encouragement and guidance helped me to do my research fruitfully. She is the kindest, soft-hearted, peaceful, and emotional person I know. My PhD journey was very unpredictable and challenging, but she stood by my side throughout my tough time. I will be lifetime indebted towards her for such immense support.

I would like to extend my sincere gratitude towards my PSPC members Dr. Preeti A. Bhobe, Department of Physics and Dr. Ajay K. Kushwaha, Department of MEMS, IIT Indore for their valuable suggestions and encouragement to improve my research work.

I gratefully acknowledge DPGC Physics, HOD Physics, DOAA and Director, IIT Indore for providing support. Particularly, I would like to thank Sen sir for giving me advice like father and kept me motivated in the journey.

I acknowledge Sophisticated Instrumentation Centre (SIC) IIT Indore, specially Mr. Nitin Upadhyay and Mr. Kinny Pandey for their support during the measurements. I also acknowledge RRCAT, Indore for XPS measurements.

I acknowledge Department of Science and Technology (DST), India for providing the INSPIRE fellowship.

I sincerely thank my senior fellows Dr. Harisankar S, Dr. Kavita Soni and Dr. Ankit Soni for guidance and fruitful discussions. I thank my lab mates Ms. Ekta Yadav, Ms. Reena Yadav, Ms. Komal Pathy, Mr. Shubham Kothari and Mr. Saurav Tomar for providing friendly atmosphere in Lab. I would like to individually mention Dr. Ankit Soni who trained

me and helped me to start my work. I also thank Ekta for Raman measurements and Komal for proofreading of articles and thesis.

I would like to thank my friends at IIT Indore, Siddhartha, Sheetal, Shweta di, Rinki di, Sushmita, Nagaraju, Prashant for their support and love.

The best part of this journey is to meet my best buddy Siddhartha. I would like to thank him for his constant support, care, encouragement and for reducing my stress and making me happy. Also, I would like to express my sincere gratitude to his family for their support and love.

I also thank to my friends Dr. Varun, Dr. Shruti, Mansi, Pooja, and Neha. I also would like to acknowledge my colleagues at my workplace for sharing the workload which helped me to complete my thesis writing on time.

I express my sincere gratitude towards my family members, Grandmother, Mother, Father, Brother, Sister-in-law, niece for their endless support and extreme love. My niece, Anshi who always made me smile irrespective of the situation.

Last but not the least, a very special thanks to my lovely “mom” for her unconditional love and care, without her support this would have not been possible. I dedicate this thesis to her. Words are not enough to convey my gratitude towards her. Her compromises and commitment made me what I am today as an individual. It was too difficult to complete my PhD journey without her as she was the backbone of my life. Although, your physical presence is not with me, but I can feel you in every single moment of my life since our souls are still connected. I love you, Mummy!!

KOMAL MULCHANDANI

**I Dedicate this thesis to
My Mother
“Poonam Mulchandani”**

LIST OF PUBLICATIONS

A. Relevant to the Thesis (Peer-reviewed Journals):

1. **Komal Mulchandani**, Ankit Soni, K. R. Mavani “Structure influenced rapid hydrogenation using metal-acid contacts on crystallographically oriented VO₂ thin films”, *Applied surface science*”, **451** (2021) 148369.
(doi.org/10.1016/j.apsusc.2020.148369).
2. **Komal Mulchandani**, Ankit Soni, Komal Pathy, K. R. Mavani “Rapid hydrogenation of VO₂ thin films via metal-acid contact method using mild electric fields at room temperature”, *Materials Letters*, **295** (2021) 129786.
(doi.org/10.1016/j.matlet.2021.129786). *Impact factor 3.423*
3. **Komal Mulchandani**, Ankit Soni, Komal Pathy, K. R. Mavani “Structural transformation and tuning of electronic transitions by W-doping in VO₂ thin films”, *Superlattices and Microstructures*, **154** (2021) 106883.
(doi.org/10.1016/j.spmi.2021.106883). *Impact factor 2.658*

B. Other than Thesis (Peer-reviewed Journals):

1. Ankit Soni, **Komal Mulchandani**, K. R. Mavani “UV activated visible-blind Ga:ZnO photodetectors using the GLAD technique: A comparative study under different gas atmospheres and temperatures”, *J. Mater. Chem. C*, **8** (2020) 7837.
(doi.org/10.1039/D0TC00990C).
2. Ankit Soni, **Komal Mulchandani**, K. R. Mavani “Effects of substrates on the crystalline growth and UV photosensitivity of glancing angle deposited porous ZnO nanostructures” *Sensors and Actuators A: Physical*, **313** (2020) 112140.
(doi.org/10.1016/j.sna.2020.112140).
3. Ankit Soni, **Komal Mulchandani**, K. R. Mavani “Crystallographically oriented porous ZnO nanostructures with

visible-blind photoresponse: Controlling the growth and optical properties” *Materialia*, **6** (2019) 100326.

(doi.org/10.1016/j.mtla.2019.100326).

C. Conference Proceedings/ Poster (Oral) presentation:

1. **Komal Mulchandani**, Ankit Soni, K. R. Mavani “Effects of deposition temperature on growth and properties of pulsed laser deposited VO₂ thin films and nanostructures” *AIP Conference Proceedings*, **2100** (2019) 020051.
(doi.org/10.1063/1.5098605). [poster presentation and proceedings]
2. Ankit Soni, **Komal Mulchandani**, K. R. Mavani “Ultraviolet photoresponse of crystallographically oriented nanostructured thin films of ZnO grown by pulsed laser deposition” *AIP Conference Proceedings*, **2100** (2019) 020077.
(doi.org/10.1063/1.5098631).

D. Conferences/ school attended:

1. ORAL presentation in “Emerging Interfaces of Physical Sciences and Technology (EIPT)” conference, 29th -30th August 2019, Vikram university Ujjain, India.
2. Prof. Dinesh Varshney memorial “National Conference on Physics and Chemistry of Materials (NCPCM)”, 27th - 28th December 2018, DAVV Indore, India.
3. “Winter School on Synchrotron Techniques on Materials”- 25th- 31st October 2018, S. N. Bose National Centre for Basic Sciences Kolkata, India.

TABLE OF CONTENTS

Acknowledgements	i
List of Publications	vi
List of Figures	xi
List of Tables	xiv
Acronyms	xv

Title	Page No.
Chapter 1: Introduction	
1.1 An overview of transition metal oxides	2
1.2 VO ₂ : The material of interest	3
1.3 Properties of VO ₂	5
1.3.1 Crystal structure	5
1.3.2 Vibrational properties	5
1.3.3 Electronic properties	7
1.3.3.1 The Mott versus Peierls controversy	8
1.4 Applications of VO ₂ and motivation	9
1.4.1 Hydrogenation in VO ₂ thin films	11
1.4.1.1 Metal-acid contact method of hydrogenation	11
1.4.2 W doping in VO ₂ thin films	12
1.5 Objectives	13
1.6 Organization of the Thesis	13
References	15

Chapter 2: Experimental and Characterization Techniques

2.1 Synthesis methods	26
2.1.1 Synthesis of bulk material	26
2.1.2 Synthesis of thin films	27
2.1.2.1 Experimental setup of PLD	28
2.1.2.2 Thin film growth mechanism in PLD	29
2.2 Hydrogenation procedure	30
2.3 Characterization Techniques	32
2.3.1 X-ray Diffraction (XRD)	32
2.3.2 X-ray Reflectivity (XRR)	34
2.3.3 Raman spectroscopy	36
2.3.4 Atomic Force Microscopy (AFM)	39
2.3.5 X-ray Photoelectron Spectroscopy (XPS)	41
2.3.6 DC resistivity measurements	42
References	45

Chapter 3: Structure influenced rapid hydrogenation in VO₂ thin films

3.1 Introduction	49
3.2 Experimental	50
3.2.1 Bulk target and VO ₂ thin films synthesis	50
3.2.2 Hydrogenation Procedure	51
3.3 Results and Discussion	52
3.3.1 Structural analysis	52
3.3.2 Surface Analysis	56
3.3.3 Chemical composition	57
3.3.4 Electronic properties	58
3.4 Summary	60
References	61

Chapter 4: Electric field induced rapid hydrogenation in VO₂ thin films

4.1 Introduction	65
4.2 Experimental	66
4.2.1 Bulk target and VO ₂ thin films synthesis	66
4.2.2 Hydrogenation procedure	66
4.3 Results and Discussion	68
4.3.1 Structural Analysis	68
4.3.2 Surface analysis	69
4.3.3 Local structure	70
4.4.4 Electronic properties	75
4.4 Summary	77
References	79

Chapter 5: Tuning of structural and electronic transitions by tungsten doping in VO₂ thin films

5.1 Introduction	82
5.2 Experimental	82
5.3 Results and discussion	83
5.3.1 Structure and morphology	83
5.3.2 Local structure analysis	86
5.3.3 Chemical composition	91
5.3.4 Metal to insulator transition characteristics	93
5.4 Summary	96
References	97

Chapter 6: Conclusions and Future Prospects

6.1 Conclusions	102
6.2 Future Prospects	103

LIST OF FIGURES

Figure	Page No.
Figure 1.1: Crystal structure of VO ₂ ; monoclinic(M1) (<i>left</i>) and rutile(R) (<i>right</i>) structure.	5
Figure 1.2: Band diagram of VO ₂ in rutile(R) and monoclinic(M1) phase.	8
Figure 1.3: Vanadium ion position in M1, M2, T and R phases of VO ₂ .	9
Figure 1.4: Applications of VO ₂ based on the ultrafast MIT.	10
Figure 1.5: Schematic representation of the metal-acid contact method.	12
Figure 2.1: Different stages of solid-state reaction route.	27
Figure 2.2: Schematic of the experimental setup of PLD.	27
Figure 2.3: PLD setup with plume formation during deposition of VO ₂ thin film.	28
Figure 2.4: Schematic diagram for nucleation and growth modes of thin films.	30
Figure 2.5: Hydrogenation <i>via</i> metal-acid contact method at a particular temperature.	31
Figure 2.6: Hydrogenation <i>via</i> metal-acid contact method under a mild electric field.	32
Figure 2.7: Diffraction of X-ray by crystals.	33
Figure 2.8: Schematic of the X-ray diffraction (XRD).	34
Figure 2.9: Schematic representation of XRR geometry.	35
Figure 2.10: Schematic representation of the Rayleigh, Stokes and anti-Stokes Raman lines.	36
Figure 2.11: Energy relation for Rayleigh scattering, Stokes and anti-Stokes scattering.	37
Figure 2.12: Schematic representation of the Raman instrument.	38
Figure 2.13: Schematic representation of an AFM setup.	40
Figure 2.14: Resistivity measurement by the two-point probe.	43
Figure 2.15: Resistivity measurement by the four-point probe.	44
Figure 2.16: Experimental setup for the temperature-dependent resistivity measurement.	44

Figure 3.1: Schematic diagram of the hydrogenation process.	51
Figure 3.2: (a) Full-scale XRD of pristine VO ₂ film and sapphire substrate. XRD peaks other than (00l) reflections from a substrate are marked by *. (b) XRD patterns of pristine and hydrogenated VO ₂ thin films grown on the Al ₂ O ₃ substrate.	53
Figure 3.3: (a-c) Temperature-dependent Raman spectra of VO ₂ , VO ₂ -300 and VO ₂ -343 films.	55
Figure 3.4: XRR fitting and AFM images of pristine and hydrogenated VO ₂ thin films.	56
Figure 3.5: V2p and O1s core level XPS spectra of VO ₂ and VO ₂ -343 films, confirming the V ³⁺ state after hydrogenation.	58
Figure 3.6: Temperature-dependent resistivity curves of VO ₂ films, inset shows temperature versus resistivity curve of VO ₂ -343 after dehydrogenation process.	59
Figure 4.1: Schematic diagram of the hydrogenation process.	67
Figure 4.2: Full-scale XRD patterns of VO ₂ thin films and sapphire substrate. XRD peaks other than (00l) reflections from a substrate are marked by *.	68
Figure 4.3: Magnified view of (020) diffraction peak of pristine and hydrogenated VO ₂ thin films grown on the Al ₂ O ₃ substrate; inset shows the XRR spectrum.	69
Figure 4.4: AFM images of VO ₂ , 0-VO ₂ , 0.1-VO ₂ films.	70
Figure 4.5: Room temperature Raman spectra of pristine and hydrogenated VO ₂ thin films on Al ₂ O ₃ substrate. Inset shows the magnified view of the most intense phonon mode (at 194 cm ⁻¹).	71
Figure 4.6: Temperature-dependent Raman spectra of VO ₂ and 0.5-VO ₂ films.	72
Figure 4.7: Linearly fitted temperature dependent Raman-shift of the most intense mode (~at 194 cm ⁻¹).	73
Figure 4.8: Variation in low-frequency mode intensities with temperature for VO ₂ and 0.5-VO ₂ films.	74
Figure 4.9: Arrhenius fitting of VO ₂ and hydrogenated VO ₂ thin films in temperature region (313K-300K).	76

Figure 4.10: Temperature-dependent resistivity curves of pristine and hydrogenated VO₂ films, inset shows temperature versus resistivity curve of VO₂, DH-0.001-VO₂ and DH-0.1-VO₂ films. 77

Figure 5.1: Full-Scale XRD patterns of undoped and W-doped VO₂ thin films and sapphire substrate. XRD peaks other than (00l) reflections from substrate are marked by '*'. 84

Figure 5.2: XRD patterns showing (020) reflection of V_{1-x}W_xO₂ (x=0, 0.01, 0.02, 0.03, 0.04) thin films on sapphire substrate. 85

Figure 5.3: Variations in Bragg's Angle, FWHM and crystallite size of (020) peak of VO₂ thin films with different doping content. 85

Figure 5.4: AFM images of (a)VO₂, (b)V_{99.99}W_{0.01}O₂, and (c)V_{99.97}W_{0.03}O₂ thin films grown on the sapphire substrate. 86

Figure 5.5: Room temperature Raman spectra of V_{1-x}W_xO₂ (x=0, 0.005, 0.01, 0.015, 0.02) thin films. 87

Figure 5.6: (a) Variation in intensity of high and low frequency mode with different doping content. (b) Raman shift and FWHM of mode 194cm⁻¹ with different doping percentage. 88

Figure 5.7: Top-panel shows the transformation of structure and bottom-panel shows the band structure variation with W doping. In the top panel, solid lines show the monoclinic structure and dashed lines show the inclination of the structure towards rutile phase. 89

Figure 5.8: Temperature-dependent Raman spectra of (a) VO₂ and (b) V_{99.98}W_{0.02}O₂ thin films. 90

Figure 5.9: XPS survey spectrum of comparison of pure VO₂ and V_{99.96}W_{0.04}O₂ films. 91

Figure 5.10: High-resolution XPS spectra for V2p and O1s of VO₂ and V_{99.96}W_{0.04}O₂ films. 92

Figure 5.11: Temperature-dependent resistivity measurement of V_{1-x}W_xO₂ (x=0, 0.01, 0.015, 0.04) thin films, top inset shows the corresponding derivative plots and bottom inset shows resistivity curve of V_{1-x}W_xO₂ (x=0.04) thin film in low temperature range. 94

Figure 5.12: Arrhenius fitting of V_{1-x}W_xO₂ (x=0, 0.01, 0.015) thin films in temperature region (230K-280K). 95

LIST OF TABLES

Table	Page no.
Table 4.1: Peak position of the most intense Raman mode, room temperature resistivity, activation energy of pristine and hydrogenated VO ₂ thin films.	76
Table 5.1 Electronic transport properties for undoped and W-doped VO ₂ thin films.	95

ACRONYMS

Vanadium dioxide	VO ₂
Metal of Insulator Transition	MIT
Pulsed Laser Deposition	PLD
X-ray Diffraction	XRD
X-ray Reflectivity	XRR
Atomic Force Microscopy	AFM
X-ray Photoelectron Spectroscopy	XPS
Full Width at Half Maximum	FWHM

Chapter 1

Introduction

This chapter presents a brief review of the transition metal oxides and their applications in devices. The material of interest, *i.e.*, vanadium dioxide (VO_2), has been explored in detail with its fundamental properties and applications. Metal-acid contact method used to hydrogenate the films and the necessity to improve this method has been discussed in detail. A comparison with other hydrogenation methods has also been presented. The motivation and the objectives are defined towards the end of the chapter.

1.1 An overview of transition metal oxides

The role of metal oxides came into the picture for countering the unprecedented growth of electronics and other applications. It was predicted that once the dimension reaches quantum size, the effect of scaling will get apprehended [1,2]. Thus, to sustain the emerging requirements of technologies, there is a boom for utilizing oxide materials at the nanoscale. Numerous oxides possess a potential for adapting the requirement of current electronics. Some new physical properties like spintronics, single electron electronics and superconducting electronics are the best approaches towards the trending area [3]. Metal oxide semiconductors belong to a discrete class of materials because of its charge transport nature when compared with conventional semiconductors like silicon (Si). As the conduction band minimum and valance band maximum generally have metal and oxygen respectively, the interaction causes a significant discrepancy of charge carrier transport [4]. Electron and hole transport are the phenomena followed by the metal oxide semiconductors, and it can be understood that a better n-type or p-type conductivity cannot be gained intrinsically. Therefore, in the case of metal oxides, the defect serves as donors and acceptors. In most of the cases the band gap is wide, the defect levels are considerably too deep to provide high concentrations of carriers. Thus, external doping with controllable parameters needs to be realized [5].

There are several challenges in the field of electronics and a single material cannot withstand in every possible application. Thus, we have to consider different alternatives and design of devices in every manner. For example, in transparent and flexible electronics, oxides are performing very well as compared to the organic compound and low dimensional carbon materials [6,7]. Likewise, perovskite oxides are considered for the magneto-optical devices for better responses.

Very extensive research activities are concentrated on the synthesis and device fabrication using functional oxides [8–10]. By doping, strain, oxygen deficiencies and other external factors, the

properties such as electrical, optical, magnetic, and chemical stoichiometry can be tuned. This tuning of functional properties is necessary for fabricating smart devices, which also makes these oxides the most diverse class of materials. Oxides have also been the subject of interest for basic and applied research, covering almost all aspects of materials science and physics in areas such as superconductivity, ferroelectricity, magnetism, magneto-electronics and electronics *etc.* [11–15]. In recent technological applications, oxides provide a promising alternative option for application in the fabrication of microelectronic circuits, gas sensors, piezoelectric devices, fuel cells, dye-sensitized solar cells, coatings for the passivation of surfaces against corrosion *etc.* [16–20]. Some of the commonly used functional oxide materials are TiO_2 , ZnO , VO_2 , HfO_2 , WO_3 *etc.* Among these materials, vanadium dioxide (VO_2) has appeared as a promising material for several applications due to its enriched and controllable electronic properties.

1.2 VO_2 : The material of interest

Strongly correlated materials are a group of materials in which the electron-electron interactions cannot be ignored. Vanadium dioxide (VO_2) is a prototype strongly correlated oxide which has attracted attention due to its ultrafast ($\sim 100\text{fs}$), first-order metal-insulator transition (MIT) slightly above room temperature ($\sim 68^\circ\text{C}$) [21] which is easily alterable by doping [22–26], oxygen vacancies [27,28], strain [29] *etc.* Although other oxides of vanadium, such as VO , V_2O_3 and V_2O_5 also exhibit insulator to metal transition, VO_2 stands out to be interesting as its transition temperature is near room-temperature and can be lowered by using the appropriate chemical modifications. This phenomenon is also sometimes termed as a metal-semiconductor transition because of the small bandgap ($\sim 0.6\text{eV}$) in VO_2 [30].

One of the most intriguing features of VO_2 is that it exists in at least 14 different kinds of polymorphs. These polymorphs have been classified based on its crystal structure and space group. For example,

both VO₂(M1) and VO₂(M2) hold a monoclinic structure with different space groups *i.e.*, $P21/c$ and $C2/m$ respectively, VO₂(T) adopts the triclinic structure with $\bar{P}1$ space group. VO₂(R) attains the tetragonal crystal structure with $P42/mnm$ space group [31]. The M2 and T phases are unstable and can be stabilised with stress engineering and doping content. The most common and easily achievable, stable phase is VO₂(M1). The focus of the present study is on M1 (at low temperature) and R (at high temperature) phase. As the functional aspects of VO₂ thin films can be tailored, the attention was paid on the study of thin films for applications. Morin, in 1959 presented a study on bulk VO₂ crystals and revealed that they exhibit a reversible semiconductor-metal transition at 68°C [21]. In bulk crystals, the change in resistivity is of the order $\sim 10^3 - 10^4$ ohm-cm, with a hysteresis width of $\sim 1^\circ\text{C}$. However, in thin films, hysteresis widths are nearly in the range of 10 -15°C with a change in resistivity $\sim 10^4 - 10^5$ ohm-cm [32]. The transition can be simply triggered by heating the VO₂ over the transition temperature. Joule heating due to the current flow through thin films will also cause the temperature increase and hence trigger the transition. The deposition of phase pure thin films of monoclinic VO₂ poses a stiff challenge because of the presence of numerous stable oxidation states of vanadium oxides and a variety of structural polymorphs of VO₂.

A suitable growth technique to produce high quality oxide thin films is Pulsed laser deposition (PLD) method [33,34], as it enables precise control over various parameters such as temperature and oxygen partial pressure, thus allowing for the control of the film's stoichiometry, phase and thickness. It is also possible to adjust the defect concentration in the films by adjusting the deposition conditions, such as the substrate temperature and the laser energy fluence.

1.3 Properties of VO₂

1.3.1 Crystal structure

At high temperatures, the VO₂ exists in a more stable, symmetric tetragonal/rutile ($P42/mnm$) stable rutile phase with lattice parameters $a_R=b_R=4.55 \text{ \AA}$ and $c_R=2.85 \text{ \AA}$. The structure of the rutile phase can be described as the V atom is forming a body centred tetragonal lattice, and each V atom being surrounded by an octahedron of oxygen atoms, as depicted in the figure 1.1. As we start to move towards the lower temperatures, dimerization and tilting of the V-V pairs starts to take place and the lattice transforms into a less symmetric monoclinic ($P21/c$) structure. A typical feature of the monoclinic phase is the presence of the V-V pairs along the $a_m = 2c_r$ axis. This leads to the doubling of the unit cell and a change in the alternate V-V separations which now become 2.65 \AA and 3.12 \AA instead of the regular 2.85 \AA [35]. Schematic diagrams of the two structures are as shown in figure 1.1.

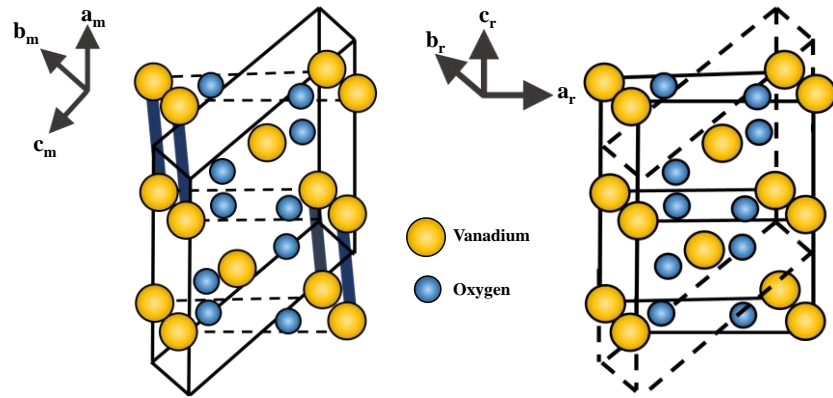


Figure 1.1: Crystal structure of VO₂; monoclinic(M1) (*left*) and rutile(R) (*right*) structure.

1.3.2 Vibrational properties

A study of the lattice vibrations helps in getting a clearer picture of the structural changes during the MIT. Raman spectroscopy has been extensively used for this because of its outstanding sensitivity towards lattice vibrations. Group theory predicts a total of 18 *i.e.*, $9A_g+9B_g$ modes in the monoclinic phase that are Raman active. The B_g modes are

usually the ones with weaker Raman intensities. Experimentally, distinct A_g phonon features are observed at 137, 194, 224, 310, 340, 393, 499, 612, and 663 cm^{-1} , whereas B_g phonons are observed at 143, 224, 262, 393, 442, 450, 484, 582, and 820 cm^{-1} . The A_g and B_g modes that coexist near 224 cm^{-1} and 393 cm^{-1} have not been resolved experimentally. The modes at 194 cm^{-1} and 224 cm^{-1} correspond to the V-V vibrations whereas the higher modes are due to the vibrations of V-O bonds [31,36]. The mode at 612 cm^{-1} can be related to the stretching of V-O bonds, whilst the phonons in the intermediate energy range are attributed to different bending modes of V-O vibration.

The modes predicted for the rutile phase are of A_{1g} (145 cm^{-1}), B_{1g} (448 cm^{-1}), B_{2g} (613 cm^{-1}), and E_g (826 cm^{-1}) symmetries, all of which are associated with the V-O vibrations. A_{1g} and B_{2g} modes are due to the motion of the oxygen atoms in the ab -plane and parallel to the c -axis, whereas the E_g mode is associated with the vibration of the oxygen atoms along the c -axis. In B_{1g} modes, the vibrations of the oxygen atoms are perpendicular to the ab plane. However, broad featureless spectra are obtained in the high temperature rutile phase [31,37]. The above information on the phonon modes of VO_2 can be extremely useful in probing the structural changes in the films due to external factors such as strain, doping, temperature and electric field.

Raman features are also useful in monitoring the phase anomalies, if any, as the VO_2 transitions from $\text{VO}_2(\text{M1})$ to $\text{VO}_2(\text{R})$ phase. $\text{VO}_2(\text{M1})$, $\text{VO}_2(\text{M2})$, and $\text{VO}_2(\text{T})$, display similar Raman features. There are 18 allowed Raman-active modes for each of these phases ($9A_g + 9B_g$ for $\text{VO}_2(\text{M1})$, $10A_g + 8B_g$ for $\text{VO}_2(\text{M2})$, and $18A_g$ modes for $\text{VO}_2(\text{T})$ phase) [31]. A shift in the peaks at 613 cm^{-1} , 189 cm^{-1} or 444 cm^{-1} , or a splitting of the peak at 225 cm^{-1} gives the confirmation of M1 or M2 phases.

With the increase in temperature, the expected softening of phonon modes due to thermal expansion is observed. The relationship

between the thermal expansion and the temperature can be best represented by the following equation:

$$\omega(T) = \omega_0 + \chi T \quad (1.1)$$

Where ω_0 is the phonon frequency at 0K, $\omega(T)$ is the frequency at temperature T and χ is the temperature coefficient of thermal expansion [38]. The intensities of the modes are an indication of the amount of the insulating phase. The intensities of the modes start to decrease as we move towards the metallic phase (symmetric structure) [37].

1.3.3 Electronic properties

The electronic properties of different phases of VO₂ were first explained qualitatively with the help of energy band diagrams, proposed by Goodenough [39]. This model suggests that, octahedral crystal field splits the *d*-levels of the V ions into lower-lying triplet *t*_{2g} and doublet *e*_g states. The octahedral crystal field due to the six O atoms, splits the *t*_{2g} multiplet into a *d*_{||} state and π^* doublet. The *d*_{||} states correspond to the V-V bonds along the rutile *c*-axis. In the rutile phase, the *t*_{2g} states overlap and a single electron is present in the lowest *d*_{||} state thus making the films metallic. However, in the less symmetric monoclinic phase, the octahedral field is disturbed due to the formation of V-V pairs. As a result, *d*_{||} states are split into two bonding states with lower energy and an antibonding state with higher energy. A bandgap of ~1.8eV is opened up. Further, tilting of the V-V pairs leads to a greater overlap between the O states and thus π^* band also moves away from the Fermi level, thus opening a bandgap of ~0.7eV between the *d*_{||} and π^* doublet states, which can be considered as a Peierls-like band gap [30,40]. Electronic band structures of the rutile and monoclinic phases are as shown in figure 1.2.

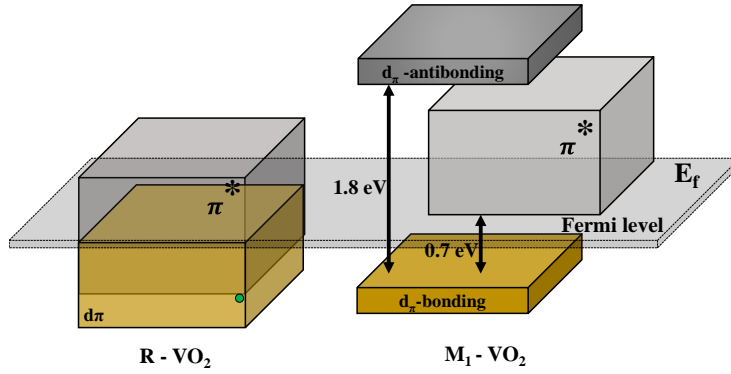


Figure 1.2: Band diagram of VO₂ in rutile(R) and monoclinic(M1) phase.

1.3.3.1 The Mott versus Peierls controversy

Whether the MIT in VO₂ is Mott-Hubbard transition or a Peierls transition has been a long-standing debate [41–43]. In the Peierls theory, a structural transformation leads to change in the fermi level and creates an energy gap. The splitting of $d_{||}$ band due to dimerization of the V-V pairs can be considered as a Peierls transition. However, the density functional theory simulations based on this theory do not match the experimentally found bandgap which is $\sim 0.6\text{eV}$ [44]. On the contrary, strong evidence in favour of a Mott-Hubbard transition was presented by *Pouget et al.*, who showed that a new phase M2 is obtained by a small doping of Cr and application of uniaxial strain. In this phase, only half of the V-atoms dimerize, while the other half form chains of evenly spaced atoms acting as spin-1/2 Heisenberg chains [45]. The obtained phase was also insulating which indicated that the transition probably is a Mott-Hubbard one.

Further, *Rice et al.* emphasized that the transition between the R→M1 phase takes place *via* two intermediate phases *viz* R→M2→T→M1 where M1, M2, and T are all Mott insulators [46]. As depicted in the figure 1.3, the M2 phase comprises two types of chains, one is indicated by the dashed lines which shows only tilting of the vanadium ions and another one is indicated in the solid lines which represents pairing of the vanadium ions. In the M1 phase, all the

vanadium ions show both pairing and tilting. T phase is the intermediary phase of M1 and M2 phases [47]. The Mott-Hubbard model is however incompatible with the structural transitions.

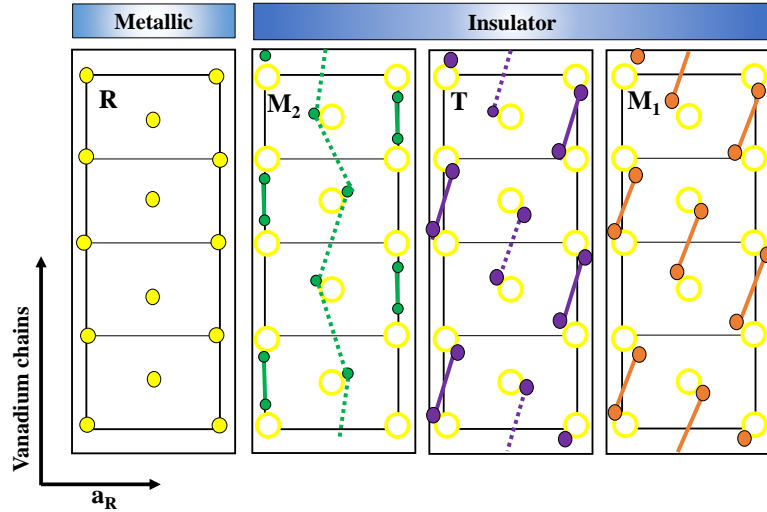


Figure 1.3: Vanadium ion position in M1, M2, T and R phases of VO₂.

Till date, many studies have been presented to unravel the mechanism, but the problem remains vastly unsolved. It is now accepted that neither a strong electron correlation nor a distortion of the lattice is sufficient to open the insulating gap [44]. Understanding the underlying mechanism is crucial for regulating the correlation effects in VO₂ and will pave the way for understanding other transition metal oxides.

1.4 Applications of VO₂ and motivation

VO₂ has drawn a lot of attention because of its potential applications in ultrafast optical and electrical switching [48–50], memory devices [51–53], smart windows [54,55], sensors and actuators [56–58], field-effect devices [59,60] etc. A unipolar field-effect transition with broad on/off amplitude has been demonstrated by electric double layer transistors (EDLTs) having VO₂ as a channel material [61]. The plethora of applications has just started to be explored [62]. It is important here to note that the main pertinence of VO₂ thin films is mainly in MIT-based applications.

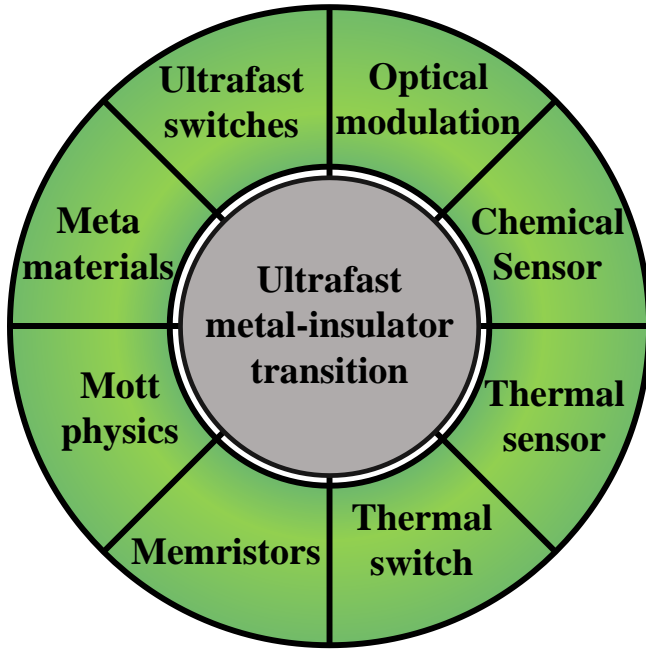


Figure 1.4: Applications of VO₂ based on the ultrafast MIT (reproduced from the reference [6]).

In order to control the properties of the strongly correlated materials, it is essential to understand the metal to insulator transition. The transition temperature of thin films can be tuned by varying parameters such as strain, doping, oxygen content, thickness variation *etc.* according to the requirement of the practical applications. One of the most administrable methods to tune electronic properties is by injecting charge carriers *via* chemical modifications such as interstitial and substitutional doping. Doping of an element can be an easy and feasible option for the fine-tuning of the transition temperature.

Doping with heavy ions such as W⁶⁺ and Mo⁶⁺, is generally used as the standard way of regulating the carrier concentration. However, the injection of such a large ion into the lattice causes structural deformation along with the carrier injection. The two entangled phenomena obstruct the proper investigation of electron-electron correlation effects.

Apart from the substitutional doping, interstitial doping with small positive ions such as Li⁺, H⁺, Mg⁺ and Al⁺ ions has been gaining a much interest [63,64] due to its potential applications in proton-based

devices, metal ion batteries and mottronics [65]. Protons (H^+) are the smallest ionic defects and hence can be reversibly inserted into the VO_2 lattice without destroying the lattice structure. Also, due to their low mass and ionic radii, devices based on H^+ and its transportation are expected to show lower operating voltage and higher speed of switching. Furthermore, the primary goal of current work is to achieve controlled modifications in the properties for advanced applications in electronic devices and proton-based devices using hydrogenation.

1.4.1 Hydrogenation in VO_2 thin films

Hydrogen, when reversibly intercalated into interstitial sites in vanadium dioxide provides a dynamic control of the phase transition. Most prominent methods of hydrogenating VO_2 thin films that have been reported are electrochemical insertion [66] and catalytic spillovers [65], out of which the catalytic spillover method is the most frequently used. Some recent reports suggested that the hydrogen doping in VO_2 stabilized the metallic phase at room temperature [67,68]. Moreover, Chen *et al.* observed the sequential insulator-metal-insulator phase transition by continuous hydrogen incorporation in the VO_2 thin films [66]. Jian *et al.* claimed the stabilized metallic phase up to 2K by direct atomic hydrogenation [69]. All the above reports are based on the conventional annealing method. However, due to the requirement of noble metal catalysts such as Au, Pt, Pd *etc.* and annealing in high temperature/pressure environment, such methods of hydrogenation are less feasible. The film is also left with a permanent sputtered metal on the surface. Recently, Chen *et al.* proposed a new facile method to hydrogenate the thin films *via* metal-acid contact [64]. This method was advantageous over the conventional methods. However, it was quite a time-consuming process. As mentioned earlier, one of the motives of this work is to provide better alternatives for *hydrogenation*.

1.4.1.1 Metal-acid contact method of hydrogenation

The underlying principle that governs the method in this work is depicted in the figure 1.5, when a low work function metal comes in the

contact with the VO_2 surface, the considerable difference in the work function of the two materials causes the electron from the metal to diffuse into the surface of the VO_2 thin films [64]. The electron-rich film is in contact with an ionic liquid (2 wt% H_2SO_4). The protons from the ionic solution start to diffuse into the surface and get intercalated into the lattice. Now there is a gradient of ions and electrons between the surface and the rest of the film. Thus, the process of transfer of electrons from the metal and in turn the surface diffusion of protons continues to progress into deeper layers of the films.

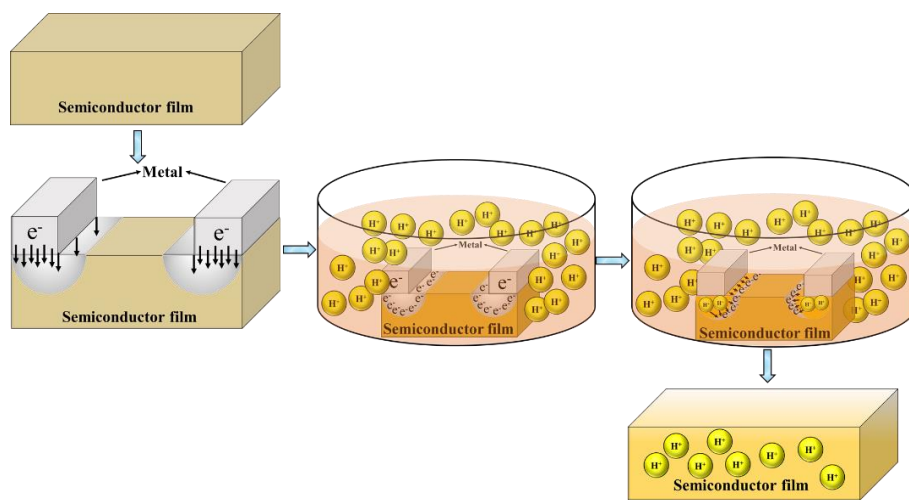


Figure 1.5: Schematic representation of metal-acid contact method.

In the present study, we have performed hydrogenation using the metal-acid contact method with some modification to achieve the rapid hydrogenation as per our motive, which has been further discussed in chapter 3 and chapter 4 of the thesis.

1.4.2 W doping in VO_2 thin films:

As discussed earlier, W doping is the most effective in modulating the MIT of VO_2 thin films [70–72]. Since W has +6 charge and V has +4 charge so due to the charge compensation, the formation of two pair of V^{3+} - V^{4+} and V^{3+} - W^{6+} take place, latter pair can donate two electrons to the system. Moreover, W substitutes the V ion and break the direct bonding between V-V which reduces the transition temperature [73]. Hence, tungsten doping is the most effective to reduce

the transition temperature. When the larger W^{6+} ions lodge themselves in the V^{4+} sites, the structure tends towards the more symmetric rutile structure. With the help of tungsten doping, we have successfully fine-tuned the structural and electronic properties which cannot only be used as per the suitable application but also be helpful in regulating and fastening the hydrogenation process. It is found that the structure of the films plays a key role in the hydrogenation. A detailed discussion is presented in the later chapters.

1.5 Objectives:

The detailed objectives of this work are as follows:

- I. To synthesize pure and crystallographically oriented VO_2 thin films by pulsed laser deposition.
- II. To investigate the methods of hydrogenation, improve the method for application purposes and understand the effects on MIT and other properties of VO_2 thin films.
- III. To tune the transition temperature by varying the doping percentage of tungsten(W), obtain a metallic state of VO_2 around room temperature for applications and study the effects on the temperature-dependent structural and electronic properties.

1.6 Organization of the Thesis

The above objectives of the work have been presented in the form of six chapters, including the introduction and conclusion. The briefing on chapter contents is given below:

Chapter 1 titled ‘Introduction’ presents a brief review of the transition metal oxides and their applications in smart devices. The material of interest, *i.e.*, VO_2 , has been explored in detail with its fundamental properties and applications. Metal-acid contact method used to hydrogenate the films have been discussed in detail.

Chapter 2 titled ‘Experimental and Characterization Techniques’ consists of a detail description of the experimental tools and methods that are used to synthesize and characterize the VO₂ thin films.

Chapter 3 comprises of the study for understanding the role of the crystal structure in accommodating the hydrogen in VO₂ thin films. For a comparative study, five VO₂ thin films were deposited on the single-crystal sapphire substrate under identical conditions. PLD technique was used to synthesize the crystallographically oriented thin films. VO₂ shows the structural transformation with increasing temperature. Hence, in order to study the effects of structure, hydrogenation *via* metal-acid contact method was tested on VO₂ at different temperature, and the treatment time was kept fixed.

Chapter 4 contains the study on the rapid hydrogenation *via* metal-acid contact method of VO₂ thin films using the mild electric fields in ionic solution at *room temperature*. The requirement of the high temperature in this method, as discussed in chapter 3, has been attempted to overcome through this study.

Chapter 5 describes the study on fine tuning of the structural and electronic properties of the VO₂ thin film *via* tungsten (W) doping. A series of seven V_{1-x}W_xO₂ ($x=0, 0.005, 0.01, 0.015, 0.02, 0.03, 0.04$) thin films were deposited on single-crystal sapphire substrates using PLD technique. Fractional doping of W can significantly transform the structure towards rutile. In chapter 3, we found that the hydrogen diffusion rate is found to be high in the rutile phase of VO₂. In this study, we have optimized the doping percentage to achieve a rutile phase at room temperature.

Chapter 6 titled ‘The Conclusion and Future Prospects’ summarize the concluding statements of the thesis and underline the future directions of the present study.

References:

- [1] W. Haensch, E.J. Nowak, R.H. Dennard, P.M. Solomon, A. Bryant, O.H. Dokumaci, A. Kumar, X. Wang, J.B. Johnson, M. V. Fischetti, Silicon CMOS devices beyond scaling, *IBM J. Res. Dev.*, 50 (2006), 339–361. (DOI: 10.1147/rd.504.0339).
- [2] K. Jeong, A.B. Kahng, A power-constrained MPU roadmap for the International Technology Roadmap for Semiconductors (ITRS), 2009 Int. SoC Des. Conf. ISOCC 2009, (2009), 49–52. (DOI:10.1109/SOCCDC.2009.5423856).
- [3] J. Fernández Rossier, Single-atom devices: Quantum engineering, *Nat. Mater.*, 12 (2013), 480–481. (DOI: 10.1038/nmat3670).
- [4] H. He, Metal oxide semiconductors and conductors, Elsevier Inc., (2020), 7-30 (DOI:10.1016/b978-0-12-814930-0.00002-5).
- [5] A. Pergament, G. Stefanovich, A. Velichko, Oxide Electronics and Vanadium Dioxide Perspective: A Review, *J. Sel. Top. Nano Electron. Comput.*, 1, (2013), 24–43. DOI:10.15393/j8.art.2013.3002).
- [6] Z. Yang, C. Ko, S. Ramanathan, Oxide electronics utilizing ultrafast metal-insulator transitions, *Annu. Rev. Mater. Res.* 41, (2011), 337–367. (DOI:10.1146/annurev-matsci-062910-100347).
- [7] R. Ramesh, D.G. Schlom, Whither oxide electronics, *MRS Bull.* 33, (2008), 1006–1014. (DOI:10.1557/mrs2008.220).
- [8] Z.R. Dai, Z.W. Pan, Z.L. Wang, Novel nanostructures of functional oxides synthesized by thermal evaporation, *Adv. Funct. Mater.*, 13, (2003), 9–24. (DOI:10.1002/adfm.200390013).
- [9] Z.L. Wang, Functional oxide nanobelts: Materials, properties and potential applications in nanosystems and biotechnology, *Annu.*

- Rev. Phys. Chem., 55, (2004), 159–196. (DOI:10.1146/annurev.physchem.55.091602.094416).
- [10] S.D. Ha, S. Ramanathan, Adaptive oxide electronics: A review, *J. Appl. Phys.*, 110, (2011), 071101. (DOI:10.1063/1.3640806).
- [11] A. Biswas, M. Talha, A. Kashir, Y.H. Jeong, A thin film perspective on quantum functional oxides, *Curr. Appl. Phys.*, 19, (2019), 207–214. (DOI:10.1016/j.cap.2018.07.013).
- [12] D. Yi, N. Lu, X. Chen, S. Shen, P. Yu, Engineering magnetism at functional oxides interfaces: Manganites and beyond, *J. Phys. Condens. Matter.*, 29, (2017), 443004. (DOI:10.1088/1361-648X/aa824d).
- [13] R. Citro, C. Noce, S. Pagano, F. Forte, V. Granata, A. Leo, Superconductivity and functional oxides, *Eur. Phys. J. Spec. Top.*, 228, (2019), 625–629. (DOI:10.1140/epjst/e2019-0084s-9).
- [14] D. Zappa, A. Bertuna, E. Comini, N. Kaur, N. Poli, V. Sberveglieri, G. Sberveglieri, Metal oxide nanostructures: Preparation, characterization and functional applications as chemical sensors, *Beilstein J. Nanotechnol.*, 8, (2017), 1205–1217. (DOI:10.3762/bjnano.8.122).
- [15] C.H. Ahn, K.M. Rabe, J.M. Triscone, Ferroelectricity at the Nanoscale: Local Polarization in Oxide Thin Films and Heterostructures, *Science.*, 303, (2004), 488–491. (DOI:10.1126/science.1092508).
- [16] R.S. Devan, R.A. Patil, J.H. Lin, Y.R. Ma, One-dimensional metal-oxide nanostructures: Recent developments in synthesis, characterization, and applications, *Adv. Funct. Mater.*, 22, (2012) 3326–3370. (DOI:10.1002/adfm.201201008).
- [17] R. Jose, V. Thavasi, S. Ramakrishna, Metal oxides for dye-sensitized solar cells, *J. Am. Ceram. Soc.*, 92, (2009), 289–301. (DOI:10.1111/j.1551-2916.2008.02870.x).

- [18] A.M. Abdalla, S. Hossain, A.T. Azad, P.M.I. Petra, F. Begum, S.G. Eriksson, A.K. Azad, Nanomaterials for solid oxide fuel cells: A review, *Renew. Sustain. Energy Rev.*, 82, (2018), 353–368. (DOI:10.1016/j.rser.2017.09.046).
- [19] R. Agrawal, H.D. Espinosa, Giant piezoelectric size effects in zinc oxide and gallium nitride nanowires. A first principles investigation, *Nano Lett.*, 11, (2011), 786–790. (DOI:10.1021/nl104004d).
- [20] N. Yamazoe, G. Sakai, K. Shimano, Oxide semiconductor gas sensors, *Catal. Surv. from Asia.*, 7, (2003), 63–75. (DOI:10.1023/A:1023436725457).
- [21] F.J. Morin, Oxides which show a metal-to-insulator transition at the neel temperature, *Phys. Rev. Lett.*, 3, (1959), 34–36. (DOI:10.1103/PhysRevLett.3.34).
- [22] T. Hajlaoui, N. Émond, C. Quirouette, B. Le Drogoff, J. Margot, M. Chaker, Metal–insulator transition temperature of boron-doped VO₂ thin films grown by reactive pulsed laser deposition, *Scr. Mater.*, 177, (2020), 32–37. (DOI:10.1016/j.scriptamat.2019.09.019).
- [23] D. Gu, X. Zhou, Z. Sun, Y. Jiang, Influence of Gadolinium-doping on the microstructures and phase transition characteristics of VO₂ thin films, *J. Alloys Compd.*, 705, (2017), 64–69. (DOI:10.1016/j.jallcom.2017.02.138).
- [24] B. Rajeswaran, A.M. Umarji, Effect of W addition on the electrical switching of VO₂ thin films, *AIP Adv.*, 6, (2016), 035215. (DOI:10.1063/1.4944855).
- [25] N. Wang, M. Duchamp, R.E. Dunin-Borkowski, S. Liu, X. Zeng, X. Cao, Y. Long, Terbium-Doped VO₂ Thin Films: Reduced Phase Transition Temperature and Largely Enhanced Luminous Transmittance, *Langmuir.*, 32, (2016), 759–764.

- (DOI:10.1021/acs.langmuir.5b04212).
- [26] B.G. Chae, H.T. Kim, S.J. Yun, Characteristics of W- and Ti-doped VO₂ thin films prepared by sol-gel method, *Electrochem. Solid - State Lett.*, 11, (2008), D53–D55. (DOI:10.1149/1.2903208).
- [27] X. Liu, S.W. Wang, F. Chen, L. Yu, X. Chen, Tuning phase transition temperature of VO₂ thin films by annealing atmosphere, *J. Phys. D. Appl. Phys.*, 48, (2015), 265104. (DOI:10.1088/0022-3727/48/26/265104).
- [28] H.Y. Xu, Y.H. Huang, S. Liu, K.W. Xu, F. Ma, P.K. Chu, Effects of annealing ambient on oxygen vacancies and phase transition temperature of VO₂ thin films, *RSC Adv.*, 6, (2016), 79383–79388. (DOI:10.1039/c6ra13189a).
- [29] B. Hong, Y. Yang, K. Hu, Y. Dong, J. Zhou, Y. Zhang, W. Zhao, Z. Luo, C. Gao, Strain engineering on the metal-insulator transition of VO₂/TiO₂ epitaxial films dependent on the strain state of vanadium dimers, *Appl. Phys. Lett.*, 115, (2019), 251605. (DOI:10.1063/1.5121876).
- [30] A. Moatti, R. Sachan, V.R. Cooper, J. Narayan, Electrical Transition in Isostructural VO₂ Thin-Film Heterostructures, *Sci. Rep.*, 9, (2019), 3009. (DOI:10.1038/s41598-019-39529-z).
- [31] P. Shvets, O. Dikaya, K. Maksimova, A. Goikhman, A review of Raman spectroscopy of vanadium oxides, *J. Raman Spectrosc.*, 50, (2019), 1226–1244. DOI:10.1002/jrs.5616).
- [32] S. Yu, S. Wang, M. Lu, L. Zuo, A metal-insulator transition study of VO₂ thin films grown on sapphire substrates, *J. Appl. Phys.*, 122, (2017), 235102. (DOI:10.1063/1.4997437).
- [33] P.R. Zhu, S. Yamamoto, A. Miyashita, H. Naramoto, Pulsed laser deposition of VO₂ single crystal thin films on sapphire substrates, *Chinese Phys. Lett.*, 15, (1998), 904–906. (DOI:10.1088/0256-

307X/15/12/016).

- [34] G. Garry, O. Durand, A. Lordereau, Structural, electrical and optical properties of pulsed laser deposited VO₂ thin films on R- and C-sapphire planes, *Thin Solid Films.*, 453–454, (2004), 427–430. (DOI:10.1016/j.tsf.2003.11.118).
- [35] K. Liu, S. Lee, S. Yang, O. Delaire, J. Wu, Recent progresses on physics and applications of vanadium dioxide, *Mater. Today.*, 21, (2018), 875–896. (DOI:10.1016/j.mattod.2018.03.029).
- [36] M. Pan, J. Liu, H. Zhong, S. Wang, Z.F. Li, X. Chen, W. Lu, Raman study of the phase transition in VO₂ thin films, *J. Cryst. Growth.*, 268, (2004), 178–183. (DOI:10.1016/j.jcrysgro.2004.05.005).
- [37] Y. Huang, D. Zhang, Y. Liu, J. Jin, Y. Yang, T. Chen, H. Guan, P. Fan, W. Lv, Phase transition analysis of thermochromic VO₂ thin films by temperature-dependent Raman scattering and ellipsometry, *Appl. Surf. Sci.*, 456, (2018), 545–551. (DOI:10.1016/j.apsusc.2018.06.125).
- [38] D.J. Late, S.N. Shirodkar, U. V. Waghmare, V.P. Dravid, C.N.R. Rao, Thermal expansion, anharmonicity and temperature-dependent Raman spectra of single- and few-layer MoSe₂ and WSe₂, *Chem Phys Chem.*, 15, (2014), 1592–1598. (DOI:10.1002/cphc.201400020).
- [39] J.B. Goodenough, The two components of the crystallographic transition in VO₂, *J. Solid State Chem.*, 3, (1971), 490–500. (DOI:10.1016/0022-4596(71)90091-0).
- [40] A. Moatti, R. Sachan, J. Prater, J. Narayan, Control of Structural and Electrical Transitions of VO₂ Thin Films, *ACS Appl. Mater. Interfaces.*, 9, (2017), 24298–24307. (DOI:10.1021/acsami.7b05620).
- [41] F. Grandi, A. Amaricci, M. Fabrizio, Unraveling the Mott-Peierls

- intrigue in vanadium dioxide, *Phys. Rev. Res.*, 2, (2020), 013298. (DOI:10.1103/physrevresearch.2.013298).
- [42] S. Xu, X. Shen, K.A. Hallman, R.F. Haglund, S.T. Pantelides, Unified band-theoretic description of structural, electronic, and magnetic properties of vanadium dioxide phases, *Phys. Rev. B.*, 95, (2017), 125105. (DOI:10.1103/PhysRevB.95.125105).
- [43] C. Weber, D.D. O'Regan, N.D.M. Hine, M.C. Payne, G. Kotliar, P.B. Littlewood, vanadium dioxide: A peierls-mott insulator stable against disorder, *Phys. Rev. Lett.*, 108, (2012), 256402. (DOI:10.1103/PhysRevLett.108.256402).
- [44] Z. Shao, X. Cao, H. Luo, P. Jin, Recent progress in the phase-transition mechanism and modulation of vanadium dioxide materials, *NPG Asia Mater.*, 10, (2018), 581–605. (DOI:10.1038/s41427-018-0061-2).
- [45] J.P. Pouget, H. Launois, Metal-Insulator Phase Transition in VO₂, *Le J. Phys. Colloq.*, 37, (1976), C4-49-C4-57. (DOI:10.1051/jphyscol:1976408).
- [46] J.P. Pouget, T. M. Rice, H. Launois, Comment on “VO₂: Peierls or Mott-Hubbard? A View from Band Theory,” *Phys. Rev. Lett.*, 73, (1994), 3042. (DOI:10.1103/PhysRevLett.73.3042).
- [47] T.J. Huffman, C. Hendriks, E.J. Walter, J. Yoon, H. Ju, R. Smith, G.L. Carr, H. Krakauer, M.M. Qazilbash, Insulating phases of vanadium dioxide are Mott-Hubbard insulators, *Phys. Rev. B.*, 95, (2017), 075125. (DOI:10.1103/PhysRevB.95.075125).
- [48] M. Soltani, M. Chaker, E. Haddad, R. V. Kruzelecky, J. Margot, Effects of Ti-W codoping on the optical and electrical switching of vanadium dioxide thin films grown by a reactive pulsed laser deposition, *Appl. Phys. Lett.*, 85, (2004), 1958–1960. (DOI:10.1063/1.1788883).
- [49] H. Zhou, J. Li, Y. Xin, G. Sun, S. Bao, P. Jin, Optical and

- electrical switching properties of VO₂ thin film on MgF₂ (111) substrate, *Ceram. Int.*, 42, (2016), 7655–7663. (DOI:10.1016/j.ceramint.2016.01.178).
- [50] F. Béteille, J. Livage, Optical Switching in VO₂ Thin Films, *J. Sol-Gel Sci. Technol.*, 13, (1998), 915–921. (DOI:10.1023/a:1008679408509).
- [51] L. Pellegrino, N. Manca, T. Kanki, H. Tanaka, M. Biasotti, E. Bellingeri, A.S. Siri, D. Marré, Multistate memory devices based on free-standing VO₂/TiO₂ microstructures driven by Joule self-heating, *Adv. Mater.*, 24, (2012), 2929–2934. (DOI:10.1002/adma.201104669).
- [52] L. Fan, Y. Chen, Q. Liu, S. Chen, L. Zhu, Q. Meng, B. Wang, Q. Zhang, H. Ren, C. Zou, Infrared Response and Optoelectronic Memory Device Fabrication Based on Epitaxial VO₂ Film, *ACS Appl. Mater. Interfaces.*, 8, (2016), 32971–32977. (DOI:10.1021/acsami.6b12831).
- [53] T. Driscoll, H.T. Kim, B.G. Chae, M. Di Ventra, D.N. Basov, Phase-transition driven memristive system, *Appl. Phys. Lett.*, 95, (2009), 043503. (DOI:10.1063/1.3187531).
- [54] F. Xu, X. Cao, H. Luo, P. Jin, Recent advances in VO₂ - based thermochromic composites for smart windows, *J. Mater. Chem. C.*, 6, (2018), 1903–1919. (DOI:10.1039/c7tc05768g).
- [55] J. Zhou, Y. Gao, Z. Zhang, H. Luo, C. Cao, Z. Chen, L. Dai, X. Liu, VO₂ thermochromic smart window for energy savings and generation, *Sci. Rep.*, 3, (2013), 3029. (DOI:10.1038/srep03029).
- [56] E. Merced, D. Torres, X. Tan, N. Sepúlveda, An electrothermally actuated VO₂ - based MEMS using self-sensing feedback control, *J. Microelectromechanical Syst.*, 24, (2015), 100–107. (DOI:10.1109/JMEMS.2014.2317944).
- [57] A. Simo, K. Kaviyarasu, B. Mwakikunga, R. Madjoe, A. Gibaud,

- M. Maaza, Phase transition study in strongly correlated VO₂ based sensing systems, *J. Electron Spectros. Relat. Phenomena.*, 216, (2017), 23–32. (DOI:10.1016/j.elspec.2017.01.011).
- [58] R. Shi, X. Cai, W. Wang, J. Wang, D. Kong, N. Cai, P. Chen, P. He, Z. Wu, A. Amini, N. Wang, C. Cheng, Single-Crystalline Vanadium Dioxide Actuators, *Adv. Funct. Mater.*, 29, (2019), 1900527.(DOI:10.1002/adfm.201900527).
- [59] M.A. Belyaev, V. V. Putrolaynen, A.A. Velichko, G.B. Stefanovich, A.L. Pergament, Field-effect modulation of resistance in VO₂ thin film at lower temperature, *Jpn. J. Appl. Phys.*, 53, (2014), 111102. (DOI:10.7567/JJAP.53.111102).
- [60] M. Nakano, K. Shibuya, N. Ogawa, T. Hatano, M. Kawasaki, Y. Iwasa, Y. Tokura, Infrared-sensitive electrochromic device based on VO₂, *Appl. Phys. Lett.*, 103, (2013), 153503. (DOI:10.1063/1.4824621).
- [61] Z. Yang, Y. Zhou, S. Ramanathan, Studies on room-temperature electric-field effect in ionic-liquid gated VO₂ three-terminal devices, *J. Appl. Phys.*, 111, (2012), 014506. (DOI:10.1063/1.3665399).
- [62] W. Zeng, N. Chen, W. Xie, Research progress on the preparation methods for VO₂ nanoparticles and their application in smart windows, *Cryst Eng Comm.*, 22, (2020), 851–869. (DOI:10.1039/c9ce01655d).
- [63] X. Xu, F. Xiong, J. Meng, X. Wang, C. Niu, Q. An, L. Mai, Vanadium-Based Nanomaterials: A Promising Family for Emerging Metal-Ion Batteries, *Adv. Funct. Mater.*, 30, (2020), 1904398. (DOI:10.1002/adfm.201904398).
- [64] Y. Chen, Z. Wang, S. Chen, H. Ren, L. Wang, G. Zhang, Y. Lu, J. Jiang, C. Zou, Y. Luo, Non-catalytic hydrogenation of VO₂ in acid solution, *Nat. Commun.*, 9, (2018), 818.

(DOI:10.1038/s41467-018-03292-y).

- [65] H. Yoon, M. Choi, T.W. Lim, H. Kwon, K. Ihm, J.K. Kim, S.Y. Choi, J. Son, Reversible phase modulation and hydrogen storage in multivalent VO₂ epitaxial thin films, *Nat. Mater.*, 15, (2016), 1113–1119.(DOI:10.1038/nmat4692).
- [66] S. Chen, Z. Wang, L. Fan, Y. Chen, H. Ren, H. Ji, D. Natelson, Y. Huang, J. Jiang, C. Zou, Sequential insulator-metal-insulator phase transitions of VO₂ triggered by hydrogen doping, *Phys. Rev. B.*, 96, (2017), 125130. (DOI:10.1103/PhysRevB.96.125130).
- [67] C. Wu, F. Feng, J. Feng, J. Dai, L. Peng, J. Zhao, J. Yang, C. Si, Z. Wu, Y. Xie, Hydrogen-incorporation stabilization of metallic VO₂ (R) phase to room temperature, displaying promising low-temperature thermoelectric effect, *J. Am. Chem. Soc.*, 133, (2011), 13798–13801. (DOI:10.1021/ja203186f).
- [68] J. Wei, H. Ji, W. Guo, A.H. Nevidomskyy, D. Natelson, Hydrogen stabilization of metallic vanadium dioxide in single-crystal nanobeams, *Nat. Nanotechnol.*, 7, (2012), 357–362. (DOI:10.1038/nnano.2012.70).
- [69] J. Lin, H. Ji, M.W. Swift, W.J. Hardy, Z. Peng, X. Fan, A.H. Nevidomskyy, J.M. Tour, D. Natelson, Hydrogen diffusion and stabilization in single-crystal VO₂ Micro/Nanobeams by direct atomic hydrogenation, *Nano Lett.*, 14, (2014), 5445–5451. (DOI:10.1021/nl5030694).
- [70] B.G. Chae, H.T. Kim, S.J. Yun, Characteristics of W-and Ti-doped VO₂ thin films prepared by sol-gel method, *Electrochem. Solid-State Lett.*, 11, (2008), 53–55. (DOI:10.1149/1.2903208).
- [71] B. Li, S. Tian, H. Tao, X. Zhao, Tungsten doped M-phase VO₂ mesoporous nanocrystals with enhanced comprehensive thermochromic properties for smart windows, *Ceram. Int.*, 45,

- (2019), 4342–4350. (DOI:10.1016/j.ceramint.2018.11.109).
- [72] S.S. Majid, S.R. Sahu, A. Ahad, K. Dey, K. Gautam, F. Rahman, P. Behera, U. Deshpande, V.G. Sathe, D.K. Shukla, Role of V-V dimerization in the insulator-metal transition and optical transmittance of pure and doped VO₂ thin films, *Phys. Rev. B.*, 101, (2020), 014108. (DOI:10.1103/PhysRevB.101.014108).
- [73] C. Tang, P. Georgopoulos, M. E. Fine, J.B.Cohen, M.Nygren, G.S.Knapp,A.Aldred, Local atomic and electronic arrangements in W_xV_{1-x}O₂, *Phys. Rev. B.*, 31, (1985), 1000–1011. (DOI:10.1103/PhysRevB.31.1000).

Chapter 2

Experimental and Characterization Techniques

This chapter describes the experimental techniques used for VO₂ thin films synthesis and the characterization techniques used for the present thesis work. The bulk synthesis by solid-state reaction and thin-film synthesis using pulsed laser deposition (PLD) has been elaborated with the necessary pictures and diagrams. The hydrogenation procedure *via* a metal-acid contact method has been discussed. This method has been modified for rapid hydrogenation in the present work and described in this chapter. Characterization techniques such as X-ray Diffraction (XRD), X-ray reflectivity (XRR), Raman Spectroscopy, Atomic Force Microscopy (AFM), X-ray Photoelectron Spectroscopy (XPS), and DC resistivity have been described. For each characterization, a brief introduction about the experimental setup along with the working principle, has been discussed.

2.1 Synthesis methods

The synthesis methods are explained in two parts, as follows:

Part I: Synthesis of bulk using solid-state reaction method.

Part II: Synthesis of thin films by pulsed laser deposition (PLD) method.

2.1.1 Synthesis of bulk material

The bulk materials (*i.e.* pellets) have been synthesized using solid-state reaction route. This method is solvent-free and a widely used conventional method for making the bulk material of oxides. For the present work, V_2O_3 and WO_3 (99.99% pure, Aldrich) powders have been used to make the pellets. For undoped pellet, the powder grinding was done for 30 min of duration. For tungsten (W) doped study, V_2O_3 and WO_3 were taken appropriately by the weighing of powders in an analytical balance., and to make the homogeneous mixture, the powder grinding was done for 3-4 h using a mortar pestle. After proper mixing of powder in the appropriate ratio, the pellets were made using the die-set of the 15 mm diameter. To make the pellet, the powder was pressed with the 5 ton of pressure using the hydraulic press (PCI Analytics, India). All the pellets with different doping content were kept into the tubular furnace simultaneously for sintering, in order to maintain the same atmosphere for all the pellets. These pellets were then sintered at 1000°C for 24 h in the Argon (Ar) atmosphere with the same cooling and heating rate in a controlled manner. This procedure can be summarized in the following steps:

- Weighing and mixing of powders in appropriate molar ratio.
- Grinding of the powders to get a homogeneous mixture.
- Pellet formation and sintering at a higher temperature in the required atmosphere.

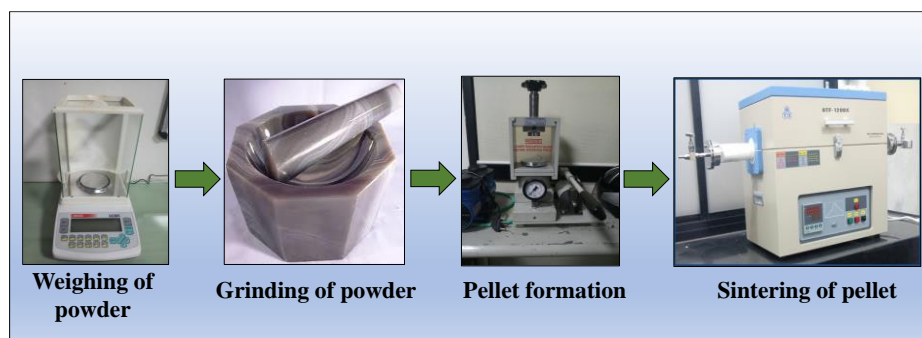


Figure 2.1: Different stages of solid-state reaction route.

For the present study, a total of 7 bulk pellets have been synthesized to prepare thin films of pure VO₂ and W-doped VO₂.

2.1.2 Synthesis of thin films

The thin films have been synthesized using the pulsed laser deposition (PLD) technique. PLD is known for the synthesis of the epitaxial and crystallographically oriented thin films. In order to understand the importance of the PLD grown thin films, it is important to discuss the geometrical system of the PLD and how it works.

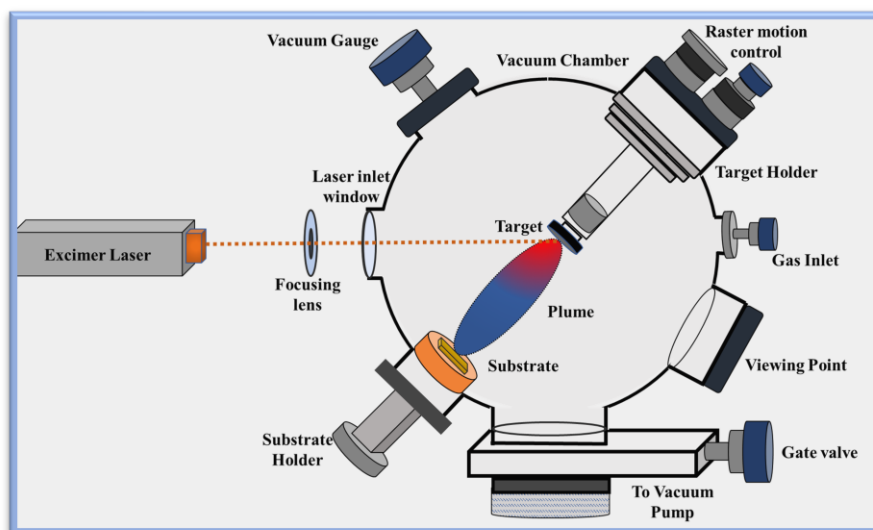


Figure 2.2: Schematic of the experimental setup of PLD.

High-temperature synthesis of nanomaterials was being studied for a longer time, and with the best available sources for fabricating thin films, PLD was studied due to its versatile effect in the thin film fabrications. In the year 1987, T Venkatesan innovated pulsed laser

deposition for the above requirements [1]. Some other major techniques for these set of depositions are sputtered deposition, electron beam physical vapor deposition and evaporation-based deposition, *etc.* [2].

Deposition *via* PLD can be basically understood by following steps: Firstly, the interaction between the laser beam and the target material inside the chamber. Secondly, the emergence of plasma plume with the best acquitted conditions for the thin films to grow and lastly nucleation and growth of the thin film onto the substrate by keeping the temperature and distance of the substrate from the target discrete in nature.

2.1.2.1 Experimental setup of PLD

The first and foremost requirement of the PLD method is laser source, a high-power pulsed laser such as ND: YAG, ArF, KrF *etc.* can be used to ablate the target material to deposit the desired crystallographically oriented films. KrF is the most widely used suitable excimer laser source for the PLD. In the present study, KrF laser of a wavelength of the 248 nm was used.

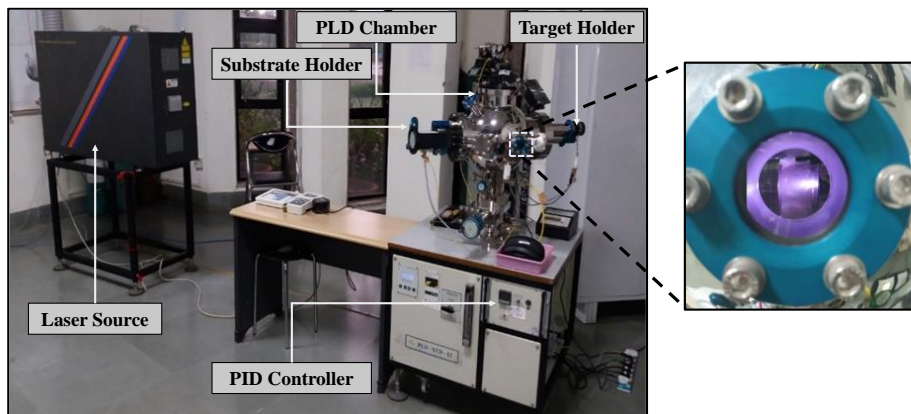


Figure 2.3: PLD setup with plume formation during deposition of VO₂ thin film.

The chamber with an ultra-high vacuum is processed by controlling the gas concentration and vacuum level externally. Once the condition is optimum, the laser interacts with the target material. The vacuum chamber consists of holders for target and substrate, which are

usually made up of stainless steel. The raster and rotational motion of the target are controlled with the help of programmed holder; this enables to have a uniform laser ablation of the target material [3]. The substrate holder is equipped with the heater mechanism to maintain deposition temperature during the growth of the thin film. These holders are separated with a specific distance target holder.

Initially, when the beam interacts with the materials under sufficient temperature and optimum vacuum conditions, plasma plume of material is formed. When the absorbed laser energy (E_{ab}) is greater than the binding energy (E_b) of single atom on the top surface of the target materials *i.e.* $E_{ab} > E_b$, elliptical or circular shape plumes are directed towards the substrate in the chamber which are caused due to the ions present in the plasma plumes inside the chamber. The shape can be altered by controlling the partial pressure of the inlet gas, adjusting the partial pressure will adjust the kinetic energy and the scattering rate of the plasma plumes therefore giving an appropriate room for thin-film growth.

2.1.2.2 Thin film growth mechanism in PLD

Growth of thin-film close to the thermodynamic analysis can be understood by Volmer-Weber, Frank-van der Merwe and Stranski-Krastinov modes of nucleation and growth, as shown in figure 2.3. These modes are well governed by free energies of the film surface (γ_f), substrate surface (γ_s) and the interface between substrate and film (γ_i). Total surface energy is greater than the substrate energy $\gamma_f + \gamma_i > \gamma_s$ which causes the three-dimensional islands and no interaction between the films and the substrate was subjected by Volmer-Weber mode [4,5]. Frank Van Der Merwe growth talks about the situation when $\gamma_f + \gamma_i < \gamma_s$; full monolayers with strong bonding between films and substrate is evidently giving a homoepitaxial thin film growth [6]. Stranski-Krastinov modes are prescribed for heteroepitaxial growth which is caused due to lattice mismatch between the substrate and deposited thin film [7,8].

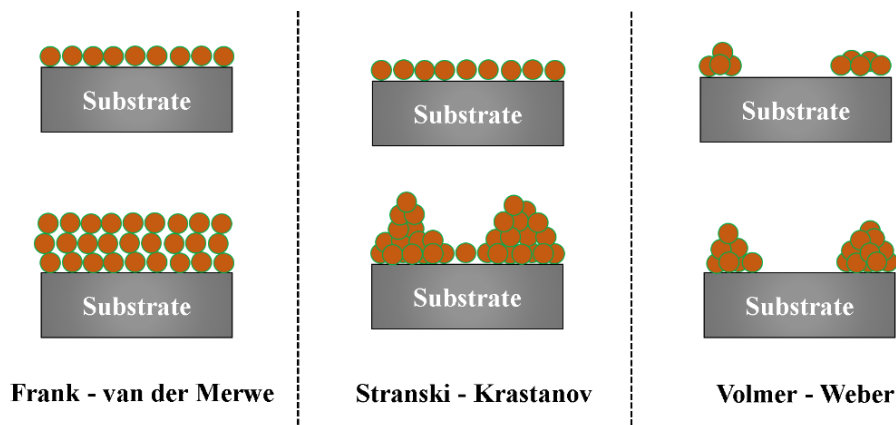


Figure 2.4: Schematic diagram for nucleation and growth modes of thin films.

The energy fluence is the key parameter for the deposition and can be defined as pulse energy over the irradiated area, which gets affected by the size of the beam. There are various other external factors that can influence the growth of the thin films; laser energy, gas pressure, the distance between target and substrate and holding temperature of the substrate.

2.2 Hydrogenation procedure:

As discussed in chapter 1, we have opted the metal-acid contact method to hydrogenate the film for our present study. Our motive was to propose one facile method to achieve rapid hydrogenation *via* easy approach. We have modified the metal-acid contact method for rapid hydrogenation in two different ways; the said method was tested (i) at different temperatures, and (ii) under different mild electric fields.

As the name suggests, for a metal-acid contact method, a suitable metal on the surface of the thin film and an acidic solution acting as a source of the H^+ ions for hydrogenation or hydrogen doping are required. In the present study, the low work function metal Aluminum (Al) is used, and 2 wt% H_2SO_4 (sulfuric acid) have been used as an ionic liquid. Firstly, to hydrogenate the film, we have used the Al foil to make the detachable electrode-like structures on the edges of the films surface and then kept it in the acidic solution for 30 s.

(i) **At different temperature:** In order to study the role of the crystal structure, we chose four different temperatures *i.e.*, 303 K, 313 K (before transition) and 333 K, 343 K (after transition). For this study, five VO₂ thin films were synthesized simultaneously; one was kept as it is, and four were hydrogenated at four different temperatures. Firstly, the optimization of the hot-plate temperature was done for the acidic solution to achieve the desired temperature. After optimization of temperature, to hydrogenate the film at a particular temperature, two petri dishes were taken and kept it on the hot-plate. The prepared film with Al contacts was kept in one dish and acidic solution in another dish at an optimized temperature. After the stabilization of the film and acidic solution, the film was transferred in the acidic solution and kept inside only for 30 s, as shown in figure 2.5. As a result, we found efficiently rapid hydrogenation, which has been discussed in chapter 3.

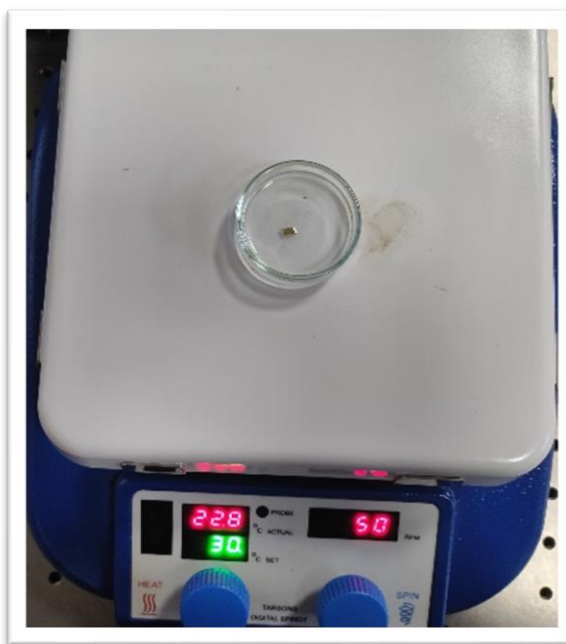


Figure 2.5: Hydrogenation *via* metal-acid contact method at a particular temperature.

(ii) **Under different mild electric fields:** To hydrogenate the films under different electric fields, one self-assembled setup was designed, as shown in figure 2.6. The arrangement of two electrodes was made in the beaker and to provide the mild electric fields; a Keithley source

meter was used. The prepared thin film with Al contact was attached to the negative electrode, and on the positive electrode, Cu plate of 0.1 mm thickness was affixed. These two electrodes were kept in the acidic solution in the beaker and then using the Keithley source meter, a particular voltage was applied to the electrodes only for 30 s at *room temperature*. With a very mild applied voltage, we found remarkable results which have been shown in chapter 4 of the thesis.



Figure 2.6: Hydrogenation *via* metal-acid contact method under a mild electric field.

2.3 Characterization techniques:

2.3.1 X-ray Diffraction (XRD):

X-ray diffraction is one of the most common techniques used for material characterization to obtain information on the atomic scale for both crystalline and non-crystalline materials [9]. It was discovered in 1912 by Max von Laue and W. L. Bragg and his father W. H. Bragg. Since the wavelength of X-rays is of the order of $\sim \text{\AA}$, which is comparable to lattice spacing, it is a very suitable tool to probe the structure of materials [10]. We can get information about crystallite size,

lattice parameters, lattice strain, chemical composition, state of order, the spacing between two crystal planes *etc.* using XRD.

Working principle:

First of all, the filament inside the cathode tube is heated by applying the alternating voltage between two electrodes. As the filament gets heated then free electrons travel from cathode to anode with higher velocity and finally strike to the anode surface, this results in the creation of X-rays in the X-ray tube. These X-rays originated from the tube fall on the surface of the sample. The wavelength of these originated X-rays is of the order of the lattice parameter which results the diffraction of X-rays in different directions by continuous change in intensity with the incident angle. The X-ray diffraction technique is basically based on the principle of Bragg’s law [11].

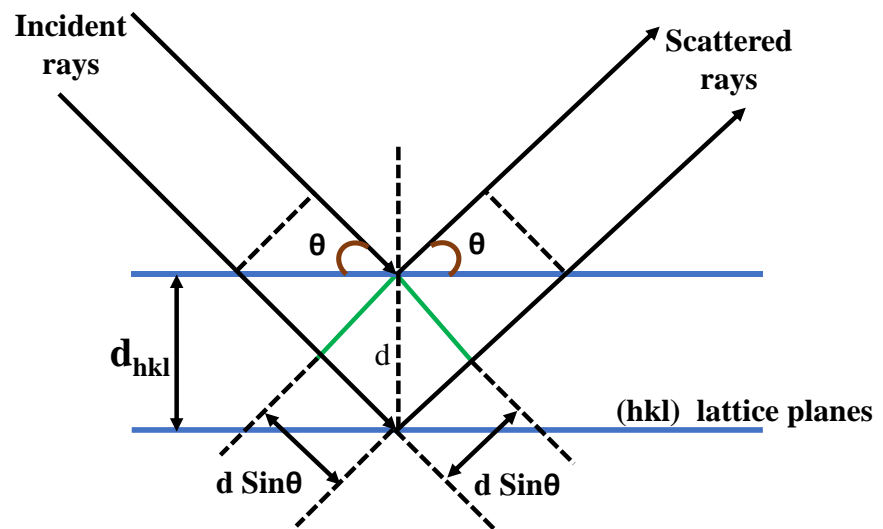


Figure 2.7: Diffraction of X-ray by crystals.

For constructive interference, path difference should be an integral multiple of wavelength λ . So, the Bragg’s condition for constructive interference is given as,

$$2d \sin\theta = n\lambda, \text{ where } n \text{ is an integer.} \tag{2.1}$$

Whenever this condition is satisfied, a diffraction peak will occur in the diffraction pattern. So, Bragg’s law states that only for the angle θ

satisfying Brag's law $2d\sin\theta = \lambda$ there is constructive interference. For all other angles, the intensity of peaks should cancel out.

The intensity of these X-ray diffracted peaks depends on the electron density across the diffracting miller plane. So, the intensity distribution varies with the angle between the incident and diffracted beam. By knowing those planes, we can calculate the structure of a sample, composition of the crystal, spacing between two planes, lattice constant *etc.* Schematic of a typical XRD set up is shown in figure 2.8. Different types of scans are possible using XRD depending upon the type of information to be extracted [12].

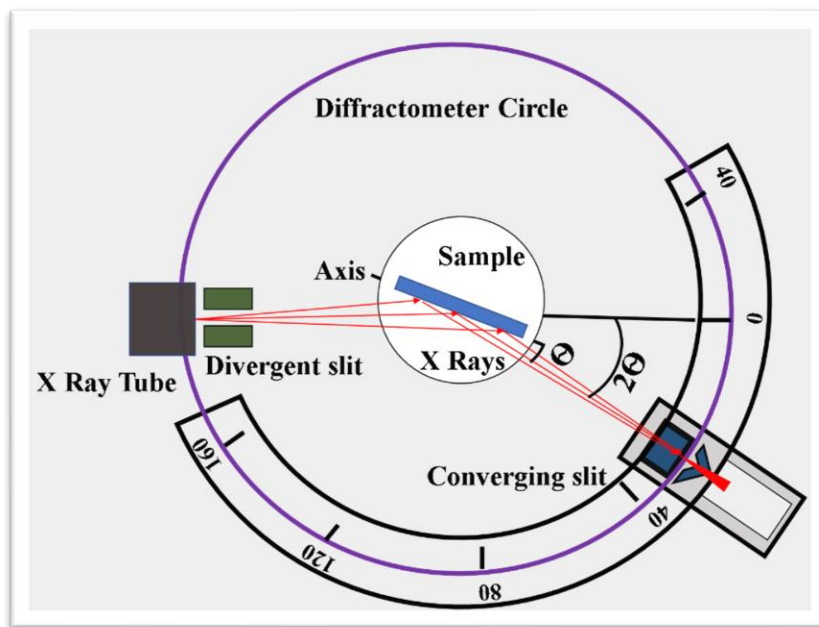


Figure 2.8: Schematic of the X-ray diffraction (XRD).

2.3.2 X-ray Reflectivity (XRR):

X-ray reflectivity is a vital characterization technique for studies related to structure and thickness of thin films grown at nanometer scale onto the substrate. XRR measurement basically features for following characteristics: (i) determination of layered structures, *i.e.* from few layers to multilayers, (ii) thickness of the films can be evaluated from the spectra and (iii) for determining the interface roughness and electron density of thin films can also be calculated.

Working principle:

The interaction between the X-rays and the objective can be equated with the help of index of refraction (n), it changes the direction as it passes from air to the material. While understanding the phenomena and the behavior we know that the refractive index of the material is less than unity [13]. Thus, when X-rays pass through the air to the material, it tends to reflect from the surface if the incident angle, θ_i (*i.e.* the angle between the incidence beam and the adjacent surface of the sample) is lesser than the critical angle θ_c . This phenomenon of total external reflection is the main cause for the study of the thin films [14].

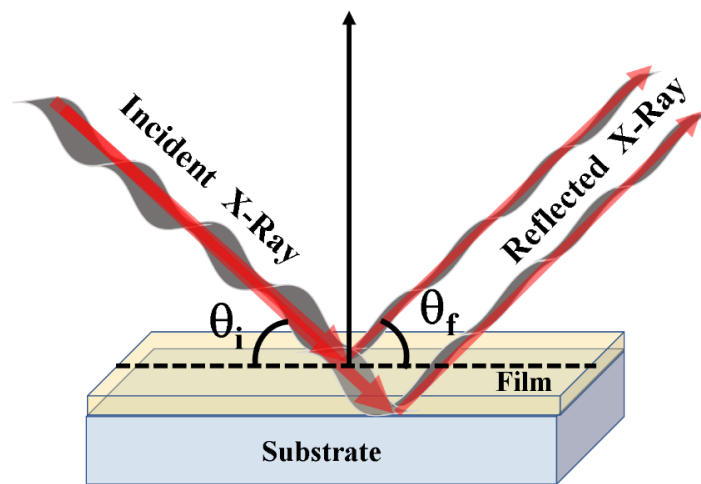


Figure 2.9: Schematic representation of XRR geometry.

The substrate and thin-film interface reflect the rays which are joined by the rays getting reflected from the top surface of the thin film and causing the interference of the reflected X-rays. This interference of X-ray produces the reflectivity profile with several oscillations. These oscillations were first noticed by scientist Kiessig in 1931 and are called Kiessig fringes [15]. The occurrence of oscillations depicts various information like the film's thickness; a shorter period of oscillations is ascribed to thicker films. The amplitude of oscillations is engaged to show the difference between the electron densities of the substrate and films [16]. The intensity of the X-ray also informs us about the

roughness of the films as the intensity decreases; it tends to have a higher surface roughness.

2.3.3 Raman spectroscopy:

Raman spectroscopy is based on the scattering phenomenon wherein a monochromatic beam of radiation, incident on a sample is scattered from it. When the scattering occurs with no energy loss, the frequency of the scattered beam is same as the frequency of the incident beam, this is known as Rayleigh scattering (Elastic scattering), whereas when the energy (frequency) of the radiation changes during the scattering process such kind of scattering is known as Raman scattering. (Inelastic scattering) (figure 2.10) and was first discovered by sir C.V. Raman and his collaborator K.S. Krishnan in 1928 [17]. Raman Effect, as defined above, is an inelastic scattering (change of energy) of light from the atomic vibrations (phonons). Raman spectroscopy is a powerful tool which measures how atoms vibrate about their equilibrium positions and provide valuable information about microstructural properties, *i.e.* crystal structure, detailed information about the chemical composition and the nature of chemical bonds can be obtained [18].

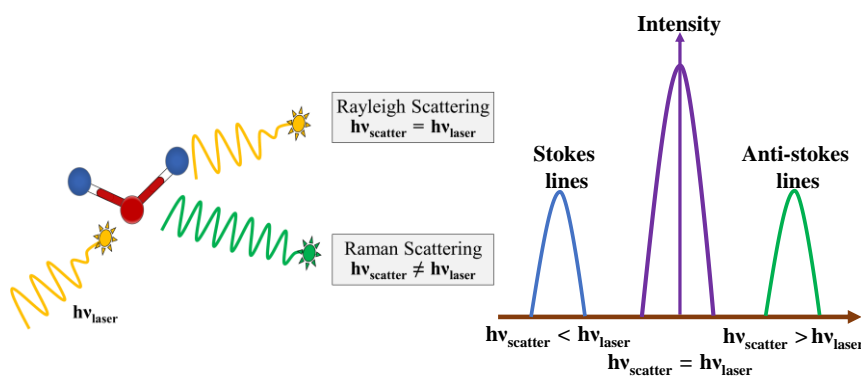


Figure 2.10: Schematic representation of the Rayleigh, Stokes and anti-Stokes Raman lines.

Raman scattering is a consequence of inelastic scattering of the incident photons, where energy is either received from or transferred to the sample, as a result of a change in the vibrational and rotational modes

of the sample causing a change in the energy, and therefore, the frequency of the light scattered. The changes in the energy are observed in the form of discrete lines in the scattered light above and below the Rayleigh line (same frequency as the incident light) is called anti-Stokes and Stokes lines, respectively [18].

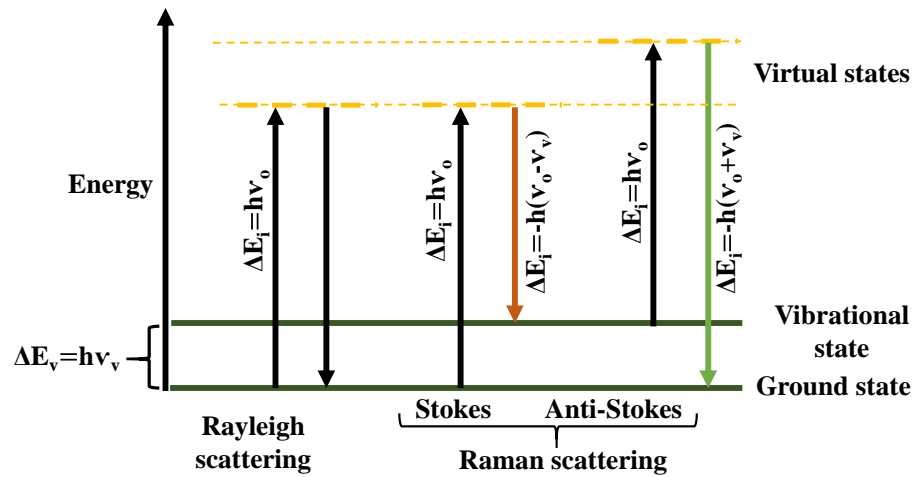


Figure 2.11: Energy relation for Rayleigh scattering, Stokes and anti-Stokes scattering.

In a crystal lattice, a photon interacts with the lattice phonons. When the incident photon transfers energy to the sample, the phonon excites to the higher vibrational energy level, then the change (Raman shift) in the energy (frequency) of phonons is known as Stokes shift. Alternatively, if a molecule is previously in an excited state, an incident photon may lead to the de-excitation of lattice phonon to lower vibrational energy level, and the corresponding scattered photon is termed as anti-Stokes shift [19]. The schematic diagram of the Rayleigh, Stokes and anti-Stokes Raman lines is shown in figure 2.11.

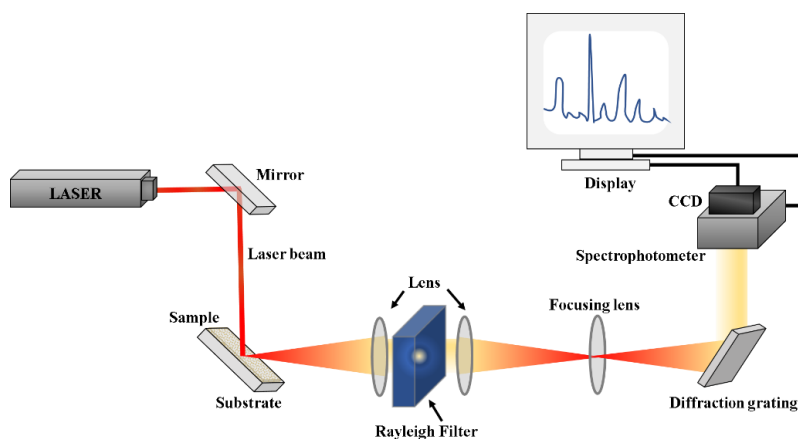


Figure 2.12: Schematic representation of the Raman instrument.

In the present thesis, room temperature Raman spectra were recorded by using the Jobin-Yvon Horiba Raman micro spectrometer attached to two air-cooled solid-state laser kits, at 532 nm, 785 nm and a He-Ne gas laser having excitation wavelength 633 nm with a power of less than 10 mW. For temperature-dependent Raman measurements, THMS600 stage from Linkam having an accuracy of 0.1 K was used.

The other major components of the Raman Spectrometers are:

1. Plasma line filter:

This filter is used to cut the plasma lines generated by gas laser due to the formation of plasma. These plasma lines are very intense and can interfere in the Raman spectra of the specimen; therefore, it needs to be cut to accomplish good Raman spectra.

2. Edge filter:

An edge filter is used to exclude the Rayleigh lines as the intensity of the elastically scattered Rayleigh lines are 106 times higher than the Raman lines and it can overshadow the Raman lines therefore it needs to be removed. The edge filter ensures that only Raman Stokes lines are transmitted. The edge filter has a very narrow width of transition which allows it to measure even the smallest Raman shifts.

3. Microscope:

The present system is equipped with three objective lenses 100x, 50x and 10x for the collection Raman scattered radiation. All these lenses are different by their working distance, numerical aperture and resolution. In the present work, a 100x objective lens is used to acquire

the room temperature Raman spectra. However, the 50x objective lens is used for the low-temperature Raman measurements, as in this case, the long working distance is required because of the height of the stage used for taking the sample to low temperature.

4.Grating:

It acts as a dispersive element and separates the scattered photons on the basis of wavelength before they enter the detector. The Raman set up is equipped with the two gratings, 600 grooves/mm and 1800 grooves/mm. The spectral range covered by the spectrograph in one shot depends on the grating and wavelength used for the excitation.

5.CCD detector:

The output of the spectrograph is detected by the charge-coupled device (CCD). It collects the scattered photons and gives an electrical signal to the computer, where the software (Labspec6.0) processes the signal by subtracting the energy of the scattered photon from the incident photon and generates the pattern of intensity versus Raman shift (cm^{-1}) with reference to the zero set energy of the incident photon.

2.3.4 Atomic Force Microscopy (AFM):

The topographical image at nanoscale for the sample surface can be recorded using atomic force microscopy instrument, which gives the information about the surface morphology and the surface roughness. The interaction between a conducting probe tip and the sample surface was first demonstrated by using atomic force microscopy in the year 1986 by Gerd Binnig *et al.* at IBM Zurich [20].

Working principle:

Basic components of an AFM system are microcantilever with a probe tip attached to a free end, laser source for detection of the feedback, a four-section photodiode and a piezoelectric sensor. Figure 2.13 shows the schematic of an AFM system.

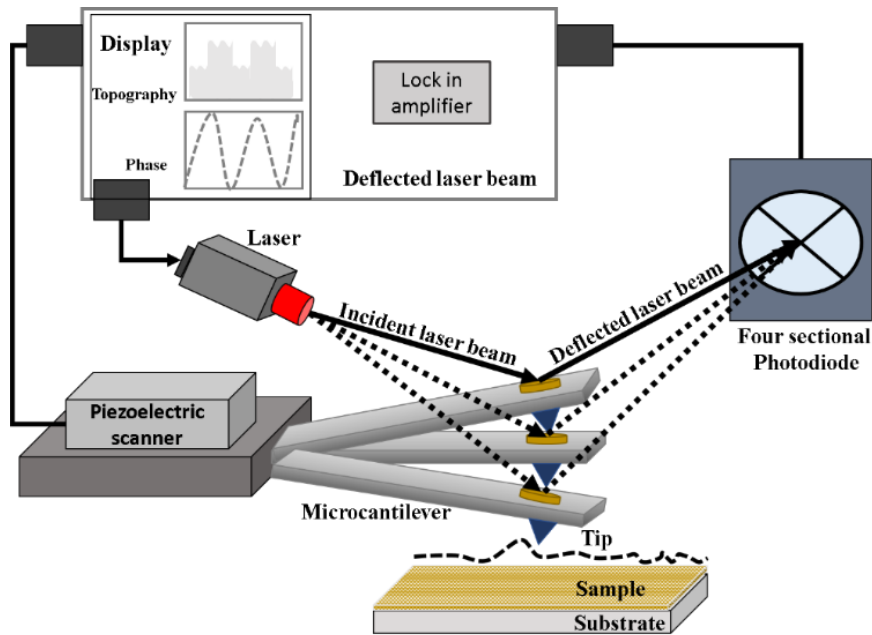


Figure 2.13: Schematic representation of an AFM setup.

A scanning tip generally made up of silicon (Si) or silicon nitride (Si_3N_4) is used for imaging the samples. The tip approaches the sample in an interatomic range (~ 0.1 nm). As the tip is moved close to the sample surface, it allows the interactions between the tip and the sample surface as a result attractive and repulsive force is experienced by the cantilever which causes to and fro motion of the cantilever. The motion of the lever is detected from a laser beam, which sends a signal to the system. Interaction between the tip and surface generates a force which can be attributed to the spring constant of the cantilever and the varied distance between the tip and the surface [21]. The force is understood with the help of Hook's law:

$$F = -K \cdot x \quad (2.2)$$

Where F is the force, K is the spring constant and x is the deflection measured in the cantilever. The deflection caused between the two can be due to electrostatic, magnetic, Vander walls kind of interactions. Displacement caused due to these deflections is measured, and a topographical image is formed. As the tip is moved on the surface, it receives signals from the laser beam that is constantly striking the cantilever which is read by a sensitive photodiode [22]. Based on the

movement of the tip, the AFM instrument can be used in three different modes:

- (i) **Contact mode:** In this mode, the tip is steadily in contact with the surface of the sample. The feedback system maintains the cantilever deflection constant through the scanning process. Surfaces like hard polymers, crystals etc. which are rigid and flat in nature are most suitable for the contact mode. In contact mode, it is easier to capture the image caused due to irregularities. Direct contact between the tip and surface of the soft material can cause the damage of the sample surface.
- (ii) **Non-contact mode:** This mode is mainly used for the soft material to prevent the undesired sample damage in contact mode. In this mode, the oscillation of the cantilever is larger than its resonance frequency.
- (iii) **Tapping mode:** Tapping mode is also known as the intermediate contact mode. The oscillation of the cantilever is near to its resonance frequency. The resolution of this mode is comparable to the contact mode.

2.3.5 X-ray Photoelectron Spectroscopy (XPS):

X-ray Photoelectron Spectroscopy is a widely used technique for the analysis of surface properties. Noble laureate Kai Siegbahn developed it in the year of 1960. This measurement setup is used for detecting the elemental constituents of the sample, the electronic state of the material and contamination present within the sample [23].

Working principle:

The samples are irradiated with the X-rays; as a result, the emitted electrons are studied on the parameters like distribution of kinetic energy. These high-end characterization setups require a very precise vacuum to not get affected by the environment easily; thus, an ultra-high vacuum is preferred while making the measurement [23].

Basic sources of XPS are soft X-rays (*i.e.* energy 100-2500 eV) is used. When the X-rays of optimum energy are irradiated on to the sample, it excites the electrons in the bound state, which lead towards emission and ionization of the electrons present in the core [24]. These photoelectrons, after getting ejected, are then collected with the help of a hemispherical analyzer. The hemispherical analyzer measures the kinetic energy of the electrons travelling inside them. Based on the Ernest Rutherford relation, which relates binding energy with photoelectrons the spectrum of ejected electron is made [25].

$$E_B = h\nu - (E_k + \Phi) \quad (2.3)$$

Where, E_B is the binding energy of the electrons, $h\nu$ is the photon energy, the kinetic energy of emitted electrons is given by E_k and Φ is the work function of the spectrometer.

2.3.6 DC resistivity measurement:

Electrical resistivity measurement is very crucial indicators for examining an important aspect of electrical properties related to the materials. Electrical resistivity is inversely proportional to the charge carrier density and carrier mobility of the material. Thus, a change in the nature of the material will have an impact on the charge carriers, which will alter the outcome of the resistivity [26].

Working principle:

Several models are present for the measurement of electrical resistance. Factors that affect the suitability of the methods depends on some discrete properties like contact resistance, the shape of the sample (*i.e.* thin film, single crystal, pellets) [27]. Methods like two probes can be used for higher resistive sample and four-probe methods for low resistive samples and single crystals as well.

Two probe measurement:

This method is known for the simplest way of measuring the resistivity. In this method, potential difference across the sample is

measured across the probes while the current is sourced across the probes [28].

The resistive value is given as:

$$\rho = \frac{V.A}{I.L} \quad (2.4)$$

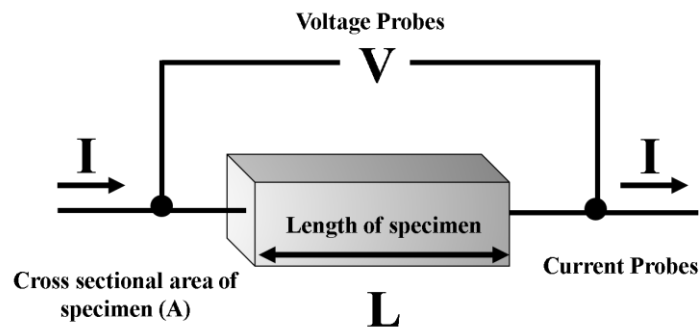


Figure 2.14: Resistivity measurement by the two-point probe.

Four probe measurement:

The disadvantage of two probe method can be overcome with the help of two more probes into the system, thus making it four-probe system. In this system, the two probes at the extreme side of the sample are used for sourcing current, whereas the inner (middle) two probe are utilized for measuring the voltage across it. The probes are equidistant across the length of the sample and to each other as well. The advantage of this method over two probes is that it eliminates the contact resistance. This is possible due to the use of different probes for sourcing and other probes for measuring this not affecting the contribution from the contacts [29].

The resistive value is given as:

$$\rho = \frac{V_D.A}{I.D} \quad (2.5)$$

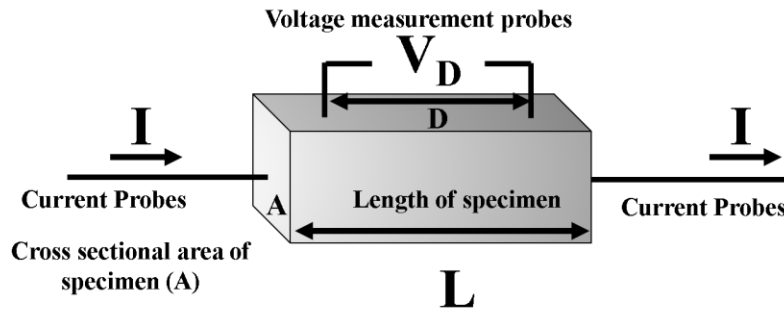


Figure 2.15: Resistivity measurement by the four-point probe.

In the present study, the four-probe method was used to measure the temperature-dependent resistivity of thin films. The average size of the thin films deposited on the solid substrate was 2.5x5 mm. To make the connections, four conductive copper wires are affixed (with silver paint) on the surface of the thin films. The temperature-dependent resistivity measurements were performed using the Keithley source meter (model: 2612 A) in the combination of the Janis made closed-cycle refrigerator (CCR) and temperature controller (Lakeshore 332).

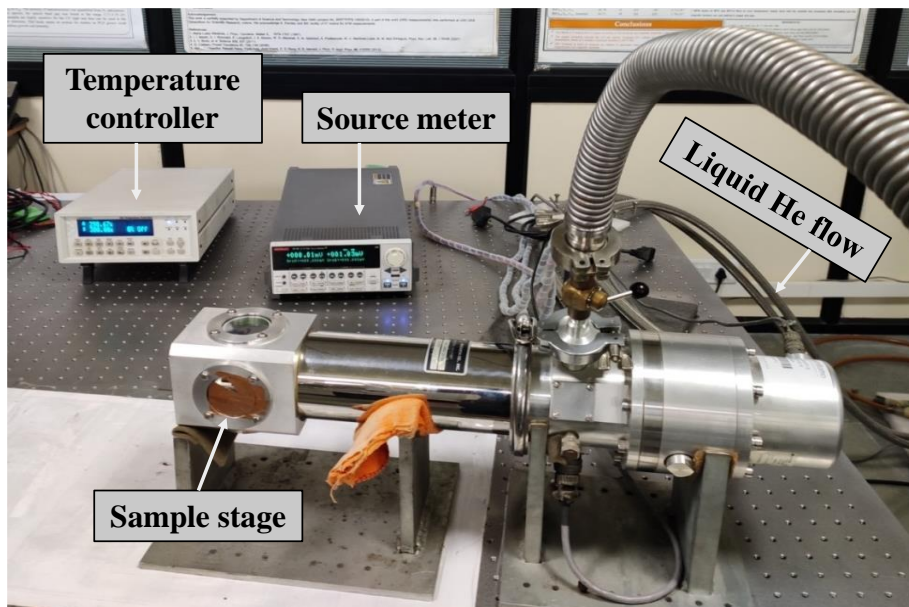


Figure 2.16: Experimental setup for the temperature-dependent resistivity measurement.

References:

- [1] T. Venkatesan, Pulsed laser deposition - Invention or discovery?, *J. Phys. D. Appl. Phys.* 47 (2014).
- [2] X. Wang, Y. Xin, H. Lee, P.A. Stampe, R.J. Kennedy, Z. Zhou, J.P. Zheng, Ca_2RuO_4 thin film growth by pulsed laser deposition, *Mater. Res. Soc. Symp. - Proc.* 819 (2004) 183–187.
- [3] D. Kaur, J. Jesudasan, P. Raychaudhuri, Pulsed laser deposition of NdNiO_3 thin films, *Solid State Commun.* 136 (2005) 369–374.
- [4] F.L. Forgerini, R. Marchiori, A brief review of mathematical models of thin film growth and surfaces. A possible route to avoid defects in stents, *Biomater.* 4 (2014) e28871.
- [5] S. Rossmagel, Sputtering and Sputter Deposition, *Handb. Thin Film Depos. Process. Tech.* (2001) 319–348.
- [6] J.H.V.D.M. F.C. Frank, One-dimensional dislocation. II. Misfitting monolayers and oriented overgrowth, *Proc. R. Soc. London A.* (1949) 216–25.
- [7] A. Baskaran, P. Smereka, Mechanisms of Stranski-Krastanov growth, *J. Appl. Phys.* 111 (2012).
- [8] J. Song, Q. Li, X. Wang, J. Li, S. Zhang, J. Kjems, F. Besenbacher, M. Dong, Evidence of Stranski-Krastanov growth at the initial stage of atmospheric water condensation, *Nat. Commun.* 5 (2014) 1–8.
- [9] B.D. Cullity, S.R. Stock, *Elements of X-ray diffraction*, 3rd edition, Prentice Hall. (2001).
- [10] C. Hammond, *The Basics of Crystallography and Diffraction* (2nd edn), Meas. Sci. Technol. (2002).
- [11] P.F. Fewster, X-ray analysis of thin films and multilayers,

- Reports Prog. Phys. 59 (1996) 1339–1407.
- [12] S.K. Sinha, E.B. Sirota, S. Garoff, H.B. Stanley, X-ray and neutron scattering from rough surfaces, Phys. Rev. B. 38 (1988)
- [13] A. Gibaud, S. Hazra, X-ray reflectivity and diffuse scattering, Curr. Sci. 78 (2000) 1467–1477.
- [14] L.G. Parratt, Surface studies of solids by total reflection of x-rays, Phys. Rev. 95 (1954) 359–369.
- [15] H. Kiessig, Untersuchungen zur Total reflexion, Ann. Phys. 402 (1931) 715–768.
- [16] G. Feng, L. Wu, J. Letey, Evaluating aeration criteria by simultaneous measurement of oxygen diffusion rate and soil-water regime, Soil Sci. 167 (2002) 495–503.
- [17] C. V. Raman, K.S. Krishnan, A new type of secondary radiation, Nature. 121 (1928) 501–502.
- [18] B. Schrader, Infrared and Raman Spectroscopy - Methods and applications, VCH Publ. 100 (1995) 1268.
- [19] G.D. Ewen Smith, Mordern Raman Spectroscopy :Apractical approach, 2019.
- [20] C.F.Q. G. Binnig, Atomic Force Microscope, Phys. Rev. Lett. 56 (1986) 930–934.
- [21] G. Friedbacher, Atomic Force Microscopy (AFM), 2011.
- [22] R.W. Phillips, Atomic force microscopy for thin film analysis, Surf. Coatings Technol. 68–69 (1994) 770–775.
- [23] S. Oswald, X-Ray Photoelectron Spectroscopy in Analysis of Surfaces, 2013.
- [24] J.F. Watts, X-Ray photoelectron spectroscopy, Elsevier Sci. Ltd. 45 (1994) 653–671.

- [25] W.L.J. JACK M. HOLLANDER, X-Ray photoelectron spectroscopy, *X-Ray Photoelectron Spectrosc.* 17 (1970) 193–200.
- [26] S. Choudhary, R. Narula, S. Gangopadhyay, Thin Cu film resistivity using four probe techniques: Effect of film thickness and geometrical shapes, *AIP Conf. Proc.* 1953 (2018).
- [27] A.A. Ramadan, R.D. Gould, A. Ashour, On the Van der Pauw method of resistivity measurements, *Thin Solid Films.* 239 (1994) 272–275. [https://doi.org/10.1016/0040-6090\(94\)90863-X](https://doi.org/10.1016/0040-6090(94)90863-X).
- [28] M. Yamashita, T. Nishii, H. Mizutani, Resistivity measurement by dual-configuration four-probe method, *Japanese J. Appl. Physics, Part 1 Regul. Pap. Short Notes Rev. Pap.* 42 (2003) 695–699.s
- [29] F.M. Smits, Measurement of Sheet Resistivities with the Four-Point Probe, *Bell Syst. Tech. J.* 37 (1958) 711–718.

Chapter 3

Structure influenced rapid hydrogenation in VO₂ thin films

In this chapter, the study on the role of the crystal structure to accommodate the hydrogen in VO₂ thin film is presented. For a comparative study, five thin films were deposited on the single-crystal sapphire substrate in identical deposition conditions. The grown films are pure and crystallographically oriented towards *b* axis of the monoclinic structure. The material, VO₂ generally shows the structural phase transformation around 341 K simultaneous to a metal-insulator transition. In order to study the effects of structure, the hydrogenation *via* metal-acid contact method was tested at different temperatures above and below this structural transition. A procedure for rapid and sustainable hydrogenation has been developed and reported here. The results presented in this chapter are published in the peer-reviewed journal*.

**Mulchandani et. al., Applied surface science, 541, (2021) 148369. (doi.org/10.1016/j.apsusc.2020.148369).*

3.1 Introduction

Structural phase transition near room-temperature makes VO₂ potentially valuable for applications in optical, electrical and thermal switches [1], smart windows [2], ultrafast optical switching devices, memory devices [3] *etc.* Several efforts have been made to modulate the phase transition such as strain engineering [4,5], varying oxygen vacancy [6] and chemical doping of higher valence elements such as Mo [7], W [8], and atomic hydrogen doping [9–11] *etc.* Unlike other doping, the hydrogen doping in VO₂ is reversible in nature. VO₂ can release hydrogen without destroying its lattice structure. The nature of reversible phase modulation opens the potential application in proton-based electronic devices [12]. There are many reports of hydrogenation which are based on the conventional annealing method using either noble metal catalyst or high pressure and temperature [13,14]. This conventional method is not that much sustainable due to the requirement of the permanent sputtered metal catalyst and extreme conditions of the temperature and pressure; also, it is a very time-consuming process. Recently, Chen *et al.* found a very simple approach of non-catalytic hydrogenation [15]. They reported on the hydrogenation of magnetron sputtered VO₂ thin films in the acidic solution at ambient temperature for 24 h. However, this method is catalyst-free but still, time-consuming and takes hours to complete the hydrogenation.

In this study, we found the catalyst-free as well as a time-effective method of the hydrogenation of pulsed laser deposited crystallographically oriented VO₂ thin films. We performed the incorporation of the hydrogen with a simple design of the electrode-like structure of Al on the edges of VO₂ thin films via metal-acid contact method. One important parameter associated with the selection of the metal is *workfunction*. Here we require the low-work function metal on the surface of the VO₂. Since the work function of Al (4.11eV) is less as compared to other metals such as Ag(4.44eV), Cu(4.71eV), Au(5.13eV), Pt(5.79eV) [15], to achieve the diffusion of the hydrogen, we have chosen the Al metal for our study. The considerable work

function difference between Al and VO₂ will induce the flow of electron from metal to VO₂. Further, to balance the electronic charge, protons (H⁺ ions) of an acid solution will attract towards VO₂, this will lead the hydrogen doping into VO₂ [15]. Hydrogenation of VO₂ thin films carried out in monoclinic (below T_{MI}) as well as in the rutile phase (above T_{MI}) of the VO₂. The novelty of this work is the incorporation of hydrogen at different temperatures in order to see the effect of structure on hydrogenation because the diffusion rate of hydrogen is dependent on the structure of VO₂. As a result, we found hydrogenation of only for 30 seconds *via* metal-acid treatment at elevated temperature.

3.2 Experimental

3.2.1 Bulk target and VO₂ thin films synthesis

A bulk target of 20 mm diameter was synthesized by hard pressing V₂O₃ powder using a hydraulic press and was sintered at 1000°C in Ar atmosphere for 24 hours. The prepared bulk target was used as target material for thin films synthesis using PLD method. VO₂ thin films (~40 nm) were deposited on single crystal *c*-cut sapphire (Al₂O₃) substrates using pulsed laser deposition method. KrF excimer Laser (Compex Pro 102 F, λ=248 nm) was used for ablation of the target material with an energy fluence of ~2.5 mJ/cm². The target to substrate distance and temperature of the substrate was kept fixed at 4 cm and 650 °C, respectively. Throughout the deposition of thin films, the oxygen partial pressure was maintained at 4 Pa, and the repetition rate was kept at 5 Hz. For a comparative study of hydrogenation at different temperatures (Structures), five thin films were grown simultaneously under identical conditions. Soon after the deposition, the films were cooled down to room temperature.

3.2.2 Hydrogenation procedure

For the hydrogenation process, metal-acid treatment of 4 thin films was carried out by 2 wt% H_2SO_4 for 30 sec by utilizing the detachable electrode-like structure of Al metal (Figure 3.1). The detailed procedure of hydrogenation *via* metal-acid treatment is described in the chapter-2 of the thesis.

For comparative study, the four films were hydrogenated at different temperatures, *i.e.* Room temperature, 313K, 333K, 343K, and accordingly, the samples were coded as VO_2 -300, VO_2 -313, VO_2 -333, VO_2 -343, respectively. In order to see the effect of hydrogenation in VO_2 , one film was kept untreated and coded as VO_2 . For the dehydrogenation process, the thin film was heated at 343 K for 2 h in the open air.

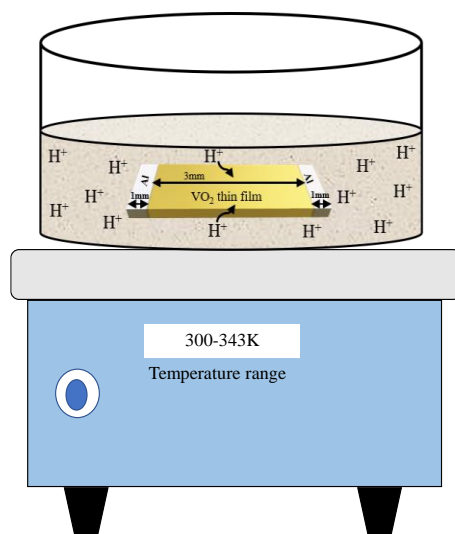


Figure 3.1: Schematic diagram of the hydrogenation process.

Rigaku Smart Lab diffractometer was used for X-ray diffraction (XRD) and X-ray reflectivity (XRR) measurements to determine the crystallinity and thickness of prepared thin films, respectively. For the observation of surface morphology and roughness, the atomic force microscope (AFM) (Park Systems, NX10) was used. To investigate electrical transport behavior, the temperature-dependent resistivity measurements were performed by a four-probe method with silver

contacts using home-made apparatus affixed with a temperature sensor just beneath the sample holder with a heater and one air-cooling unit. The heating rate for the measurement was 0.5K/min. Keithley source meter (Model:2612A) was used for the measurement of resistivity, in the temperature range of (303-363K). X-ray photoelectron spectra (XPS) is recorded by beamline BL-14 of the Indus-2 synchrotron source. Measurement was performed in an ultra-high vacuum with the monochromatic X-ray beam of 4357 eV energy. To examine the structural change with temperature and hydrogen doping, temperature-dependent Raman spectra were collected with Horiba LabRam HR Evolution spectrometer. The excitation source, He-Ne Laser (632.8 nm) with less than 1 mW power was used to avoid the heating effects.

3.3 Results and discussion

3.3.1 Structural Analysis

X-ray Diffraction

Figure 3.2(a) shows the full-scale XRD patterns of the pristine VO₂ thin film and *c*-cut sapphire substrate. The XRD pattern is free of any impurity peak and shows (020) and (040) reflections corresponding to the monoclinic phase of VO₂. Figure 3.2(b) shows the magnified view of the (020) peak of VO₂. As hydrogen incorporation takes place, systematic and significant broadening in the (020) peak is observed in XRD patterns of VO₂ films (figure 3.2(b)) which are described in the latter part of the text. A minor peak shifting takes place towards the lower angle, indicating an expansion of unit cell due to the hydrogen doping. The bonding of the interstitial H atom with oxygen atoms drives the lattice slightly towards the rutile phase with expansion in the unit cell [12,13].

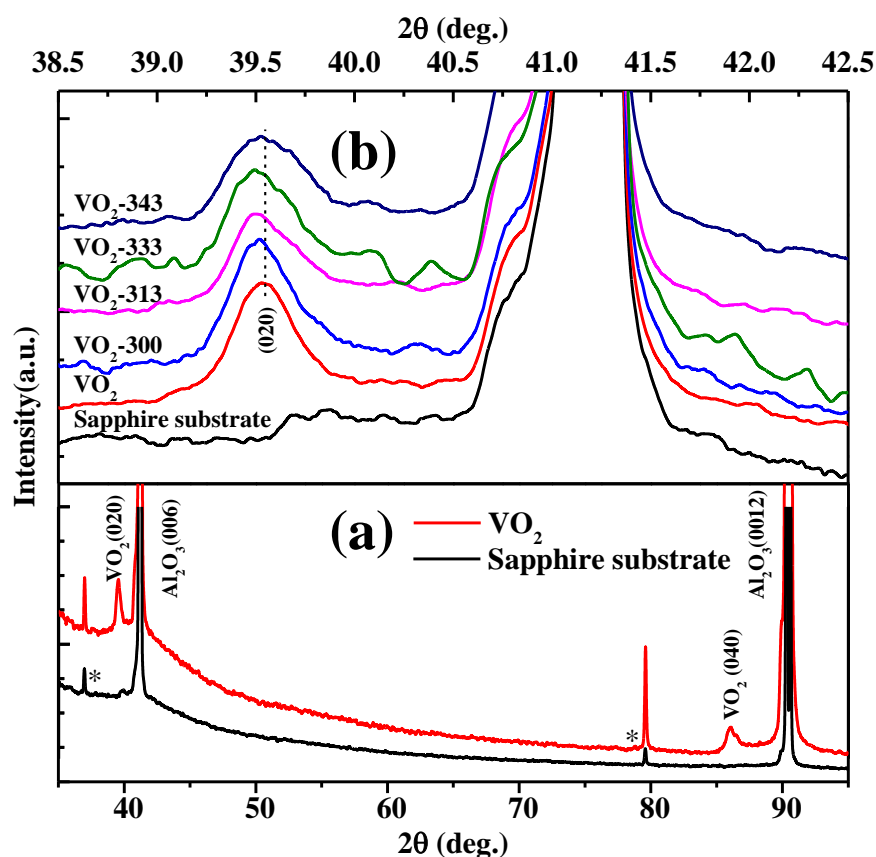


Figure 3.2: (a) Full-scale XRD of pristine VO₂ film and sapphire substrate. XRD peaks other than (00*l*) reflections from a substrate are marked by *. (b) XRD patterns of pristine and hydrogenated VO₂ thin films grown on the Al₂O₃ substrate.

Raman Spectroscopy

Temperature-dependent Raman spectroscopy was employed to study the phonon vibrations and through that track the possible structural changes in the pristine (VO₂) and hydrogenated (VO₂-300 and VO₂-343) VO₂ thin films. These three films are chosen for the Raman study in order to compare the effects of hydrogenation across the transition. The Raman spectra of all the films were obtained under identical conditions. In the monoclinic phase, 18 modes are predicted to be Raman active by group theory, whereas the rutile phase shows broadband luminescence or featureless spectra [16,17]. At room temperature, there are total 10 Raman active modes observed at 149, 194, 224, 266, 310, 339, 390, 441, 498, 615 cm⁻¹, all these modes indicate the monoclinic (of M₁ type)

phase of VO₂. The Raman modes at 418, 432, 450, 579, 752 cm⁻¹ appear due to the contribution from the sapphire substrate [18]. The low-frequency modes depict V-V pairing and the vibrations due to its tilting, whereas high-frequency mode at 615 cm⁻¹ represents V-O vibrations [19].

Figure 3.3 (a-c) shows the temperature-dependent Raman spectra of VO₂, VO₂-300 and VO₂-343 thin films. Inset figure 3.3 (c) shows the temperature-dependent change in the most prominent low-frequency mode at 194 cm⁻¹ in VO₂, VO₂-300, and VO₂-343 films. A softening as well as broadening in the low-frequency modes were observed for the pristine thin film with the increasing temperature (Inset figure 3.3(c)). This softening and broadening of modes take place due to the structural transformation from monoclinic to rutile phase [20]. VO₂-300 film shows less softening of the modes as compared to those of pristine film. On the other hand, VO₂-343 film shows initial softening of modes as temperature increased from 300 K to 310 K, followed by which a negligible change has been observed above this temperature. Zhao *et al.* claimed that the absence of the temperature-dependent shift in low-frequency modes shows the presence of coexisting monoclinic and rutile phases of VO₂. This further infers that the present process of hydrogenation of films at elevated temperatures leads to finally a coexisted monoclinic and rutile phases at ambient temperature [13].

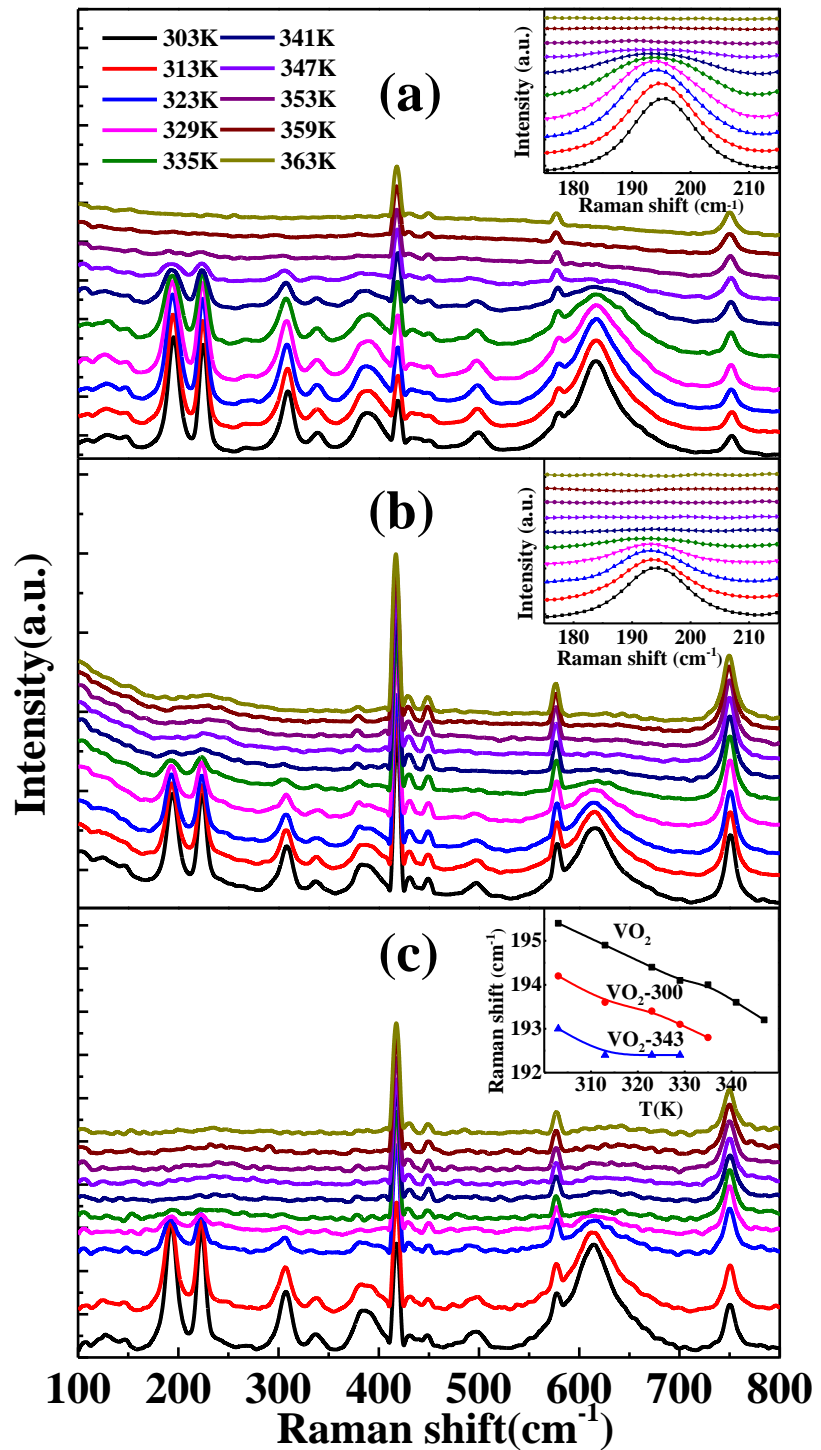


Figure 3.3: (a-c) Temperature-dependent Raman spectra of VO₂, VO₂-300 and VO₂-343 films.

Across the temperature range of the study, Raman modes of both the hydrogenated films show lower intensities in comparison to that of the pristine film. Low-intensity signal of Raman mode with hydrogen doping also further confirms the structural transformation from

monoclinic to rutile phase [20]. In the low-temperature range for both the hydrogenated films, featureless Raman spectra with vanishing intensities were observed because of its mixed-phase condition. The rutile phase shows featureless or broad spectrum of Raman and hence the mix of any rutile phase in the material can be indirectly detected by observing the Raman spectra.

3.3.2 Surface Analysis

To determine the thickness of the films, X-ray reflectivity (XRR) measurements were performed. Figure 3.4 shows the XRR results along with the Parratt fitting. The thickness of the films is calculated based on this fitting and found to be around 40 nm. It can be clearly observed from the analysis of XRR patterns that the hydrogenation does not affect the thickness of any film, and the thickness remains the same even after two to three cycles of hydrogenation and dehydrogenation process.

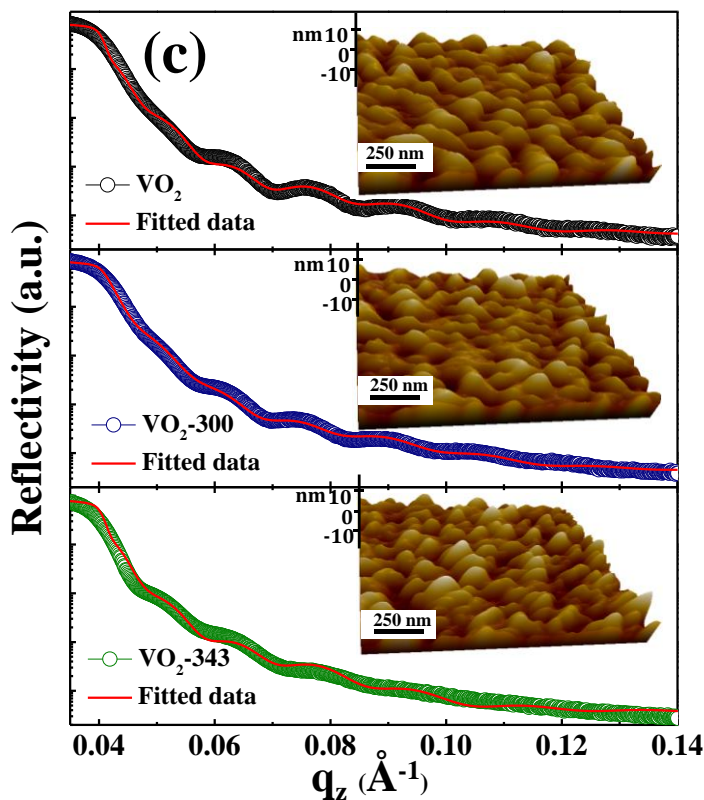


Figure 3.4: XRR fitting and AFM images of pristine and hydrogenated VO₂ thin films.

Figure 3.4 shows the AFM images of the films. All the films show similar and uniform morphology. Based on AFM images, root mean square (RMS) roughness of the films was observed to be 5.6 nm, 3.1 nm and 2.6 nm, respectively for VO₂, VO₂-300 and VO₂-343 films. The roughness is found to be reduced with increased hydrogen incorporation. Moreover, the grain size distribution changes with hydrogenation in thin films, which also got reflected by broadened XRD peaks, as explained above.

3.3.3 Chemical composition

In order to identify the chemical states of pristine and hydrogenated thin films of VO₂, XPS is used. For analysis, Shirley background subtraction is imposed, and deconvolution of the peak into it constitutes is done. For the calibration of different elements, carbon C1s peak is assumed to have a binding energy of 284.6 eV. Figure 3.5 shows the peak position of O1s, V2p_{1/2} and V2p_{3/2} core level for VO₂ and VO₂-343 films. The reference binding energy corresponding to H-O, V-O, V³⁺, V⁴⁺, and V⁵⁺ is 531.9 eV, 530.1 eV, 515.5 eV, 516.0 eV and 517.1 eV, respectively [14,21]. The deconvolution peaks of O1s peak shows two peaks; one is corresponding to H-O bond and another one due to the V-O bond. It is important to note that the peak corresponding to H-O is present in both hydrogenated as well as in the pristine film. In pristine films, H-O peak is present due to surface contamination. With the incorporation of hydrogen, the percentage of peak area is increasing for H-O bond while on the other hand, this area is decreasing for V-O bond. This indicates that the hydrogen is chemically bonded with the oxygen atom. V⁴⁺ is the most prominent state for VO₂ thin films, and V⁵⁺ state exists due to the surface oxidation in the air. The bonding of H atom with oxygen affects the valence state of vanadium in the hydrogenated film; as a result of a slight change in V⁴⁺ state to V³⁺ state. Deconvolution of peak V2p_{3/2} reveals that the V³⁺ state appears only after hydrogenation in VO₂-343 thin film.

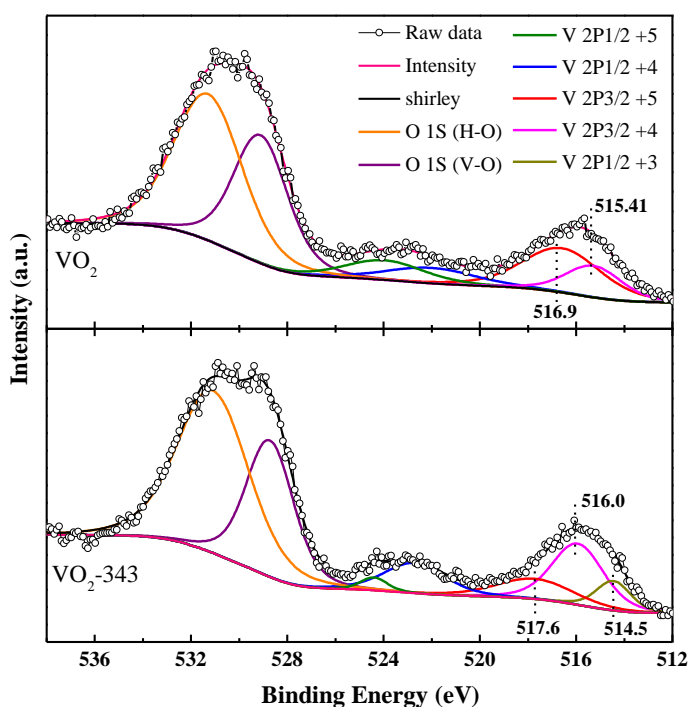


Figure 3.5: V2p and O1s core level XPS spectra of VO₂ and VO₂-343 films, confirming the V³⁺ state after hydrogenation.

3.3.4 Electronic properties

Figure 3.6 shows the temperature-dependent electrical resistivity of VO₂ thin films. Pristine VO₂ film shows three orders of change in the resistivity at the transition temperature (T_{MI}) of 332 K. The T_{MI} for the film is generally lower than that of bulk VO₂ (340K) due to the effect of strain [5]. The resistivity curves of VO₂, VO₂-300, and VO₂-313K films show similar values across the transition, whereas the resistivity curves of VO₂-333 and VO₂-343 show dramatically different values below T_{MI} . The latter two films show about two orders of decrease in the room-temperature resistivity as compared to that of the pristine film. Notably, the hydrogenation does not affect the T_{MI} , as well as the resistivity values, and the resistivity remains the same above T_{MI} . Thus, the films fall into two categories, *a*) the pristine film and the films hydrogenated in monoclinic phase, and *b*) the films hydrogenated in rutile phase; where the change of structure is acquired by variation in the temperature at the time of hydrogenation. These resistivity results clearly indicate that the effect of hydrogenation on the resistivity is mediated by the

structure of the films and not because of any thermal effect at the time of hydrogenation. Further, once this hydrogenation takes place in the rutile phase, the film tends to partially retain the rutile phase even after cooling down the film to ambient temperature, as is also observed by XRD and Raman spectra. Because of this tendency of VO₂-333 and VO₂-343 films of partially retaining the rutile structure below T_{MI}, the resistivity of these two films remains low as compared to that of the other set of films. This feature further validates the partially acquired rutile phase in VO₂-333 and VO₂-343 films.

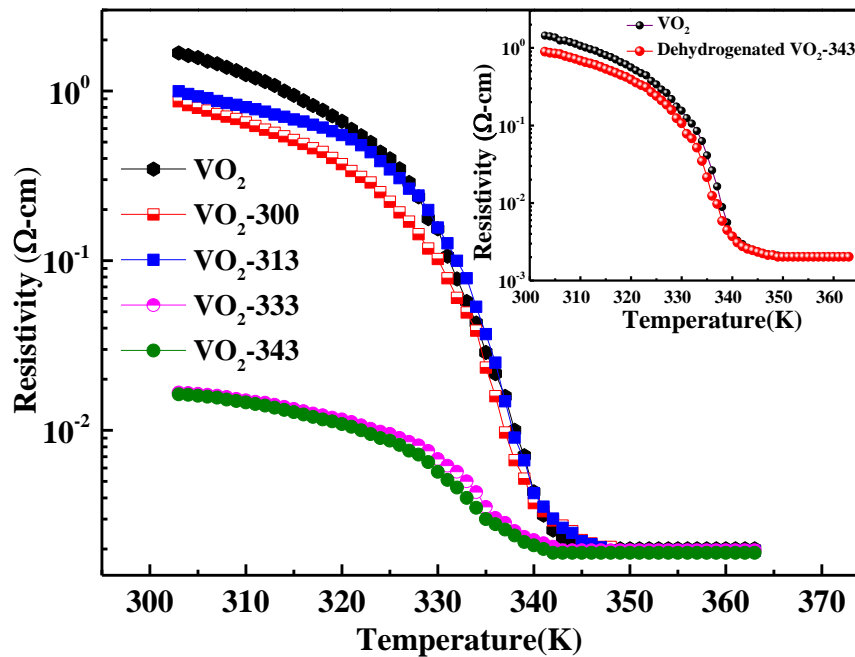


Figure 3.6: Temperature-dependent resistivity curves of VO₂ films, inset shows temperature versus resistivity curve of VO₂-343 after dehydrogenation process.

To further test the reversibility and sustainability, the dehydrogenated VO₂-343 was characterized for temperature-dependent resistivity again. As shown in inset figure 3.6, the film almost retains the original values of the resistivity, indicating no significant damage to the film as well as the reversible structure and electronic state.

Additionally, to test the stability of the hydrogenation, the resistivity of all the films was measured again from time to time for two

days. A steady change in the value of resistivity back to the original was observed after two days for VO₂-300 and VO₂-313 films; however, VO₂-333 and VO₂-343 films continued to show nearly same values of the resistivity as earlier *i.e.*, at the time of the hydrogenation. This study indicates that a higher stability of the modified process of the hydrogenation in the rutile phase as compared to that in the monoclinic phase of VO₂ thin films.

3.4 Summary

We have deposited five crystallographically oriented and crystalline VO₂ thin films with (020) orientation on a sapphire substrate using the PLD method. The effects of hydrogen incorporation on the properties of VO₂ films were studied. These results indicate that the VO₂ films, when hydrogenated at elevated temperatures, show dramatic variation in the resistivity even if they are processed only for 30 seconds. These films also tend to retain the rutile structure even after cooling down to the room temperature, which can be a way to stabilize the rutile structure in the films at ambient conditions. Additionally, the study also indicates that the VO₂ films show enhanced stability of hydrogenation and increased effects on the resistivity state when hydrogenated at elevated temperatures with rutile structure. Here, a method of hydrogenation by simple metal-acid contact at *higher than room temperature* is presented, which is much rapid, sustainable, noncatalytic, as well as reversible.

References:

- [1] Z. Yang, C. Ko, S. Ramanathan, Oxide Electronics Utilizing Ultrafast Metal-Insulator Transitions, *Annu. Rev. Mater. Res.*, 41, (2011), 337-367. (DOI:10.1146/annurev-matsci-062910-100347).
- [2] F. Xu, X. Cao, H. Luo, P. Jin, Recent advances in VO₂-based thermochromic composites for smart windows, *J. Mater. Chem. C*, 6, (2018), 1903-1919. (DOI:10.1039/c7tc05768g).
- [3] N. Vardi, E. Anouchi, T. Yamin, S. Middey, M. Kareev, J. Chakhalian, Y. Dubi, A. Sharoni, Ramp-Reversal Memory and Phase-Boundary Scarring in Transition Metal Oxides, *Adv. Mater.*, 29, (2017), 1605029. (DOI:10.1002/adma.201605029).
- [4] J. Jian, X. Wang, L. Li, M. Fan, W. Zhang, J. Huang, Z. Qi, H. Wang, Continuous Tuning of Phase Transition Temperature in VO₂ Thin Films on c-Cut Sapphire Substrates via Strain Variation, *ACS Appl. Mater. Interfaces.*, 9, (2017), 5319-5327. (DOI:10.1021/acsami.6b13217).
- [5] L.L. Fan, S. Chen, Z.L. Luo, Q.H. Liu, Y.F. Wu, L. Song, D.X. Ji, P. Wang, W.S. Chu, C. Gao, C.W. Zou, Z.Y. Wu, Strain Dynamics of Ultrathin VO₂ Film Grown on TiO₂ (001) and the Associated Phase Transition Modulation, *Nano Lett.*, 14 (2014), 4036-4043. (DOI:10.1021/nl501480f).
- [6] L.L. Fan, S. Chen, Y.F. Wu, F.H. Chen, W.S. Chu, X. Chen, C.W. Zou, Z.Y. Wu, Growth and phase transition characteristics of pure M-phase VO₂ epitaxial film prepared by oxide molecular beam epitaxy, *Appl. Phys. Lett.*, 103 (2013), 131914. (DOI:10.1063/1.4823511).
- [7] L.Q. Mai, B. Hu, T. Hu, W. Chen, E.D. Gu, Electrical property of mo-doped VO₂ nanowire array film by melting-quenching sol-gel method, *J. Phys. Chem. B.*, 110, (2006), 19083–19086. (DOI:10.1021/jp0642701).

- [8] K. Shibuya, M. Kawasaki, Y. Tokura, Metal-insulator transition in epitaxial $V_{1-x}W_xO_2$ ($0 \leq x \leq 0.33$) thin films, *Applied Physics Letters*, 96, (2010), 022102. (DOI:10.1063/1.3291053).
- [9] J. Lin, H. Ji, M.W. Swift, W.J. Hardy, Z. Peng, X. Fan, A.H. Nevidomskyy, J.M. Tour, D. Natelson, Hydrogen diffusion and stabilization in single-crystal VO_2 Micro/Nanobeams by direct atomic hydrogenation, *Nano Lett.*, 14, (2014), 5445–5451. (DOI:10.1021/nl5030694).
- [10] Y. Filinchuk, N.A. Tumanov, V. Ban, H. Ji, J. Wei, M.W. Swift, A.H. Nevidomskyy, D. Natelson, In situ diffraction study of catalytic hydrogenation of VO_2 : Stable phases and origins of metallicity, *J. Am. Chem. Soc.*, 136, (2014), 8100–8109. (DOI:10.1021/ja503360y).
- [11] J. Wei, H. Ji, W. Guo, A.H. Nevidomskyy, D. Natelson, Hydrogen stabilization of metallic vanadium dioxide in single-crystal nanobeams, *Nat. Nanotechnol.*, 7, (2012), 357–362. (DOI:10.1038/nnano.2012.70).
- [12] H. Yoon, M. Choi, T.W. Lim, H. Kwon, K. Ihm, J.K. Kim, S.Y. Choi, J. Son, Reversible phase modulation and hydrogen storage in multivalent VO_2 epitaxial thin films, *Nat. Mater.*, 15, (2016), 1113–1119. (DOI:10.1038/nmat4692).
- [13] Y. Zhao, G. Karaoglan-Bebek, X. Pan, M. Holtz, A.A. Bernussi, Z. Fan, Hydrogen-doping stabilized metallic VO_2 (R) thin films and their application to suppress Fabry-Perot resonances in the terahertz regime, *Appl. Phys. Lett.*, 104, (2014), 241901. (DOI:10.1063/1.4884077).
- [14] S. Chen, Z. Wang, L. Fan, Y. Chen, H. Ren, H. Ji, D. Natelson, Y. Huang, J. Jiang, C. Zou, Sequential insulator-metal-insulator phase transitions of VO_2 triggered by hydrogen doping, *Phys. Rev. B.*, 96, (2017), 125130. (DOI:10.1103/PhysRevB.96.125130).

- [15] Y. Chen, Z. Wang, S. Chen, H. Ren, L. Wang, G. Zhang, Y. Lu, J. Jiang, C. Zou, Y. Luo, Non-catalytic hydrogenation of VO₂ in acid solution, *Nat. Commun.*, 9, (2018), 1-9. (DOI:10.1038/s41467-018-03292-y).
- [16] P. Schilbe, Raman scattering in VO₂, *Phys. B Condens. Matter.*, 316–317, (2002), 600–602. (DOI:10.1016/S0921-4526(02)00584-7).
- [17] R. Srivastava, L.L. Chase, Raman spectrum of semiconducting and metallic VO₂, *Phys. Rev. Lett.*, 27, (1971), 727–730. (DOI:10.1103/PhysRevLett.27.727).
- [18] J.R. Skuza, D.W. Scott, A.K. Pradhan, Sapphire substrate-induced effects in VO₂ thin films grown by oxygen plasma-assisted pulsed laser deposition, *J. Appl. Phys.*, 118, (2015), 195303. (DOI:10.1063/1.4935814).
- [19] C. Marini, E. Arcangeletti, D. Di Castro, L. Baldassare, A. Perucchi, S. Lupi, L. Malavasi, L. Boeri, E. Pomjakushina, K. Conder, P. Postorino, Optical properties of V_{1-x}Cr_xO₂ compounds under high pressure, *Phys. Rev. B*, 77, (2008), 235111. (DOI:10.1103/PhysRevB.77.235111).
- [20] Y. Huang, D. Zhang, Y. Liu, J. Jin, Y. Yang, T. Chen, H. Guan, P. Fan, W. Lv, Phase transition analysis of thermochromic VO₂ thin films by temperature-dependent Raman scattering and ellipsometry, *Appl. Surf. Sci.*, 456, (2018), 545–551. (DOI:10.1016/j.apsusc.2018.06.125).
- [21] D. Lee, H. Kim, J.W. Kim, I.J. Lee, Y. Kim, H.J. Yun, J. Lee, S. Park, Hydrogen incorporation induced the octahedral symmetry variation in VO₂ films, *Appl. Surf. Sci.*, 396, (2017), 36–40. (DOI:10.1016/j.apsusc.2016.11.047).

Chapter 4

Electric field induced rapid hydrogenation in VO₂ thin films

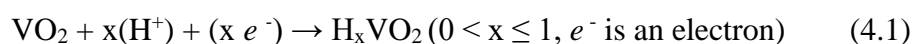
In this chapter, rapid hydrogenation of VO₂ thin films using very mild electric fields is presented. The limitation of the high temperature for the rapid hydrogenation, as discussed in the chapter-3, is overcome by this work. For the hydrogenation process, we used mild electric fields in ionic solution at *room temperature* using a self-assembled setup. The method is much rapid, sustainable, noncatalytic, as well as reversible. The high stability and extraordinary reversibility of the films show a great potential for material applications in proton-based electronic devices. The results presented in this chapter are published in the peer-reviewed journal[#].

[#]Mulchandani *et. al.*, *Materials Letters*, **295** (2021) 129786.
(doi.org/10.1016/j.matlet.2021.129786)

4.1 Introduction

Hydrogenation of VO₂ thin films has gained a lot of attention for over a decade because of its dynamic nature in tuning the MIT as well as for the application of VO₂ films in proton based electronic devices [1]. It has been reported that the incorporation of hydrogen into the VO₂ lattice slowly drives the cells towards a more symmetric structure hence stabilizing the metallic phase at room temperature [2]. Hydrogenation *via* a conventional method, *i.e.* annealing of the films in a hydrogen atmosphere, either requires permanent sputtered islands of metals or high-temperature/pressure condition [1,3]. However, the drawbacks of this method are the constraint of high-temperature/pressure treatment and sputtering of the permanent metal catalyst. For practical applicability, a much more rapid and reversible method of thin-film hydrogenation is required at room temperature. In our previous study (chapter-3) we have reported rapid hydrogenation in VO₂ film using metal-acid contacts method and studied the dependence of the hydrogenation process on the structure of VO₂. The hydrogenation was found to be faster in rutile phase [4]. Despite of uncovering quite a commodious method of hydrogenation, our goal was to further accomplish the same at room temperature.

In this chapter, we have presented the catalyst-free hydrogenation of VO₂ thin films by applying a small amount of electric field to the films for a very short period of time ($\sim 30s$) in an ionic solution at *room temperature*, which was not yet demonstrated and tested method for hydrogenation of VO₂ films. The applied electric field causes the attraction of H⁺ ions from the ionic solution towards the negatively charged electrode (the film). The electrode-like structures of Al on the edges of the VO₂ thin film facilitate surface diffusion as reported in our previous work [4] and drag the H⁺ ions into the lattice. The hydrogenation process can be described by the following chemical equation [5]



Hence, the incorporated hydrogen strives to stabilize the rutile phase at the room temperature and modulate the phase transition. Moreover, the high stability and extraordinary reversibility of the films show great potential for material applications such as proton based electronic devices.

4.2 Experimental

4.2.1 Bulk and VO₂ thin films synthesis

VO₂ thin films (~40 nm) were deposited on single crystal *c*-cut sapphire (Al₂O₃) substrates using pulsed laser deposition method. The bulk target pellet (20 mm) was prepared by hard-pressing V₂O₃ powder in a hydraulic press and was sintered at 1000°C in Ar atmosphere for 24 h. The KrF excimer laser (Compex Pro 102 F, $\lambda=248$ nm) was used for ablation of the target material with an energy fluence of ~2.5 mJ/cm² and pulse rate at 5 Hz. The target to substrate distance was maintained at 4 cm, and the temperature of the substrate was kept at 650°C. The oxygen partial pressure in the deposition chamber was maintained at 4 Pa throughout the deposition of thin films. For a comparative study of hydrogenation at different voltages, five thin films were grown simultaneously under identical conditions.

4.2.2 Hydrogenation Procedure

For the hydrogenation procedure, a self-assembled setup was used with two fixed negative and positive electrodes, as shown in figure 4.1. A Keithley-made source meter (model: 2612 A) was used to apply different voltages. Firstly, detachable electrode-like aluminum contacts were made on the edges of the films. Secondly, the prepared films were attached to the negative-electrode, and on a positive-electrode, a conductive copper plate of 0.1mm thickness was affixed. For hydrogenation procedure, four films were subjected to the different voltages (*i.e.* 0mV, 0.001mV, 0.1mV, and 0.5mV) in an ionic solution (2 wt% H₂SO₄) at room temperature only for 30 seconds and the films were coded as 0-VO₂, 0.001-VO₂, 0.1-VO₂, 0.5-VO₂ respectively. For a

comparative study, one film was kept untreated and labelled as VO₂. To study the reversible nature of the films, dehydrogenation of the 0.001-VO₂ and 0.1-VO₂ films was done by heating at 343K for the two hours; the films were coded as DH-0.001-VO₂ and DH-0.1-VO₂, respectively.

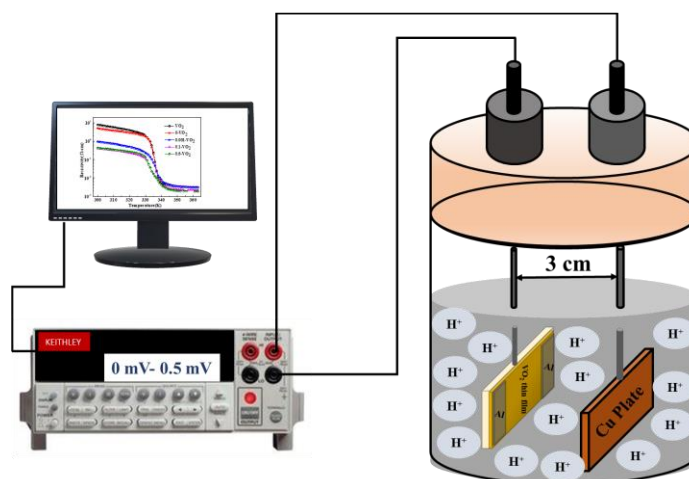


Figure 4.1: Schematic diagram of the hydrogenation process.

The prepared thin films were systematically investigated using the following characterization techniques. X-ray diffraction (XRD) measurements were taken using the Bruker D2 Phaser diffractometer with Cu K α source to determine the phase and crystallinity of the films. Rigaku Smart Lab diffractometer was used for X-ray reflectivity (XRR) to determine the thickness of the film. A Park Systems, NX10 Atomic force microscope (AFM) was used to check the surface morphology and roughness. For local structure analysis, temperature-dependent Raman spectroscopy was performed using Horiba LabRam HR Evolution spectrometer in micro-Raman mode. He-Ne LASER excitation source of wavelength 632.8nm with very low laser power was used to avoid overheating. The temperature range was kept 173-343 K using a temperature controller and LN2 cooling module. To analyze the electronic behavior, temperature-dependent resistivity measurements were carried out using a four-probe method with a home-made apparatus consisting of a heater, an air-cooling unit and a temperature controller. Measurement was performed with a heating rate of 1K/min in the temperature range 300K to 353K.

4.3 Results and discussion

4.3.1 Structural Analysis

Figure 4.2 shows the full-scale XRD pattern of the pristine and hydrogenated VO₂ thin films. XRD pattern is free of any impurity peak and shows (020) and (040) reflections corresponding to the monoclinic structure of VO₂.

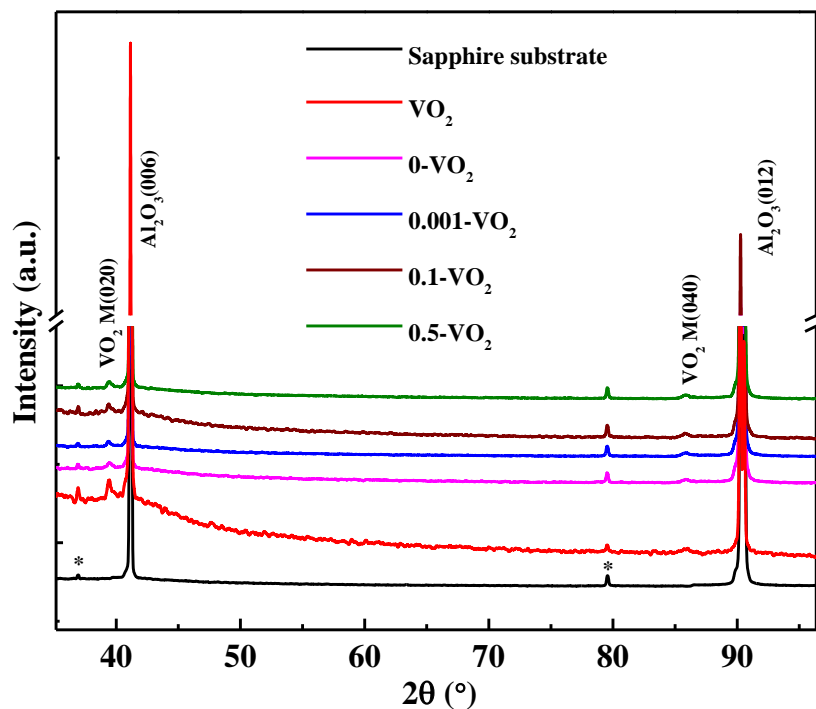


Figure 4.2: Full-scale XRD patterns of VO₂ thin films and sapphire substrate. XRD peaks other than (00*l*) reflections from a substrate are marked by *.

For a better understanding of the effect of the hydrogenation at different voltages magnified (020) peak of the films is shown in figure 4.3. Films hydrogenated at different voltages show the shift towards the lower Bragg's angle, which confirms the incorporation of the hydrogen in the VO₂ thin film [1,6]. Moreover, these shifts indicate the tendency of the films to change the structure from the monoclinic phase towards the rutile phase with the incorporation of the H⁺ ions into the VO₂ matrix at the negative applied voltage. This structural transformation is caused by the interstitially doped hydrogen that forms dynamic bonds with

oxygen and leads to expansion of the unit cell. For the film hydrogenated at the different voltages, (020) peak broadening takes place as compared to pristine VO₂ thin film, which is described in the latter part of the text.

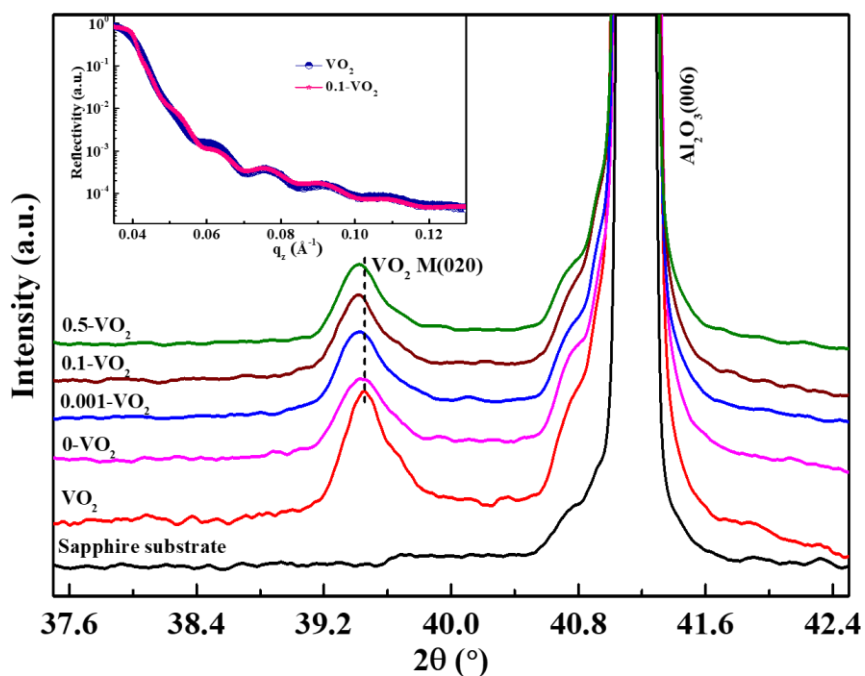


Figure 4.3: Magnified view of (020) diffraction peak of pristine and hydrogenated VO₂ thin films grown on the Al₂O₃ substrate; inset shows the XRR spectrum.

4.3.2 Surface analysis

Figure 4.4 shows AFM images of pristine and hydrogenated films. All films show uniform surface morphology. The observed root mean square (RMS) roughness was 2.74, 1.05, 1.7 nm respectively for VO₂, 0-VO₂, 0.1-VO₂. Roughness of hydrogenated films is found to decrease with hydrogen inclusion, *i.e.*, smoothness gets improved after the hydrogenation process. These results validate the broadening in the XRD peaks. AFM images were taken after three to four cycles of hydrogenation and dehydrogenation. As the images show, the hydrogenation process is not affecting the uniformity of the films. In order to check the sustainability of the films, XRR measurement was performed after three-four cycles of hydrogenation and dehydrogenation. The calculated thickness for VO₂ and 0.1-VO₂ films

is found to be nearly 40 nm (inset of figure 4.3). The above results confirm the reliability of the said method for the hydrogenation without damaging the films.

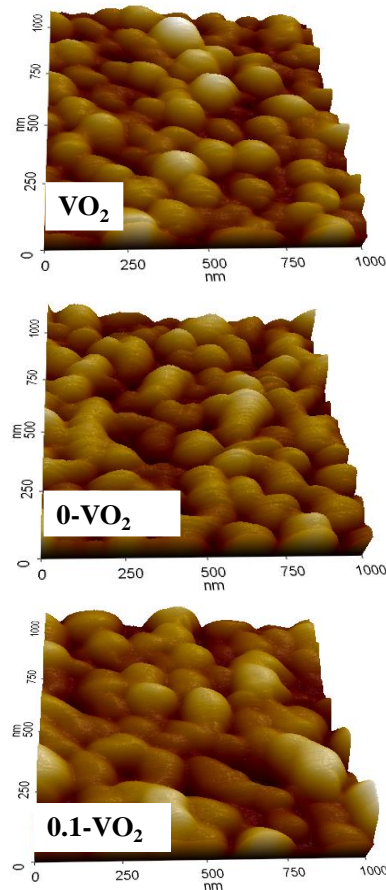


Figure 4.4: AFM images of VO₂, 0-VO₂, 0.1-VO₂ films.

4.3.3 Local structure

The local structures of pristine and hydrogenated thin films were analyzed using the room temperature Raman spectroscopy. Figure 4.5 shows the Raman spectra of all the films recorded at room temperature. According to the group theory, for the monoclinic phase of the VO₂ total of 18 Raman active phonon modes (9A_g + 9B_g) are predicted, and rutile phase of VO₂ can be identified by four very broad spectra (A_{1g} + B_{1g} + B_{2g} + E_g) [7]. However, a featureless broad spectrum gives the confirmation of rutile phase in VO₂. For all thin films, we observed total 10 Raman active modes at ~ 147, 194, 223, 306, 336, 384, 616, 267, 440, 497 cm⁻¹, representing the monoclinic phase of VO₂ [8]. Modes of

low frequency represent the vibrations due to V-V pairing and its tilting, whereas modes of high energy show the V-O vibrations. The low-frequency Raman modes due to V-V vibrations shift gradually towards lower wave number as seen in the inset of figure 4.5. With the increasing applied voltage, the H^+ ions penetrate in the lattice and drive the structure towards a higher symmetry, hence elongating the V-V bond length and softening the phonon modes [9]. Furthermore, it may be noted that deposition of the pure VO_2 thin films is a challenging task because the most stable phase of vanadium is V_2O_5 and not VO_2 . To verify phase-purity using Raman spectra, the room temperature Raman spectra of the film were purposely recorded up to 1100 cm^{-1} . The absence of the most common mode corresponding to the V_2O_5 phase at 995 cm^{-1} confirms the phase purity of the films.

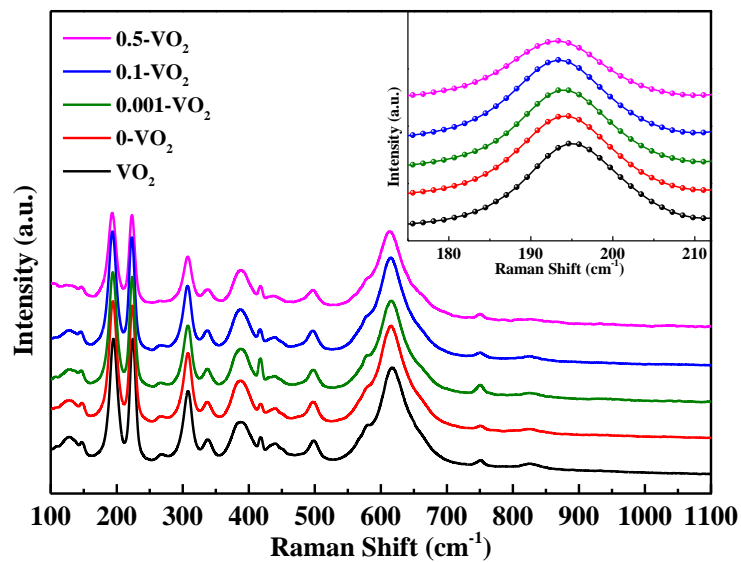


Figure 4.5: Room temperature Raman spectra of pristine and hydrogenated VO_2 thin films on Al_2O_3 substrate. Inset shows the magnified view of the most intense phonon mode (at 194 cm^{-1}).

Temperature-dependent Raman spectroscopy re-emphasized the earlier results. Figure 4.6 shows the temperature-dependent Raman spectra of VO_2 and $0.5-VO_2$ thin films. As can be seen, there is an expected shift towards lower wavenumber due to thermal expansion in both films with increasing temperature. For VO_2 thin films, the modes

start to diminish, and we get a featureless spectrum representing the rutile structure at 343K and the same is observed for the 0.5-VO₂ thin film at 333K. Due to the mixed-phase nature of the hydrogenated films, the modes start to diminish gradually at a lower temperature than that for the pristine one.

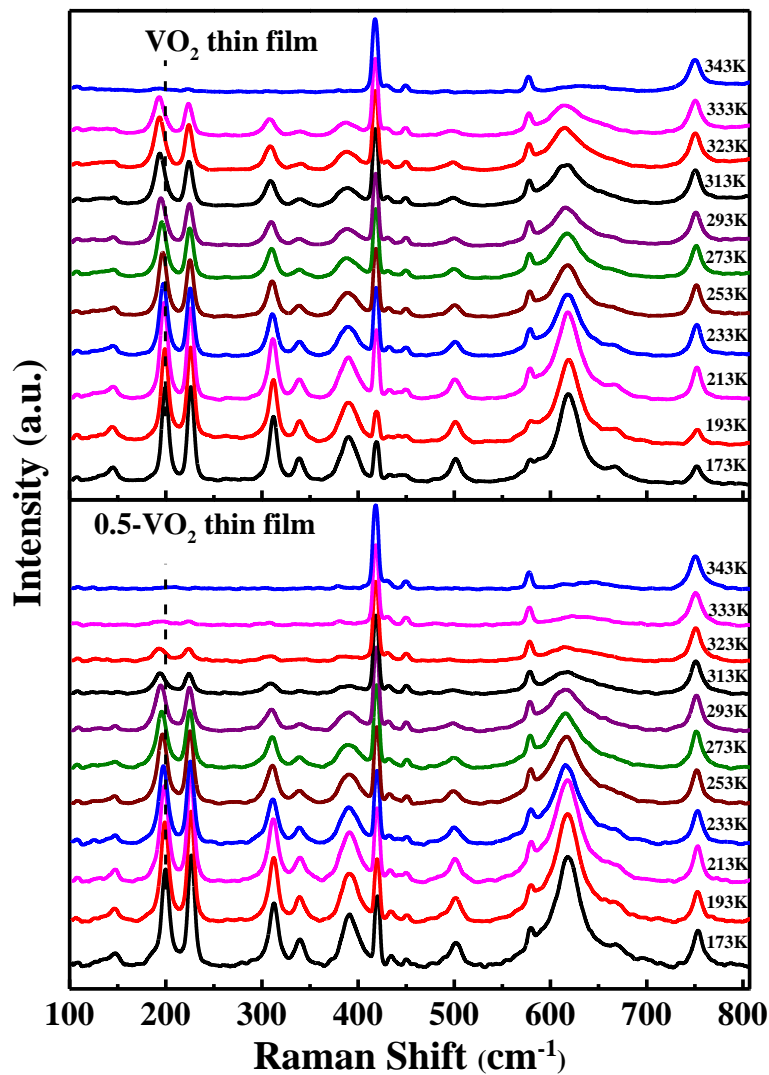


Figure 4.6: Temperature-dependent Raman spectra of VO₂ and 0.5-VO₂ films.

To further analyze the structural changes with increasing temperature, Raman shift of the most intense mode (194 cm⁻¹) at different temperatures for both the films were plotted in figure 4.7. The expected softening of phonon modes is observed due to thermal

expansion. The relationship between the thermal expansion and the temperature can be best represented by the given equation [10]:

$$\omega(T) = \omega_0 + \chi T \quad (4.2)$$

Where ω_0 is the phonon frequency at 0K, $\omega(T)$ is the frequency at temperature T and χ is the temperature coefficient of thermal expansion. The most intense low-frequency phonon mode (194 cm^{-1}) versus temperature plots were analyzed using the linear fit, as shown in figure 4.7 and the thermal expansion coefficient (χ) was calculated for VO_2 and 0.5-VO_2 films. The obtained values of χ were $0.040 \text{ cm}^{-1}\text{K}^{-1}$ and $0.042 \text{ cm}^{-1}\text{K}^{-1}$, respectively. This difference in the χ solely due to hydrogenation since the thermal effect is the same for both films.

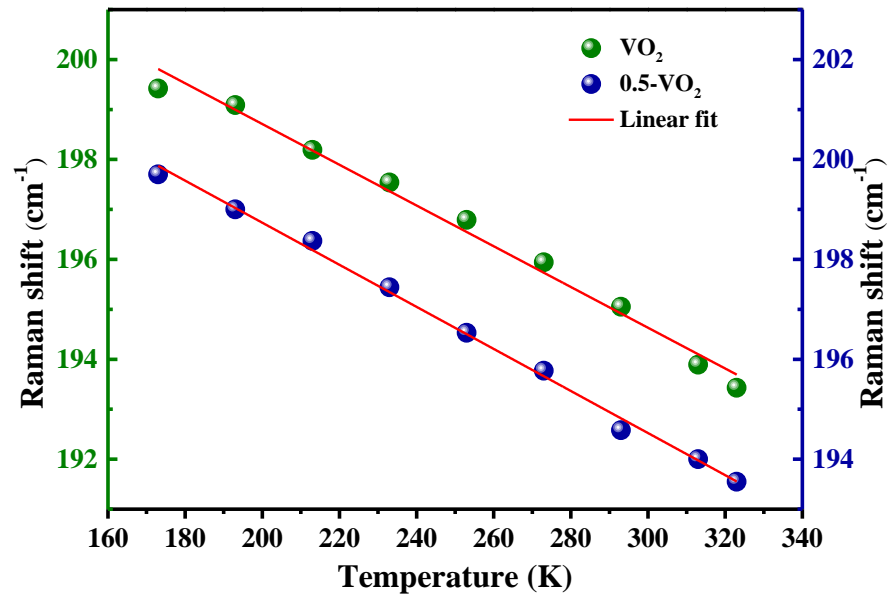


Figure 4.7: Linearly fitted temperature-dependent Raman-shift of the most intense mode (~at 194 cm^{-1}).

Hence, the softening of mode in VO_2 thin films is due to the elongation of V-V bonds by thermal expansion. However, in 0.5-VO_2 thin films, the softening of modes takes place because of two combined effects, namely the thermal expansion and the coexistence of the monoclinic and rutile phase as a result of hydrogenation.

For further confirmation on the effect of hydrogenation, the relative intensities of the peaks were examined. Since the intensity of the Raman mode is associated with the amount of the monoclinic structure [11]. Figure 4.8 shows the temperature dependence of relative intensities of the highest-intensity phonon mode of VO₂, *i.e.* mode at 194 cm⁻¹ and the substrate (Al₂O₃) intense mode, *i.e.* mode at 412 cm⁻¹. A sharp depletion in the intensity of 0.5-VO₂ as compared to pristine VO₂ is observed. Since with the inclusion of the hydrogen, the monoclinic (insulating) phase is tending towards the more symmetric rutile (metallic) phase and as a result hydrogenated films attains the coexistence of monoclinic and rutile phase. Hence, the decrement in intensity is twofold for the hydrogenated film. Firstly, due to an increase in crystal symmetry, the total number of phonon modes decreases. Secondly, the high carrier absorption due to the coexistence of more conductive phase reduces the intensity of the incident light, leading to a weaker detected signal [11].

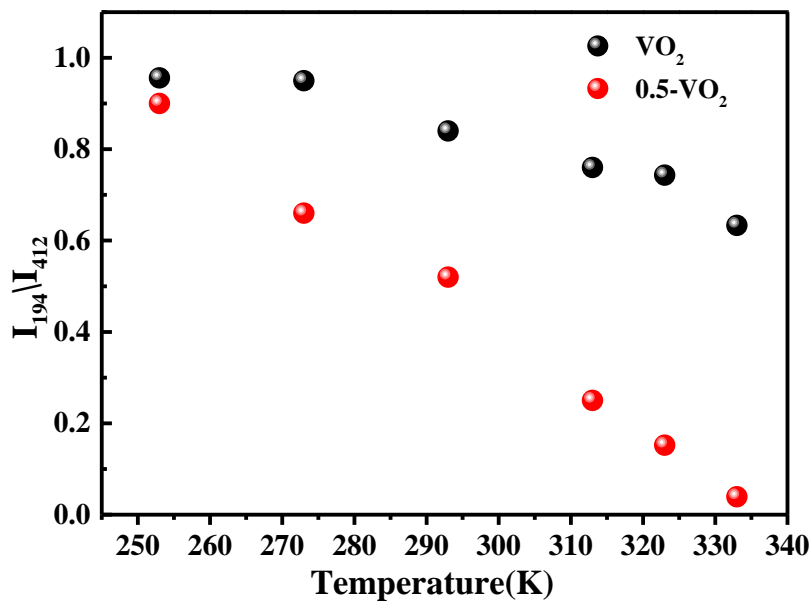


Figure 4.8: Variation in low-frequency mode intensities with temperature for VO₂ and 0.5-VO₂ films.

4.4.4 Electronic properties

Figure 4.10 shows the temperature-dependent electrical resistivity plots of the pristine and hydrogenated films. VO₂ films show the 3-order change in resistivity across the phase transition temperature (T_{MI}) at 336K, where T_{MI} is slightly lower than that for the bulk VO₂ [12]. It is clear from the figure that, the film hydrogenated without electric field, *i.e.*, film hydrogenated at the 0mV (in absence of electric field) shows only a slight variation in the resistivity below T_{MI} as compared to the pristine one. However, below the T_{MI}, a drastic (~ 1 order) decrement in resistivity of the film subjected to only a small electric field (.001mV per 3cm) is observed. The large effect of a small applied electric field can be explained as follows. This film is kept attached to the negative electrode with very small voltage (0.001mV) for 30 sec, which attracts much larger amount of H⁺ ions towards the films, which adds to the reduction of the resistivity, also because of the coexistence of monoclinic and rutile phases in the film. On applying an increased value of the voltage of 0.1mV, the resistivity further decreases. On further increase in the voltage to 0.5mV, the change in room temperature resistivity is negligible. Moreover, a slight decrement in the phase transition temperature is observed for 0.1-VO₂ and 0.5-VO₂ thin films, which takes place as a result of the distortion of the crystal structure after hydrogenation [13]. The distorted structure appears as a result of the formation of the H-O bond between the interstitially doped hydrogen and the oxygen which finally affects the valence state of the vanadium, as confirmed through our previous study (chapter-3) by XPS [4].

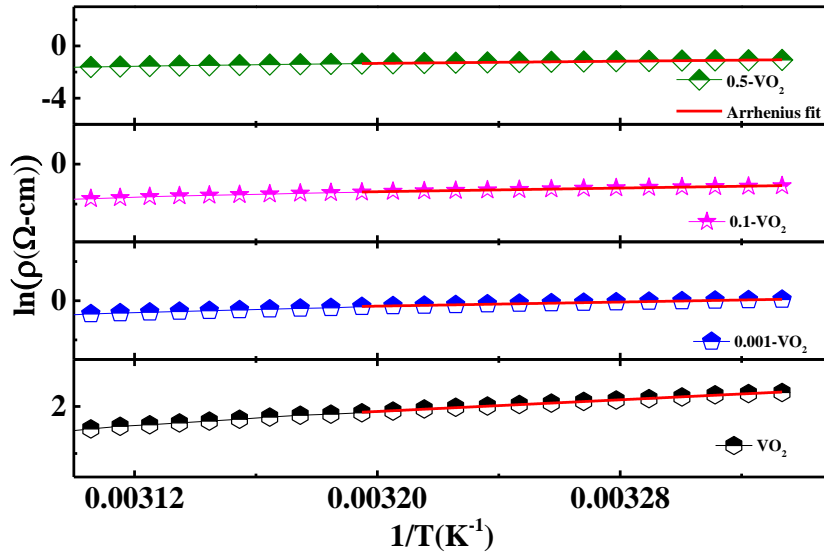


Figure 4.9: Arrhenius fitting of VO₂ and hydrogenated VO₂ thin films in the temperature region (313K-300K).

The activation energies for the thin films in the insulating region can be calculated using the Arrhenius equation given as

$$\rho = \rho_0 \exp\left(\frac{E_a}{k_B T}\right) \quad (4.3)$$

where E_a is the activation energy, and k_B is Boltzmann constant. Figure 4.9 shows the Arrhenius fitting in the temperature region (313-300 K). The activation energy and room temperature resistivity are found to be decreasing with the increasing applied voltage as listed in table 4.1.

Table 4.1: Peak position of the most intense Raman mode, room temperature resistivity, activation energy of pristine and hydrogenated VO₂ thin films.

Samples	Raman mode (cm ⁻¹)	RT resistivity (Ω-cm)	Activation energy (m eV)
VO ₂	195.21	9.933	267
0.001-VO ₂	194.09	1.057	225
0.1-VO ₂	193.42	0.343	196
0.5-VO ₂	192.98	0.336	178

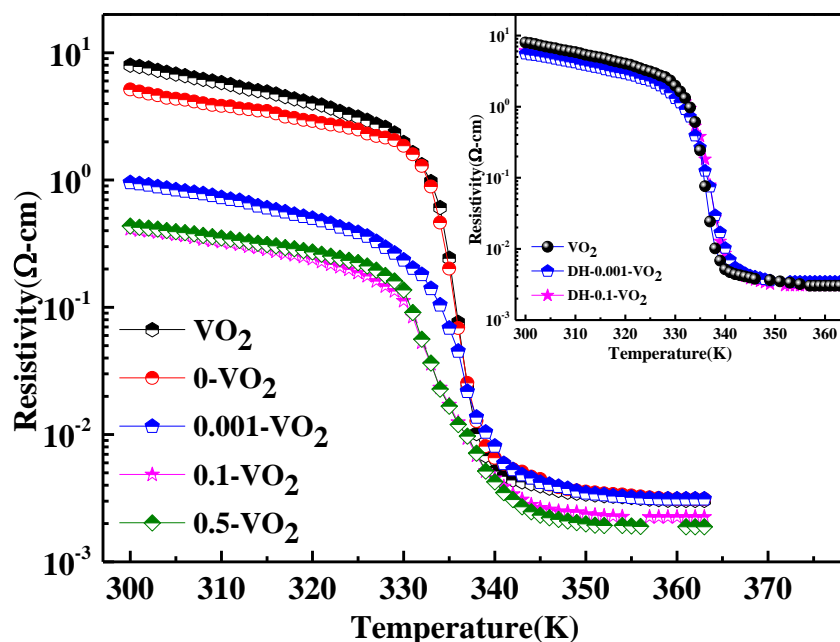


Figure 4.10: Temperature-dependent resistivity curves of pristine and hydrogenated VO₂ films, inset shows temperature versus resistivity curve of VO₂, DH-0.001-VO₂ and DH-0.1-VO₂ films.

In order to check the reversible nature of the hydrogenation in the films, a de-hydrogenation of the films was performed. Inset of figure 4.10 shows the resistivity curves after dehydrogenation of the films, and it is seen that the films gain their actual state after the dehydrogenation, which demonstrates the excellent reversibility of the films. Our results suggest that an easy insertion of H⁺ into VO₂ channel at *room temperature* and extreme reversibility of the films is also an outcome of highly crystallographically oriented VO₂ thin films. Further investigations of this very promising method are necessary in order to optimize the rapidity of the hydrogenation, application of voltage as well as new designs of the metal contacts and distance may be tested.

4.4 Summary

Five thin films of VO₂ were synthesized under the identical deposition conditions and studied for the hydrogenation under the effect of applied voltage in an ionic liquid solution. Four films were hydrogenated under four different voltages at room temperature. The films were placed as a negative electrode with aluminum contacts to

mediate the surface diffusion of hydrogen in the solution. With increased voltage, a systematic shift in the XRD peaks was observed, which is an indication of a gradually changing structure from the monoclinic to the rutile phase of VO₂. The atomic force micrographs show uniformly deposited films. The surfaces of the films remained unaffected even after 3-4 cycles of hydrogenation and dehydrogenation. Thus, there was no etching of the films, and the films are reusable. Room temperature Raman analysis confirmed the changing microstructure with the incorporation of hydrogen. The effects of hydrogenation were further emphasized by the analysis of the temperature-dependent Raman spectroscopy. A dramatic decrease in the *room temperature* resistivity was obtained by applying a trivial voltage 0.001mV for 30s during the hydrogenation. Resistivity measurements showed a clear picture of the success of the experiment. The films also confirmed high reversibility of the original state when tested with resistivity measurements. The method gives a quick, easy and affordable way to hydrogenate VO₂ thin films at room temperature, keeping the films intact and sustainable even after the several cycles of the hydrogenation and dehydrogenation.

References:

- [1] H. Yoon, M. Choi, T.W. Lim, H. Kwon, K. Ihm, J.K. Kim, S.Y. Choi, J. Son, Reversible phase modulation and hydrogen storage in multivalent VO₂ epitaxial thin films, *Nat. Mater.*, 15, (2016), 1113–1119.(DOI:10.1038/nmat4692).
- [2] C. Wu, F. Feng, J. Feng, J. Dai, L. Peng, J. Zhao, J. Yang, C. Si, Z. Wu, Y. Xie, Hydrogen-incorporation stabilization of metallic VO₂ (R) phase to room temperature, displaying promising low-temperature thermoelectric effect, *J. Am. Chem. Soc.*, 133, (2011), 13798–13801.(DOI:10.1021/ja203186f).
- [3] S. Chen, Z. Wang, L. Fan, Y. Chen, H. Ren, H. Ji, D. Natelson, Y. Huang, J. Jiang, C. Zou, Sequential insulator-metal-insulator phase transitions of VO₂ triggered by hydrogen doping, *Phys. Rev. B.*, 96, (2017), 1–6. (DOI:10.1103/PhysRevB.96.125130).
- [4] K. Mulchandani, A. Soni, K.R. Mavani, Structure influenced rapid hydrogenation using metal-acid contacts on crystallographically oriented VO₂ thin films, *Appl. Surf. Sci.*, (2020), 148369. (DOI:10.1016/j.apsusc.2020.148369).
- [5] S. Chen, Z. Wang, H. Ren, Y. Chen, W. Yan, C. Wang, B. Li, J. Jiang, C. Zou, Gate-controlled VO₂ phase transition for high-performance smart windows, *Science Advances*, 5, (2019), eaav6815,1–9. (DOI:10.1126/sciadv.aav6815)
- [6] Y. Zhao, G. Karaoglan-Bebek, X. Pan, M. Holtz, A.A. Bernussi, Z. Fan, Hydrogen-doping stabilized metallic VO₂ (R) thin films and their application to suppress Fabry-Perot resonances in the terahertz regime, *Appl. Phys. Lett.*, 104, (2014), 241901. (DOI:10.1063/1.4884077).
- [7] P. Shvets, O. Dikaya, K. Maksimova, A. Goikhman, A review of Raman spectroscopy of vanadium oxides, *J. Raman Spectrosc.*, 50, (2019), 1226–1244. (DOI:10.1002/jrs.5616).

- [8] C. Marini, E. Arcangeletti, D. Di Castro, L. Baldassare, A. Perucchi, S. Lupi, L. Malavasi, L. Boeri, E. Pomjakushina, K. Conder, P. Postorino, Optical properties of $V_{1-x}Cr_xO_2$ compounds under high pressure, *Phys. Rev. B*, 77, (2008), 235111. (DOI:10.1103/PhysRevB.77.235111).
- [9] E. Evlyukhin, S.A. Howard, H. Paik, G.J. Paez, D.J. Gosztola, C.N. Singh, D.G. Schlom, W.C. Lee, L.F.J. Piper, Directly measuring the structural transition pathways of strain-engineered VO_2 thin films, *Nanoscale.*, 12, (2020), 18857–18863. (DOI:10.1039/d0nr04776g).
- [10] X. Gong, H. Wu, D. Yang, B. Zhang, K. Peng, H. Zou, L. Guo, X. Lu, Y. Chai, G. Wang, X. Zhou, Temperature dependence of Raman scattering in single crystal SnSe, *Vib. Spectrosc.*, 107, (2020), 103034. (DOI:10.1016/j.vibspec.2020.103034).
- [11] S. Chen, X.J. Wang, L. Fan, G. Liao, Y. Chen, W. Chu, L. Song, J. Jiang, C. Zou, The Dynamic Phase Transition Modulation of Ion-Liquid Gating VO_2 Thin Film: Formation, Diffusion, and Recovery of Oxygen Vacancies, *Adv. Funct. Mater.*, 26, (2016), 3532–3541. (DOI:10.1002/adfm.201505399).
- [12] F.J. Morin, Oxides which show a metal-to-insulator transition at the neel temperature, *Phys. Rev. Lett.*, 3, (1959), 34-36. (DOI:10.1103/PhysRevLett.3.34).
- [13] V.N. Andreev, V.A. Klimov, M.E. Kompan, Influence of hydrogenation on electrical conductivity of vanadium dioxide thin films, *Phys. Solid State.*, 54, (2012), 601–606. (DOI:10.1134/S1063783412030043).

Chapter 5

Tuning of structural and electronic transitions by tungsten doping in VO₂ thin films

In this chapter, A series of seven V_{1-x}W_xO₂ (x=0, 0.005, 0.01, 0.015, 0.02, 0.03, 0.04) thin films have been deposited on single-crystal sapphire substrates using PLD technique with a motive to understand the structural transformation simultaneous to electronic transition. The effects of the substitutional doping of W at V-site on the structural and electronic properties of the VO₂ thin films have been investigated. A minor level of doping of tungsten (W) transforms the structure significantly. The results presented in this chapter are published in the peer-reviewed journal^Ψ.

^ΨMulchandani *et. al.*, *Superlattices and Microstructures*, **154** (2021) 106883
(doi.org/10.1016/j.spmi.2021.106883)

5.1 Introduction

VO₂ thin film-based devices rely on its unique MIT, which is very close to the room temperature, which means the phase transition temperature of pristine VO₂ thin films can be too high or too low for practical applications. Thus, tuning of the transition temperature according to the requirement is crucial for cost effective device fabrication. Transitions of VO₂ can be tuned *via* strain [1], doping [2,3], oxygen content [4] *etc.* . Doping of an element can be an easy and feasible option for the fine-tuning of the transition temperature. In the past, in order to increase the transition temperature, Al [5], Fe [6], and Cr [7] have been used as dopant elements; particularly, high-valent transition metals such as Nb [8], Mo [9], and W [10,11] have been used as dopants to decrease the transition temperature of VO₂ thin films. However, W has been shown to be the most effective in influencing the MIT. High-valence elements such as W, introduce the extra electrons into the 3*d* band of vanadium by charge compensation mechanism. Hence, the substitutional doping of the W⁶⁺ in the place of V⁴⁺ shows a remarkable reduction in the phase transition temperature [12].

Recently the effects of the higher valence atom (W) doping on the electronic and optical properties of VO₂ films have been reported [11,13,14]. Yet, only a few reports are available on *the structural properties* of crystalline VO₂ films. In this work, we have studied the changes in structural and electronic properties of the crystallographically oriented pulsed laser deposited VO₂ thin films with increasing W doping at a *minor level* (V_{1-x}W_xO₂; *x*=0, 0.005, 0.01, 0.015, 0.02, 0.03, 0.04). These results can be useful in fine-tuning of structural as well as electronic properties of VO₂ thin films using W doping.

5.2 Experimental

Bulk samples of V_{1-x}W_xO₂ (*x*=0, 0.005, 0.01, 0.015, 0.02, 0.03, 0.04) were prepared using solid-state reaction method. For making the pellets, high purity powders of V₂O₃ (> 99.99 % pure) and WO₃ (> 99.99 % pure) were mixed in appropriate molar ratios. The mixture of powders was ground for 3-4h in order to make a homogeneity and then pressed

into pellets using a hydraulic press. The pellets were sintered at 1000°C in Ar atmosphere for 24h simultaneously. Thin films were deposited on single crystal *c*-cut sapphire (Al₂O₃) substrate by pulsed laser deposition technique using a KrF excimer laser ($\lambda = 248$ nm). For all depositions, laser energy fluence was set at 2.5 mJ, and the repetition rate was 5 Hz. The distance between target and substrate was kept at 4 cm, and substrate temperature was maintained at 650°C during deposition. Before target ablation, the chamber was evacuated to a base pressure of the order of 10⁻⁴ Pa. During the growth of thin films, oxygen partial pressure was maintained at 4 Pa.

For the structural analysis of thin films, X-Ray Diffractometer (XRD) was performed using a Rigaku Smart Lab with the Cu K _{α} source. In order to further analyze the local structure of the thin films, temperature-dependent Raman spectra, were recorded with Horiba LabRam HR Evolution spectrometer with 633nm laser as the excitation source. The Raman spectroscopy measurements were performed in the temperature range of 170K to 303K using a temperature controller and liquid nitrogen cooling module. For the morphological study, the Atomic Force Microscopy (AFM) (Park Systems, NX10) was used. X-ray photoelectron spectroscopy (XPS) was performed using the BL-14 beamline of the Indus-2 synchrotron source, RRCAT, Indore, India, with a monochromatic X-ray beam of 4357eV energy. The temperature-dependent resistivity measurements of the samples were performed while warming the samples using closed-cycle cryostat, using a four-point probe method.

5.3 Results and Discussion

5.3.1 structure and morphology

Figure 5.1 shows the full scale XRD patterns of the undoped (40 nm) [15] and W-doped VO₂ thin films deposited on sapphire substrate. The (020) and (040) peaks of VO₂ thin films for doped and undoped films are detected. There is no peak observed related to other crystalline phases of vanadium oxide, and no sign of diffraction peak corresponding

to any impurity or unreacted tungsten oxides. Thus, W has been doped at V-site, and these thin films are highly pure and crystalline in nature. The films remain crystallographically oriented and free of any impurity even after 4 at% of (highest) doping.

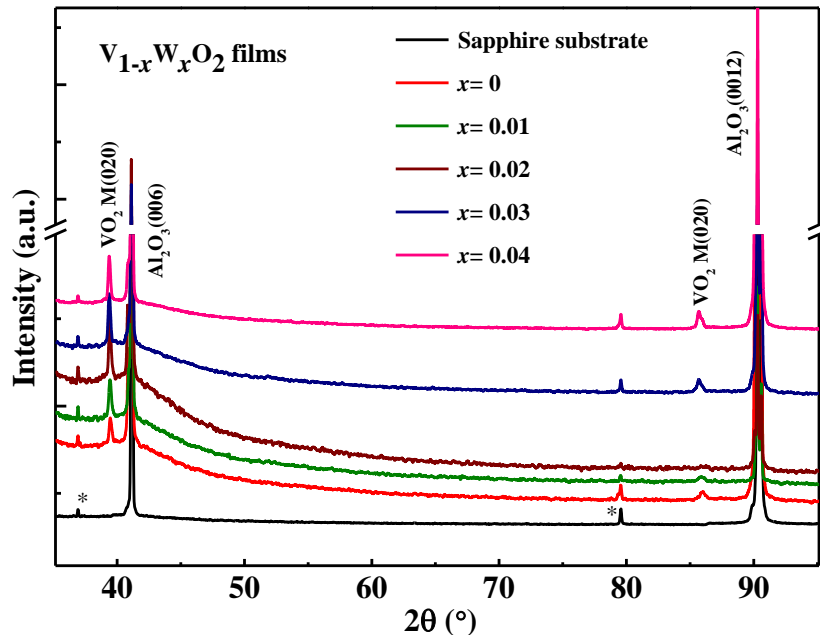


Figure 5.1: Full-Scale XRD patterns of undoped and W-doped VO₂ thin films and sapphire substrate. XRD peaks other than (00*l*) reflections from substrate are marked by ‘*’.

Figure 5.2 shows the magnified view of (020) peak of VO₂ and W-doped VO₂ thin films. With the inclusion of W content in VO₂ matrix, (020) peak shifts towards lower diffraction angle which reveals that structure enlarges and accommodates itself in the rutile structure [11]. The lattice parameter ‘*b*’ was calculated using 2θ values of (020) peak and found to be increasing with W doping. Figure 5.3 gives the variation in the Bragg’s angle and lattice constant with different doping concentrations. The substitutional incorporation of W⁶⁺ in place of V⁴⁺ ion enlarges the lattice structure due to the larger ionic radii of W⁶⁺. Due to this, the lattice constant increases with the increased doping percentage [12].

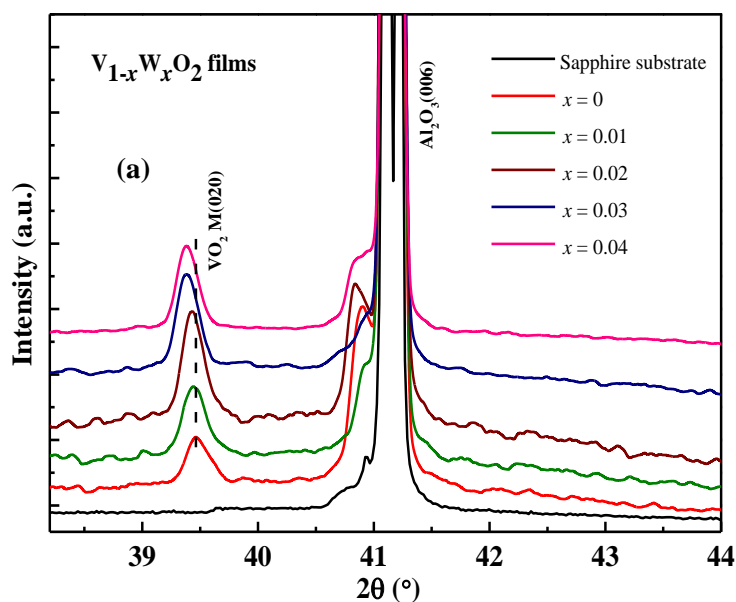


Figure 5.2: XRD patterns showing (020) reflection of $V_{1-x}W_xO_2$ ($x=0, 0.01, 0.02, 0.03, 0.04$) thin films on sapphire substrate.

The full width at half maximum (FWHM) of (020) peak is calculated from the Gaussian fit of the curve and found to be decreasing with increasing W content. Hence, the crystallite size increased as calculated from the Scherrer's formula $D = K\lambda/\beta\cos\theta$, where D is the average crystallite size, K is Scherrer constant with a value close to unity, λ is the X-ray wavelength, β is the line broadening at half of the maximum intensity and θ is the Bragg angle. The increment in the crystallite size was further confirmed by calculation using AFM images too.

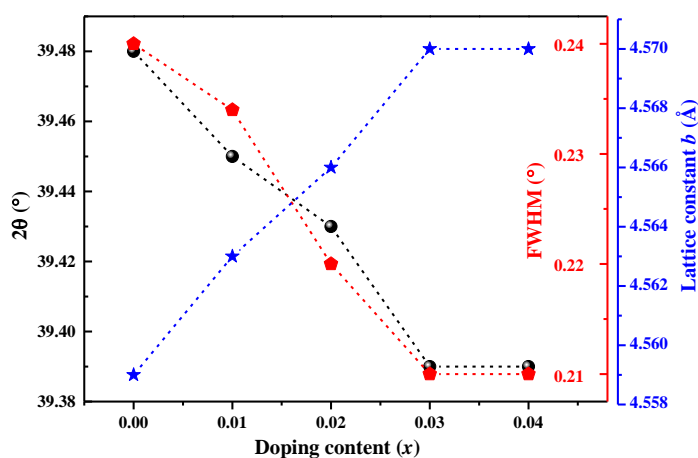


Figure 5.3: Variations in Bragg's Angle, FWHM and crystallite size of (020) peak of VO_2 thin films with different doping content.

The surface morphology of undoped and W-doped VO₂ thin films was examined using AFM in tapping mode. Figure 5.4 illustrates the granular microstructure and found to be highly uniform throughout the surface in all the films. With the increasing doping concentration of W into the VO₂ matrix, the average grain size is increasing, which supports the XRD results of increased crystallite size. Also, incorporation of W improves the smoothness of films since the root mean square (RMS) surface roughness decreases with enhanced W content. Indeed, the grain size is about 80, 105, 130 nm for VO₂, V_{0.99}W_{0.01}O₂ and V_{0.97}W_{0.03}O₂ respectively, while the corresponding roughness is about 4.70, 4.37, 3.42 nm.

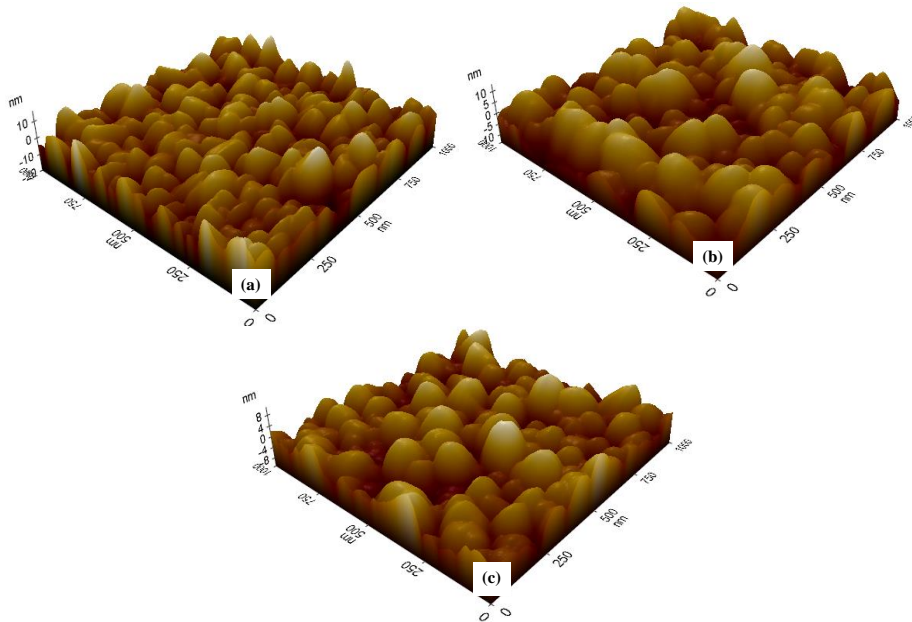


Figure 5.4: AFM images of (a)VO₂, (b)V_{99.99}W_{0.01}O₂, and (c)V_{99.97}W_{0.03}O₂ thin films grown on the sapphire substrate.

5.3.2 Local structure Analysis

To investigate the changes in the local structure with the inclusion of W doping, room temperature Raman spectra were recorded. Figure 5.5 shows the room temperature Raman spectra of the W doped and undoped films. The Monoclinic phase of VO₂ consists of 18 Raman active modes as predicted by the group theory, and the rutile phase of VO₂ gives the broad featureless spectra [16,17]. For pure VO₂ thin film,

we observed seven A_g and three B_g Raman modes at $\sim 147, 194, 223, 306, 336, 384, 616 \text{ cm}^{-1}$ and $267, 440, 497 \text{ cm}^{-1}$ respectively, which belong to the monoclinic (M1) phase of VO_2 . The remaining modes were observed due to the sapphire substrate [18]. Modes of low frequency represent the vibrations due to V-V pairing and its tilting, whereas modes of high energy depict the V-O vibrations [19].

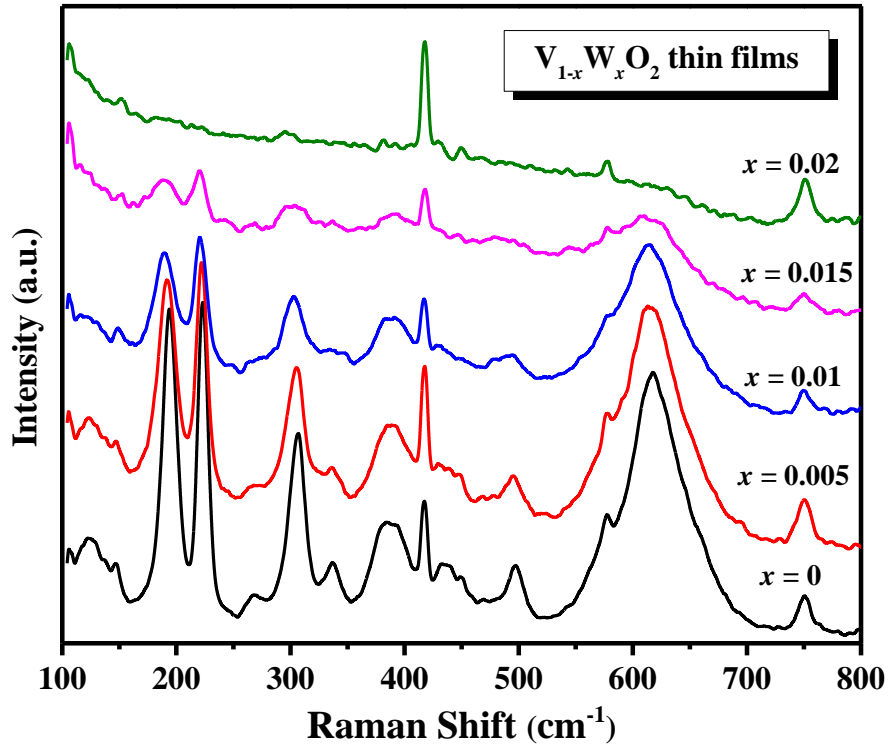


Figure 5.5: Room temperature Raman spectra of $\text{V}_{1-x}\text{W}_x\text{O}_2$ ($x=0, 0.005, 0.01, 0.015, 0.02$) thin films.

Figure 5.6 (a) shows that with the increasing doping percentage of W, the ratio of intensities of Raman active modes (low-frequency and high-frequency mode) are decreasing. This is because W doping starts to favor a more symmetric structure (rutile structure) [20]. Also, at a certain doping percentage, the modes start to disappear, which clearly indicates the complete transformation of the films into the rutile phase. Moreover, a softening and broadening of the most intense low-frequency mode (at 194 cm^{-1}) was observed with the increasing doping content, as shown in figure 5.6 (b). As already stated, that mode at 194 cm^{-1} represents the vibration of the V-V dimers. W^{6+} has a larger ionic radius as compared to V^{4+} as a result of which the substitution of V

atoms by W atoms leads to the elongation and straightening of the V-V bond [21]. Thus, due to the elongation of V-V bond, the Raman peaks shift towards lower energy (softening of the modes), and this validates the XRD results that the W doping is causing a shift from the structure of monoclinic VO₂ towards the rutile.

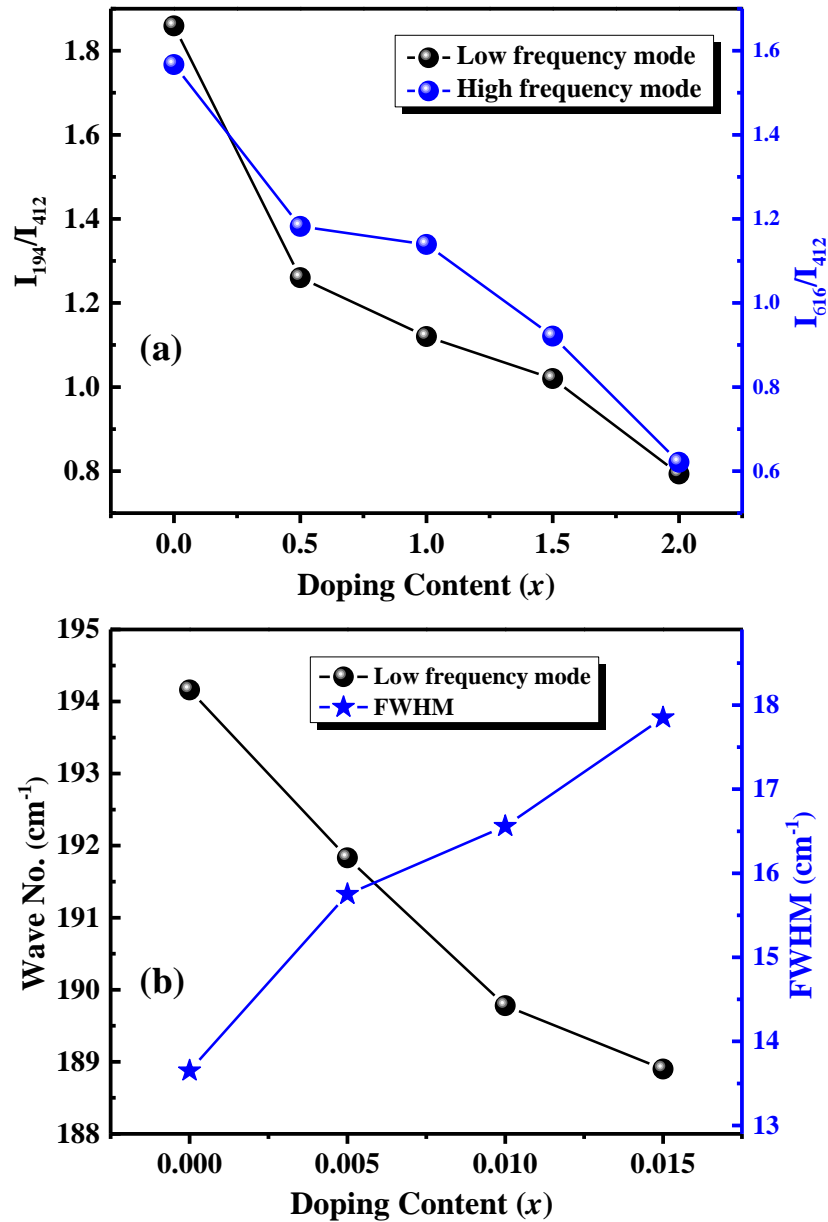


Figure 5.6: (a) Variation in intensity ratio of high and low frequency modes with different doping content. (b) Raman shift and FWHM of mode 194cm⁻¹ with different doping percentage.

Doping, stress, and deposition parameters can affect the phase transition, as well as the phase formation. Intermediate unstable phases

(M2 and T) can be formed as a result of doping. The formation of the M2 intermediate phase can be confirmed by the shifting of the high-frequency mode (613 cm^{-1}) and splitting of the mode at 225 cm^{-1} [22]. Analysis of the peak positions with the increase in the W content suggests that there is no emergence of the M2 phase from the M1 phase. The above observations indicate a structural transformation in the VO_2 thin films. As W is incorporated progressively in the lattice, it being a larger ion starts to favor a higher symmetry and hence the V-V dimers start to un-dimerize and elongate to give a rutile structure as shown in figure 5.7. Thus, a change in local structure with W doping was recorded.

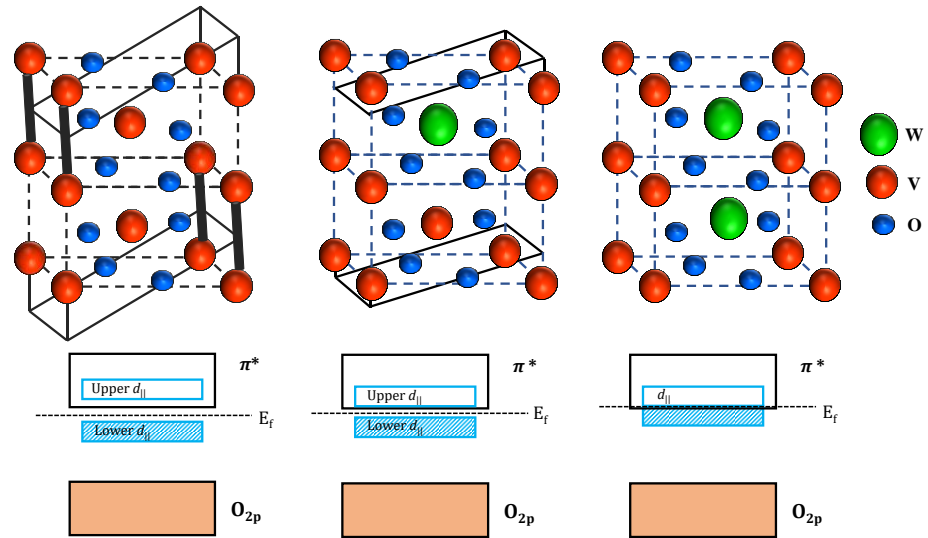


Figure 5.7: Top-panel shows the transformation of structure and bottom-panel shows the band structure variation with W doping. In the top panel, solid lines show the monoclinic structure and dashed lines show the inclination of the structure towards rutile phase.

In order to check the phase-related anomalies that can appear because of temperature variation, the temperature-dependent Raman spectra of the undoped (VO_2) and 2% W doped ($\text{V}_{99.98}\text{W}_{0.02}\text{O}_2$) were recorded [figure 5.8]. In the undoped films there is a gradual softening and broadening of the peaks in the low-frequency modes as shown in figure 5.8 (a), which can be attributed to the thermal expansion of the cells [21]. In case of doped films, a similar trend is observed but only below a certain temperature. It can be seen from figure 5.8 (b) that above

303 K the modes start disappearing gradually, which is suggestive of the formation of a rutile structure much below the transition temperature of pristine films. Again, as seen from the peak positions, there is no emergence of M2 phase from M1 phase. These observations of structural transformations corroborate very well with the electronic transitions as described in the later text.

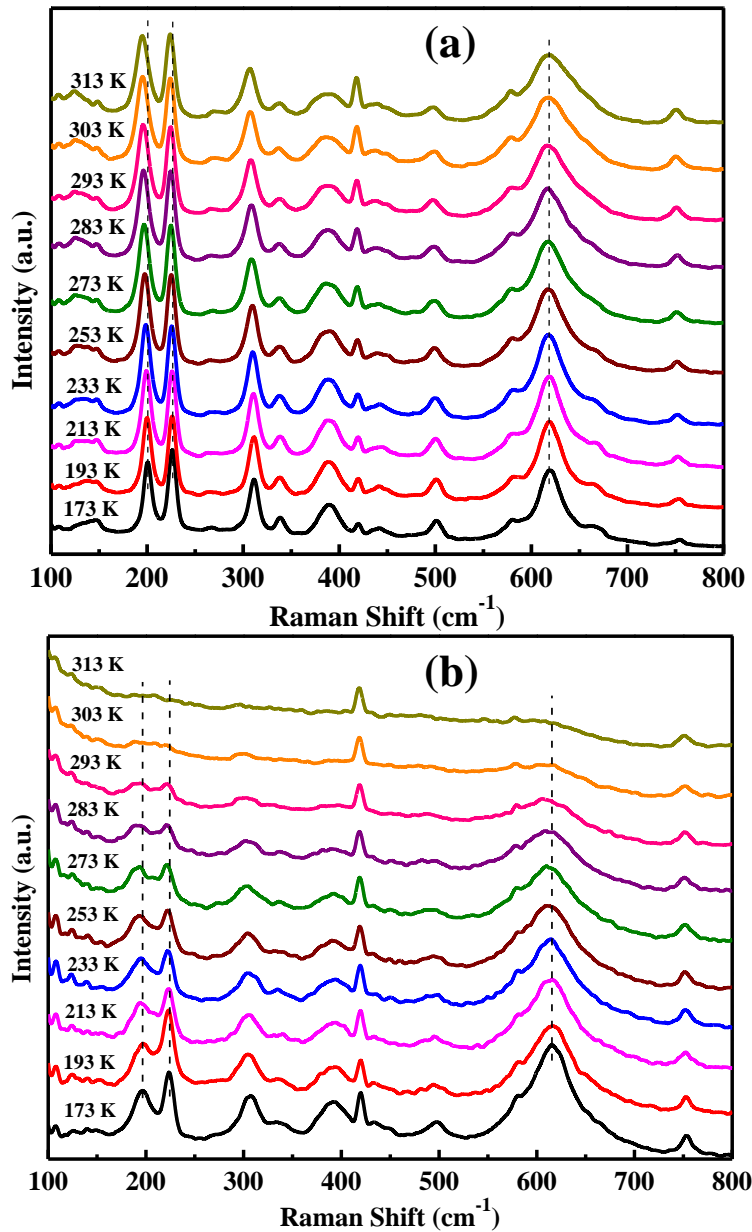


Figure 5.8: Temperature-dependent Raman spectra of (a) VO₂ and (b) V_{99.98}W_{0.02}O₂ thin films.

5.3.3 Chemical composition

The chemical composition of the films was analyzed using XPS. The carbon C1s peak is approximated to have a binding energy of 284.6 eV to calibrate the XPS spectra. A Shirley background subtraction is imposed using CASA software for the analysis. Figure 5.9 shows a survey spectrum of the VO₂ and V_{99.96}W_{0.04}O₂ thin films. O1s, V2s, V2p, V3s, V3p peaks can be observed in both films. The doped film, however, shows additional W4p and W4d peaks, which indicates the successful doping of W in the VO₂ films [13].

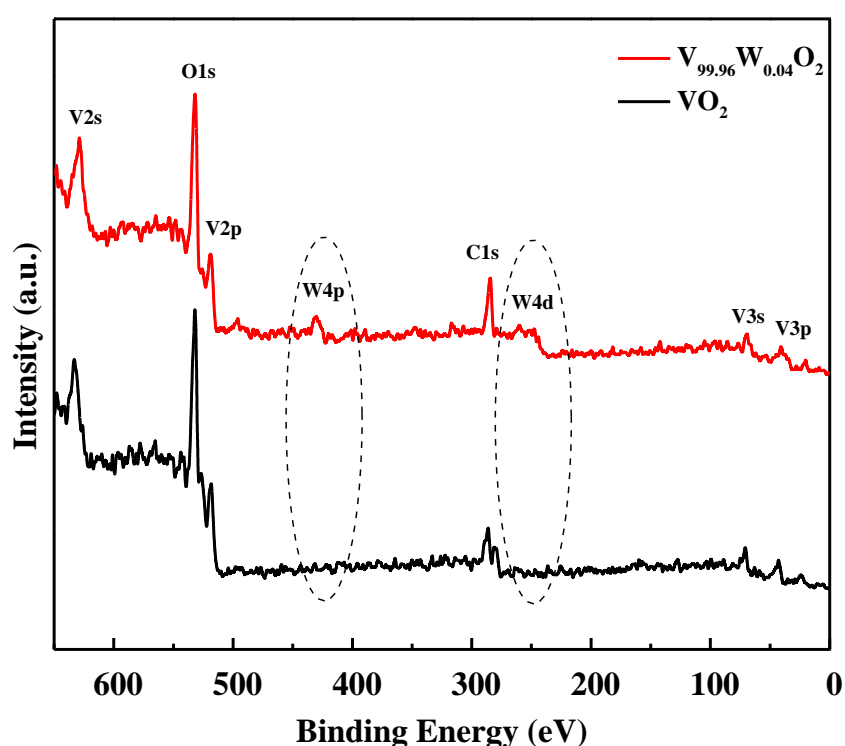


Figure 5.9: XPS survey spectrum of comparison of pure VO₂ and V_{99.96}W_{0.04}O₂ films.

To extract the exact information of the chemical state, high-resolution spectra were recorded for both the films as shown in figure 5.10. The O1s peak is deconvoluted into two peaks, one is corresponding to the H-O bond, which appears due to surface contamination of the films, and the other peak is due to V-O bond [23]. The V2p peak shows its two components *i.e.* V2p_{1/2} and V2p_{3/2}, with both having some contribution from V⁴⁺ as well as V⁵⁺ states. The V⁵⁺ states arise due to

the surface oxidation in both the films. In the case $V_{99.96}W_{0.04}O_2$ film, a new peak appears at 515.03eV. This peak corresponds to the V^{3+} valence state, which is resulted by the replacement of the V^{4+} by the W^{6+} ions [24]. Further, in the case of undoped films, the ratio of the percentage area of the V^{4+} to V^{5+} states is 1.8 and 1.2 in the $V2p_{1/2}$ and $V2p_{3/2}$ peaks, respectively. Similarly, for W-doped film the ratio of the percentage areas of V^{4+} to V^{5+} is 4.9 and 7.2, respectively, for the $V2p_{1/2}$ and $V2p_{3/2}$ states. This clearly indicates that the W doping decreases the formation of V^{5+} valence state in the films.

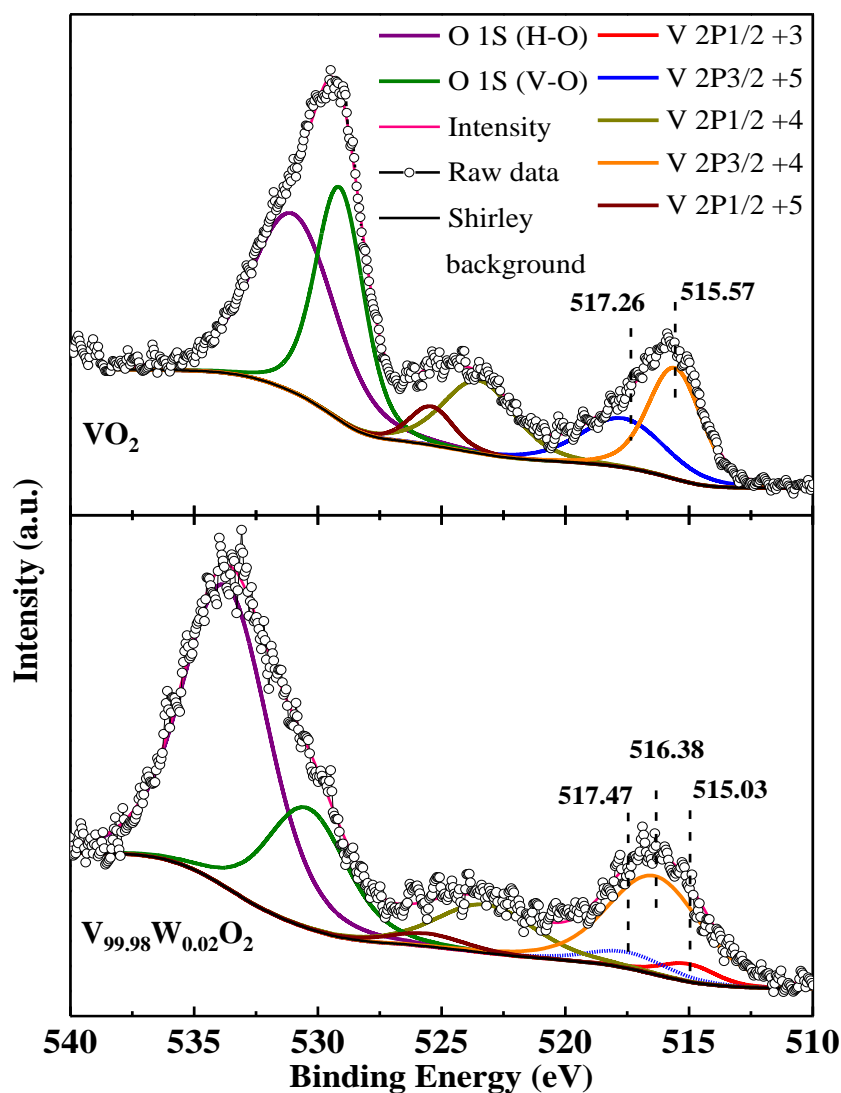


Figure 5.10: High-resolution XPS spectra for V2p and O1s of VO_2 and $V_{99.96}W_{0.04}O_2$ films.

As it can be observed from the figure 5.10, The binding energy of V^{4+} in the $V_{99.96}W_{0.04}O_2$ film is higher as compared to the VO_2 film. This is probably due to the replacement of V^{4+} ion with larger ionic radii of W^{6+} . Due to this replacement, the length of the V-O bond becomes shorter causing an increase in the binding energy [25]. Based on the above observations, it can be derived that W doping has stabilized V^{4+} state with an improved surface stoichiometry.

5.3.4 Metal to insulator transition characteristics

Figure 5.11 shows the temperature-dependent resistivity curves. W doping into VO_2 matrix shows a significant impact on the transition temperature. Phase transition temperature decreases as the W doping increases. The top inset in figure 5.11 shows the derivative plot of resistivity with temperature, representing the transition temperatures at different doping percentages. The transition temperature of the undoped VO_2 thin film is about 340K, which agrees well with reported results [26]. Further, the transition temperature of $V_{99.99}W_{0.01}O_2$ and $V_{99.985}W_{0.015}O_2$ are reduced to 322K and 300K, respectively. Transition width (ΔT), defined as the full width at half maximum of the derivative curve (inset of figure 5.11) increases with the increasing doping percentage, which indicates the reduction in the sharpness of the transition. Bottom inset of figure 5.11 clearly shows a very broad transition around at 180K for 4 at % W-doped films. Moreover, the resistivity below the transition temperature is also decreasing with the incorporation of W.

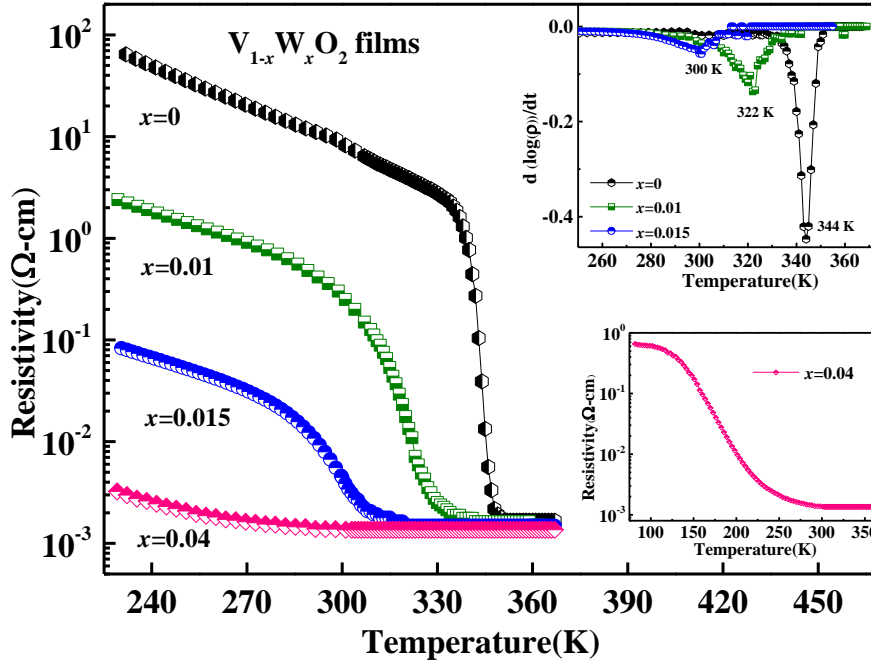


Figure 5.11: Temperature-dependent resistivity curves of $V_{1-x}W_xO_2$ ($x=0, 0.01, 0.015, 0.04$) thin films, top inset shows the corresponding derivative plots and bottom inset shows resistivity curve of $V_{1-x}W_xO_2$ ($x=0.04$) thin film in low temperature range.

The activation energy values give an idea of the electronic band gap. The activation energies for the thin films in the insulating region can be calculated using the Arrhenius equation given as:

$$\rho = \rho_0 \exp\left(\frac{E_a}{k_B T}\right) \quad (5.1)$$

where E_a is the activation energy and k_B is Boltzmann constant. Figure 5.12 shows the Arrhenius fitting in the temperature region (230K-280K) and obtained values of activation energies are shown in table 5.1. Thus, activation energy decreases with the increase in the doping percentage of W.

Table 5.1 Electronic transport properties for undoped and W-doped VO₂ thin films.

Sample	Transition temperature (K)	Transition width (K)	Activation energy (meV)
VO ₂	344	6	166
V _{99.99} W _{0.01} O ₂	322	11	130
V _{99.985} W _{0.015} O ₂	300	15	123

In the monoclinic state, the dimerization of the V-V atoms causes the localization of the V 3d t_{2g} orbitals and split them into d_{||} and π* sub-bands. Decrement in the transition temperature and activation energy can be due to the fact that the W doping narrows this band gap by weakening the dimerization of the V atoms as shown in figure 5.7 [21]. As we reach the rutile phase, the upper and lower d_{||} bands overlap completely making it a conductor.

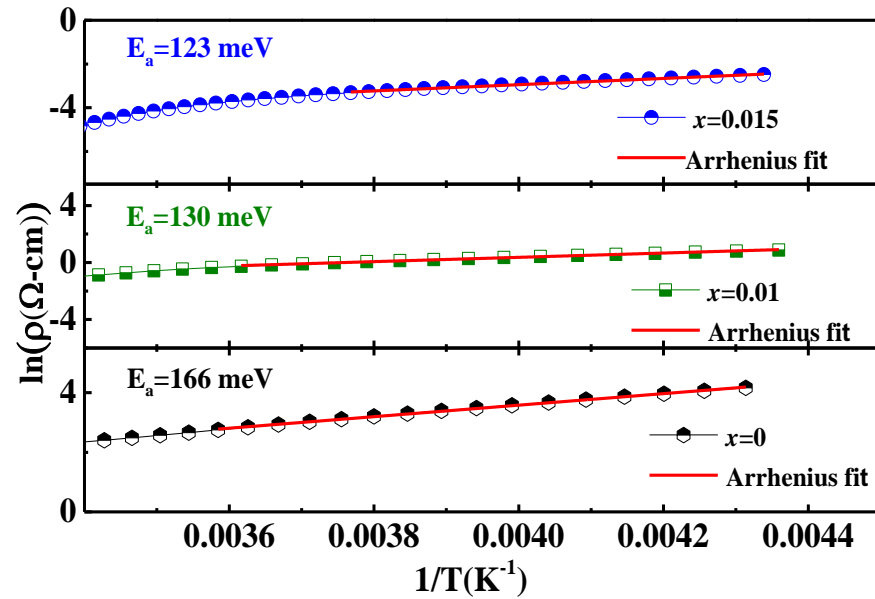


Figure 5.12: Arrhenius fitting of V_{1-x}W_xO₂ (x=0, 0.01, 0.015) thin films in temperature region (230K-280K).

Another useful parameter, MIT strength can be measured by the resistance ratio, defined as below:

$$S = \frac{R_{monoclinic}}{R_{Rutile}}$$

With the inclusion of the W doping into the VO₂ thin films, the strength of MIT weakens because there is no change in the resistivity of metallic phase for W doped films with respect to the undoped films, which agrees with the previously reported results [22]. Thus, the expected shift in MIT was obtained with fine-tuning of structure *via* W doping.

5.4 Summary

A series of crystallographically oriented thin films V_{1-x}W_xO₂ ($x=0, 0.005, 0.01, 0.015, 0.02, 0.03, 0.04$) were deposited on single-crystal sapphire substrate. By only a minor variation of W doping, a gradual structural transformation from monoclinic to rutile phase has been observed without the appearance of any phase anomalies and losing the crystallinity of the films. The analysis of XRD and XPS data clearly confirm successful doping of W in the VO₂ films and the effect of doping on the valence state of vanadium. With the inclusion of W doping a systematic reduction in the transition temperature and activation energy are observed. The room temperature resistivity decreases along with a decrease in the MIT strength. Thus, this work clearly shows that W doping efficiently tunes the transition temperature *via* structural transformation in VO₂ thin films. This tunability can be utilized as per the suitability of the applications.

References:

- [1] Y. Zhao, J. Hwan Lee, Y. Zhu, M. Nazari, C. Chen, H. Wang, A. Bernussi, M. Holtz, Z. Fan, Structural, electrical, and terahertz transmission properties of VO₂ thin films grown on c-, r-, and m-plane sapphire substrates, *J. Appl. Phys.*, 111, (2012), 1-8. (DOI:10.1063/1.3692391).
- [2] R. Long, B. Qu, R. Tan, Y. Sun, X. Tan, W. Ying, B. Pan, Y. Xiong, Y. Xie, Identifying structural distortion in doped VO₂ with IR spectroscopy, *Phys. Chem. Chem. Phys.*, 14, (2012), 7225–7228. (DOI:10.1039/c2cp40392g).
- [3] C. Si, W. Xu, H. Wang, J. Zhou, A. Ablat, L. Zhang, J. Cheng, Z. Pan, L. Fan, C. Zou, Z. Wu, Metal-insulator transition in V_{1-x}W_xO₂ : Structural and electronic origin, *Phys. Chem. Chem. Phys.*, 14, (2012), 15021–15028. (DOI:10.1039/c2cp42313h).
- [4] D. Bhardwaj, A. Goswami, A.M. Umarji, Synthesis of phase pure vanadium dioxide (VO₂) thin film by reactive pulsed laser deposition, *J. Appl. Phys.*, 124, (2018), 135301 (DOI:10.1063/1.5046455).
- [5] B. Chen, D. Yang, P.A. Charpentier, M. Zeman, Al³⁺ - doped vanadium dioxide thin films deposited by PLD, *Sol. Energy Mater. Sol. Cells.*, 93, (2009), 1550–1554. (DOI:10.1016/j.solmat.2009.04.005).
- [6] T.E Phillips, R.A. Murphy, T.O. Poehle Electrical studies of reactively sputtered Fe-doped VO₂ thin films, *Mat.res. Bull.*, 22 (1987), 1113-1123. (DOI:10.1016/0025-5408(87)90241-8).
- [7] B.L. Brown, M. Lee, P.G. Clem, C.D. Nordquist, T.S. Jordan, S.L. Wolfley, D. Leonhardt, C. Edney, J.A. Custer, Electrical and optical characterization of the metal-insulator transition temperature in Cr-doped VO₂ thin films, *J. Appl. Phys.*, 113, (2013), 173704. (DOI:10.1063/1.4803551).

- [8] T.D. Manning, I.P. Parkin, C. Blackman, U. Qureshi, APCVD of thermochromic vanadium dioxide thin films-solid solutions $V_{2-x}M_xO_2$ ($M = Mo, Nb$) or composites $VO_2 : SnO_2$, *J. Mater. Chem.*, 15, (2005), 4560–4566. (DOI:10.1039/b510552h).
- [9] Z.P. Wu, A. Miyashita, S. Yamamoto, H. Abe, I. Nashiyama, K. Narumi, H. Naramoto, Molybdenum substitutional doping and its effects on phase transition properties in single crystalline vanadium dioxide thin film, *J. Appl. Phys.*, 86, (1999), 5311–5313. (DOI:10.1063/1.371519).
- [10] X. Tan, T. Yao, R. Long, Z. Sun, Y. Feng, H. Cheng, X. Yuan, W. Zhang, Q. Liu, C. Wu, Y. Xie, S. Wei, Unraveling metal-insulator transition mechanism of VO_2 triggered by tungsten doping, *Sci. Rep.*, 2, (2012), 466. (DOI:10.1038/srep00466).
- [11] E. Shin, K.C. Pan, W. Wang, G. Subramanyam, V. Vasilyev, K. Leedy, T. Quach, Tungsten-doped vanadium dioxide thin film based tunable antenna, *Mater. Res. Bull.*, 101, (2018), 287–290. (DOI:10.1016/j.materresbull.2018.02.007).
- [12] S.E. Chen, H.H. Lu, S. Brahma, J.L. Huang, Effects of annealing on thermochromic properties of W-doped vanadium dioxide thin films deposited by electron beam evaporation, *Thin Solid Films.*, 644, (2017), 52–56. (DOI:10.1016/j.tsf.2017.05.052).
- [13] J. Zou, X. Chen, L. Xiao, Phase transition performance recovery of W-doped VO_2 by annealing treatment, *Mater. Res. Express.*, 5, (2018), 1-9. (DOI:10.1088/2053-1591/aacd8c).
- [14] A.E. Ersundu, M. Çelikkilek Ersundu, E. Doğan, M.B. Güven, A comparative investigation on thermal, structural and optical properties of W and Nb-doped VO_2 -based thermochromic thin films, *Thin Solid Films.*, 700, (2020), 137919. (DOI:10.1016/j.tsf.2020.137919).
- [15] K. Mulchandani, A. Soni, K.R. Mavani, Structure influenced

- rapid hydrogenation using metal-acid contacts on crystallographically oriented VO₂ thin films, *Applied Surface Science*, 541, (2021) 1–5. (DOI:10.1016/j.apsusc.2020.148369).
- [16] P. Schilbe, Raman scattering in VO₂, *Phys. B Condens. Matter.*, 316–317, (2002), 600–602. (DOI:10.1016/S0921-4526(02)00584-7).
- [17] R. Srivastava, L.L. Chase, Raman spectrum of semiconducting and metallic VO₂, *Phys. Rev. Lett.*, 27, (1971), 727–730. (DOI:10.1103/PhysRevLett.27.727).
- [18] J.R. Skuza, D.W. Scott, A.K. Pradhan, Sapphire substrate-induced effects in VO₂ thin films grown by oxygen plasma-assisted pulsed laser deposition, *J. Appl. Phys.*, 118, (2015), 195303. (DOI:10.1063/1.4935814).
- [19] C. Marini, E. Arcangeletti, D. Di Castro, L. Baldassare, A. Perucchi, S. Lupi, L. Malavasi, L. Boeri, E. Pomjakushina, K. Conder, P. Postorino, Optical properties of V_{1-x}Cr_xO₂ compounds under high pressure, *Phys. Rev. B.*, 77, (2008), 1–9. (DOI:10.1103/PhysRevB.77.235111).
- [20] D. Gu, X. Zhou, Z. Sun, Y. Jiang, Influence of Gadolinium-doping on the microstructures and phase transition characteristics of VO₂ thin films, *J. Alloys Compd.*, 705, (2017), 64–69. (DOI:10.1016/j.jallcom.2017.02.138).
- [21] E. Evlyukhin, S.A. Howard, H. Paik, G.J. Paez, D.J. Gosztola, C.N. Singh, D.G. Schlom, W.C. Lee, L.F.J. Piper, Directly measuring the structural transition pathways of strain-engineered VO₂ thin films, *Nanoscale.*, 12, (2020), 18857–18863. (DOI:10.1039/d0nr04776g).
- [22] B. Rajeswaran, A.M. Umarji, Effect of W addition on the electrical switching of VO₂ thin films, *AIP Adv.*, 6, (2016), 035215. (DOI:10.1063/1.4944855).

- [23] D. Lee, H. Kim, J.W. Kim, I.J. Lee, Y. Kim, H.J. Yun, J. Lee, S. Park, Hydrogen incorporation induced the octahedral symmetry variation in VO₂ films, *Appl. Surf. Sci.*, 396, (2017), 36–40. (DOI:10.1016/j.apsusc.2016.11.047).
- [24] S.S. Majid, S.R. Sahu, A. Ahad, K. Dey, K. Gautam, F. Rahman, P. Behera, U. Deshpande, V.G. Sathe, D.K. Shukla, Role of V-V dimerization in the insulator-metal transition and optical transmittance of pure and doped VO₂ thin films, *Phys. Rev. B.*, 101, (2020), 014108. (DOI:10.1103/PhysRevB.101.014108).
- [25] B. Li, S. Tian, H. Tao, X. Zhao, Tungsten doped M-phase VO₂ mesoporous nanocrystals with enhanced comprehensive thermochromic properties for smart windows, *Ceram. Int.*, 45, (2019), 4342–4350. (DOI:10.1016/j.ceramint.2018.11.109).
- [26] F.J. Morin, Oxides which show a metal-to-insulator transition at the neel temperature, *Phys. Rev. Lett.*, 3, (1959), 34–36. (DOI:10.1103/PhysRevLett.3.34).

Chapter 6

Conclusions and Future Prospects

This chapter concludes the present work with some future prospects that can be implemented further. The core objective of this dissertation was to accomplish the rapid hydrogenation in the crystallographically oriented VO₂ thin films and study the physical properties under the effect of the interstitial doping of the hydrogen and substitutional doping of tungsten. Thereby further to modify the structural and electronic properties in a systematic and controlled manner.

6.1 Conclusions

The present study accomplishes the core objectives and justifies the title of the thesis. The key highlights of the work presented in this dissertation are as follow:

- ❖ We have achieved the rapid hydrogenation *via* modification of the metal-acid contact method *i.e.*, we have used the detachable electrode-like structure of metal and tested the said method at different temperatures and under very mild electric fields for rapid hydrogenation.
- ❖ In chapter 3, the role of crystal structure to accommodate the hydrogen is discussed. The modified method of hydrogenation of the films in 30 s was tested at different temperatures (structures). As a result, about two orders of reduction in the room-temperature resistivity is observed after the hydrogenation. Thus, rapid and sustainable hydrogenation is accomplished using a metal-acid contact method. Almost complete dehydrogenation of the films is possible, and results are highly reproducible.
- ❖ In chapter 4, efforts have been made to attain the rapid hydrogenation at *room temperature*. Under very mild electric fields, the rapid hydrogenation is found within the 30 s of the treatment time at *room temperature*. The films are highly reproducible and sustainable even after the several cycles of the hydrogenation and dehydrogenation, which confirms the reliability of the method.
- ❖ In chapter 5, the effects of W doping in the VO₂ thin films and their properties are discussed. The fine-tuning of the structural and electronic properties with the W doping is presented, in

order to understand the structural transformation simultaneous to electronic transition.

6.2 Future Prospects

In spite of uncovering the two easily accessible methods of the rapid hydrogenation in this study, there is still space to further explore the existing method *via* variation in the several parameters in future. Some possible scopes are as listed:

- ❖ The method of hydrogenation can also be further explored, such as using the different contacts of the low work function metal and by varying the concentration of the ionic solution.
- ❖ The hydrogenation of VO₂ nanostructures with high surface to volume ratio can also be tested.
- ❖ Hydrogenation method can be further explored in the direction of hydrogen transportation.
